Spinor Dynamics and Faraday Imaging of Ultra-Cold Gasses

Masters Thesis

Troels Thorsen Mørch
Supervisor - Jan Arlt
Institute for Physics and Astronomy
University of Aarhus
March 2013

Abstract

Within this thesis I have performed the initial investigations into spinor dynamics in an optical lattice and investigated the properties of a dark field Faraday imaging system.

As a prerequisite to these experiments the creation of a Bose-Einstein condensate in a 1D optical lattice was investigated to pave the way for investigations of spinor dynamics. Moreover the control of magnetic fields and microwave radiation was realised for the state preparation scheme. These mechanisms were investigated in detail to give the best possible starting point for the investigation of spinor dynamics.

It was thus possible to load a Bose-Einstein condensate of $5.5(6) \cdot 10^4$ atoms at a purity of $60(6)\%$ into the optical lattice and prepare the $|F = 2, m_F = 0\rangle$ state containing 99% of the atoms. The initial investigation of spinor dynamics in this configuration are presented. The first results indicate the need for better comparison with theory and the need for more investigations. The future prospects of this research are discussed and evaluated in the context of the creation of EPR pairs to be used in quantum communication protocols.

The dark field Faraday imaging system is explained and characterised. It is shown to be a reliable method for in situ investigation of ultra-cold atomic ensembles. The destructiveness of the method is investigated showing that it can reliably probe thermal clouds multiple times without significantly heating the system. A first investigation of Bose-Einstein condensates using this method is presented highlighting the limitations of the system and illustrating future improvements to be made. A number of applications of the Faraday technique are presented, showing applications in imaging system calibration, trap characterisation and magnetometry. Future applications are discussed for the implementation of feedback in the system and for imaging Bose-Einstein condensates.

The investigations has been performed in the Ultra-Cold Quantum Gasses group at Aarhus University.

Acknowledgements

I would like to thank the Århus Ultra-Cold Quantum gasses group as a whole for an interesting and exciting year working in the laboratory and participating in group discussions. I would particularly like to thank Jan Arlt for great supervision, being available for discussions on a short notice and engaged guidance of my writing process.

Jacob Sherson and Andrew Hilliard I would like to thank for additional guidance when queried and for being the driving force behind many of the weekly group discussions.

I would like to thank Poul Lindholm Pedersen and Miroslav Gjadacz for guidance and help with laboratory work and for taking time to show me the intricacies of the laboratory. I would also like to thank them along with the rest of the quantum gas group for an enjoyable social life both in the daily work and also after work.

Contents

1. Introduction

The experimental realisation of gaseous Bose-Einstein condensates in 1995 [1, 2, 3] unlocked the door to a new field in modern physics. Weakly interacting condensates have spurred investigations in many directions related to fields such as solid state, atomic, nuclear and condensed matter physics. They have also become viable candidates for quantum information, computing and simulation routines. In this context the internal degrees of freedom of a Bose-Einstein condensate become very interesting since they unlock more dynamics for investigation.

Spin dynamics in an optical lattice may allow for the production of Einstein, Podolsky and Rosen (EPR) pairs of atoms in higher lattice bands [4]. In the context of quantum computing and information. Quantum non-demolition measurements of Bose-Einstein condensates may allow for feedback into and extraction of information from quantum system with minimal perturbation of the operator under investigation.

Gaseous alkali Bose-Einstein condensates are an ensemble of neutral atoms confined to the single particle ground state as a result of Bose-Einstein statistics. The condensate thus forms a coherent atomic ensemble which allows for the realisation of coherent atomic physics. The low density and weak interaction of the condensate allow it to function as a model system for many other quantum systems of interest [5].

The first experimental realisation of gaseous Bose-Einstein condensates was in 1995 but the field of quantum gasses has its origin in 1924 with Satyendra Nath Bose's description of photon statistics [6]. Bose's work on photons was applied by Albert Einstein to massive particles [7]. A consequence of Einstein's work on non-interacting particles was a macroscopic occupation of the single particle ground state below a certain temperature. The theory neglected interactions between atoms and was a purely statistical phenomena. It was initially thought that interactions excluded the possibility of creating a Bose-Einstein condensate since they would lead to the formation of solids. In 1938 the observation of super-fluid helium became the first example of a Bose-Einstein condensed system [8, 9]. The connection between Bose-Einstein condensation and super-fluid helium was made by Fritz London that same year [10]. Thus there was one example of a Bose-Einstein condensed system though no substance was a viable candidate for a pure Bose-Einstein condensate. In super-fluid helium there are strong interactions unlike the condensation phenomena discussed by Einstein which was independent of interactions. The strong interactions in super-fluid helium lead to a small population in the zero momentum state, because of depletion by interactions.

In 1959 Hecht suggested that spin polarised hydrogen would stay a gaseous down to zero temperature [11]. It still took almost twenty years before real experimental work towards Bose-Einstein condensation in spin polarised hydrogen began. This work was triggered by confirmation of Hecht's prediction through numerical simulation [12]. Spin polarised hydrogen was not the first gaseous condensate but it provided important steps towards the production of a gaseous condensate. Many techniques developed for trapping and cooling spin polarised hydrogen, such as magnetic traps and evaporative cooling, were indispensable for creating the first gaseous Bose-Einstein condensates. In 1998 a condensate of spin polarised hydrogen was finally realised by the group of Thomas Greytak at MIT [13].

Spin polarised hydrogen might have been the first candidate for the creation of a gaseous Bose-Einstein condensate but it was not the first actual condensate since alkali atoms can be optically cooled. With the advent of evaporative cooling the road to Bose-Einstein condensates was clear and in 1995 both the MIT, JILA and Rise groups reported the first observation of Bose-Einstein condensates [1, 2, 3]. After the realisation of the first condensates the field quickly expanded with many more atomic species shown to undergo Bose-Einstein condensation. Not only have more species been added, Bose-Einstein condensed molecules and degenerate Fermi gasses has also been created [14, 15, 16, 17].

Bose-Einstein condensates provide a macroscopic quantum system which can be manipulated and probed using electric and magnetic fields. The success of the field reflects itself in the many branches of research in which ultra-cold atomic physics has found applications. Moreover Bose-Einstein condensation and the properties of condensates provide an interesting field in itself. These properties include vortices, interference, solitons and low temperature phenomena [18, 19]. Ultra-cold atomic physics, including degenerate Fermi-gasses and Bose-Einstein condensation of molecules, are useful for simulating condensed matter physics, high energy and low dimensional physics. Many of the atomic species that have been Bose-Einstein condensed have tunable interactions. Feshbach resonances have increased the applications of Bose-Einstein condensates to the investigation phenomena such as molecular physics [20]. The existence of Feshbach resonances also allow the interaction to be turned off and study the ideal non-interacting system as described by Einstein.

The Spin degree of freedom is another avenue of investigation which allow for the observation of even more complex dynamics, than the scalar condensates. The field of multi-component dynamics was triggered by the production of multi-component condensates [21, 22]. Later the realisation of true spinor condensates were realised by the optical confinements of ultra-cold atoms. In the case of alkali atoms the spinors take the form of the Zeeman sub-levels of the ground-state hyperfine manifolds. The first optical confinement of neutral atoms was achieved by the MIT group trapping sodium in an optical dipole trap in 1998 [23]. The early experimental and theoretical investigations were into the ground state properties, dynamics of the systems and domain formation [24, 25, 26, 27, 28]. Later the effects of the magnetic field on the dynamics gained interest [29]. The effect of a quantum phase transitions by quenching of condensates from high to low magnetic fields initiating spinor dynamics were investigated [30]. It was possible to tune the linear and quadratic Zeeman energy to investigate dynamics and observe the amplification of vacuum fluctuations [31, 32, 33]. The dynamics of spinor condensates in optical lattices were also investigated [34]. These investigations allowed for great control of the dynamics by working in the Mott insulating phase with a site occupation of 2. The effects of the trap and later the orientation of the magnetic field are also areas of investigation [35, 36, 37].

Within this thesis the combination of optical lattice properties coupled with excitations caused by spin changing collisions are under investigation. One goal of these investigations is the creation of Einstein, Podolsky and Rosen pairs propagating in an optical lattice.

Back action from measurements has been a part of quantum mechanics since its inception. By measuring an operator the uncertainty of this operator is decreased leading to an increase in the uncertainty of another non-commuting operator, for example the position and momentum operators. This leads to the concept of back action which make it difficult to probe a system more than once, without affecting the outcome of subsequent measurements. As an answer to this the concept of a quantum non-demolition measurement was introduced in the 1970's. The idea is to perform the measurement in such a way that the increase in uncertainty is applied to an operator that does not couple back into the originally observed operator. These quantum non-demolition techniques were first discussed in the context of gravitational wave measurements in the 1970's [38, 39, 40, 41].

In the 1980's the the field of quantum optics became an interesting area for quantum non-demolition measurements [42, 43, 44]. This field was promising for performing high quality measurements because of the high sensitivity of optical sources and sensors allowing for detection of fluctuations below the shot noise level. Early experimental investigations were done using cavity quantum electro dynamics where the light interacts with a few or a single atom and this atom is strongly coupled to the cavity [45, 46, 47, 48]. Later the coupling of an atomic ensemble and quantum light was investigated [49].

For non-destructive imaging of a spatially inhomogeneous sample such as an ultra-cold cloud there are multiple methods available, such as phase-contrast imaging [50], diffraction techniques [51] and Faraday rotation [52]. All these techniques use off resonant light to probe the atomic cloud. The light is affected by the cloud leading to phase shifts, diffraction or polarisation rotations depending on the method used. Further development of such quantum non-demolition measurements is of great interest in regards to quantum information and quantum computing. Today phase-contrast imaging is the preferred method for non-destructive probing of ultra-cold atomic clouds. It is usually applied to samples with small line density where it has better signal to noise ratio than other non-destructive methods [50]. Depending on the strength of the interaction between the atomic cloud and the probe light a specific method may be favourable.

In addition Faraday rotation provides a source of entanglement between the atoms and the light, thereby offering more possibilities for quantum systems [53]. Spatially resolved Faraday imaging has been performed by the Copenhagen group [54]. In this thesis a different method for performing non-destructive Faraday imaging is presented and investigated. We call it dark field Faraday imaging, since the light that has interacted with the atoms is transmitted on the dark port of a polarising beam splitter. I present a characterisation of the imaging system and cover some applications of the Faraday system.

This thesis is structured as follows: A theoretical chapter covers the interaction of atoms and off-resonant light and the spinor dynamics. This is followed by a description of the experimental setup and some characterisation measurements in chapter thee. In chapters four and five the results of the spinor and Faraday work are presented. The thesis ends with a summary and outlook of future experiments to be performed in both research directions.

2. Theoretical Background

2.1 Atom – Light Interaction

The experiments presented in this thesis rely on the interaction of off-resonant light with atoms. This interaction is well described using the dressed state picture [55, 56]. In this section I derive an effective Hamiltonian which illustrates the trapping potential of the optical lattice and the Faraday effect. A further description of these interactions follows and the section ends with a discussion of heating due to spontaneous emission.

To describe the atom we use the coherence operator $\hat{\sigma}_{ij} = |i\rangle\langle j|$, for $i = j$ it corresponds to the population operator of the state i and in the case $i \neq j$ the coupling between the two states. The light field is described by the creation and annihilation operators ($\hat{a}^\dagger$ and $\hat{a}$) and $n_{ph} = \hat{a}^\dagger\hat{a}$ is the photon number operator.

In the dressed state picture the full Hamiltonian contains the atomic Hamiltonian $H_A = \hbar\omega_A\sigma_{ee}$ and the light Hamiltonian $H_L = \hbar\omega_L a^\dagger a$, where ω_A and ω_L are the atomic transition frequency and the laser frequency respectively. These are free space Hamiltonians and describe a system with no interaction, see figure 2.1(a) [55, 56]. Including interactions causes

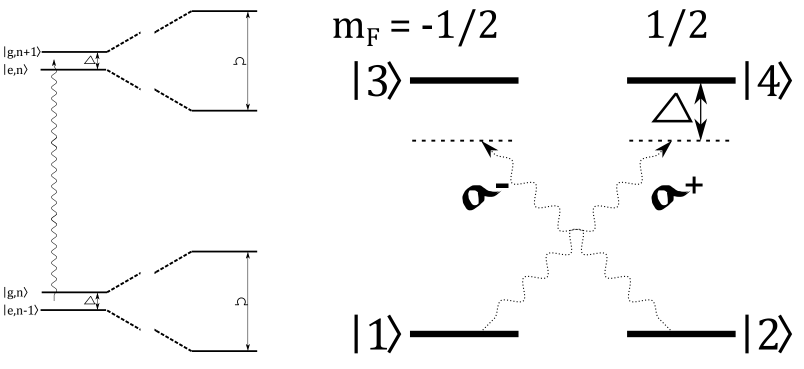

(a) (b) (c)

Figure 2.1: Energy diagrams of the dressed state picture (a) without and (b) with the interaction term. The splittings are the detuning Δ and the effective Rabi frequency $\Omega = \hbar g^2 d^2 n_{ph}/\Delta$. (c) The state diagram for a doubly degenerate two level system used in illustrating the Faraday effect. The state $|1\rangle$ and $|3\rangle$ are in the $m_F = -1/2$ manifold while the states $|2\rangle$ and $|4\rangle$ are in the $m_F = 1/2$ manifold. The transitions are coupled by $\sigma^\pm$ polarised light.

an energy shift in the coupled system compared to the non-interacting system, figure 2.1(b). The interaction term can be considered as the coupling between the ground and excited state dressed by a photon of a given detuning.

The interaction is given by

$$H_{int} = -\hbar g d \left(\hat{\sigma}_{eg} \hat{a} e^{-i\omega_L t} + \hat{a}^\dagger e^{i\omega_L t} \hat{\sigma}_{ge} \right) \tag{2.1}$$

where $g = \sqrt{\frac{\omega_L}{2\hbar\varepsilon_0 V}}$, $d = \langle i | e\mathbf{r} | j \rangle$ is the dipole matrix element of the atomic transition, ε_0 is the vacuum permittivity and V the volume of the light field [55, 56]. This interaction Hamiltonian assumes the dipole approximation [55] where the atom is considered to be small compared to the length scale of the laser wavelength. Because of this the effective laser field can be assumed to be uniform across the atom. Another assumption of the interaction Hamiltonian is the rotating wave approximation [55]. The result is an effective Hamiltonian that scales as $\frac{1}{\omega_L - \omega_A}$, without the rotating wave approximation another term involving $\frac{1}{\omega_L + \omega_A}$ would also contribute. For small detuning ($\Delta = \omega_L - \omega_A$) the second term can be neglected, see section 2.1 for more on the effects of this on the lattice depth.

The model system is based on a two level atom interacting with linearly polarized light, it follows the derivations of Duan *et. al.* [57]. In the absence of a magnetic field the energy levels of the atom are doubly degenerate, the ground and excited states each correspond to a spin 1/2 system. The ground lower manifold consists of the states $|1\rangle$ and $|2\rangle$ and the excited manifold the states $|3\rangle$ and $|4\rangle$, having spin $-1/2$ and $+1/2$ respectively along the quantisation axis, see figure 2.1(c). Linearly polarised light traveling along the quantisation axis can only drive $\sigma^\pm$ transitions, form selection rules. These transitions are the $|1\rangle$ to $|4\rangle$ and $|2\rangle$ to $|3\rangle$ transitions respectively. Leading to a Hamiltonian for two seperate two level system.

$$\begin{aligned} \hat{H} = \hbar\omega_L \hat{a}_+^\dagger \hat{a}_+ + \hbar\omega_A \hat{\sigma}_{44} - \hbar g d \left(\hat{\sigma}_{41} \hat{a}_+ e^{-i\omega_L t} + \hat{a}_+^\dagger e^{i\omega_L t} \hat{\sigma}_{14} \right) \\ + \hbar\omega_L \hat{a}_-^\dagger \hat{a}_- + \hbar\omega_A \hat{\sigma}_{33} - \hbar g d \left(\hat{\sigma}_{32} \hat{a}_- e^{-i\omega_L t} + \hat{a}_-^\dagger e^{i\omega_L t} \hat{\sigma}_{23} \right). \end{aligned} \tag{2.2}$$

It is possible to eliminate the coupling operators between the ground and excited states leaving a Hamiltonian only dependent on the population in the ground states and the photon number operators for the $\sigma^\pm$ components. To get there a slowly varying operator[1] is introduced $\tilde{\sigma}_{23} = \hat{\sigma}_{23} e^{i\omega_L t}$. Using the Heisenberg equation of motion, the time evolution of $\tilde{\sigma}_{23}$ and $\tilde{\sigma}_{14}$ can be found

$$\begin{aligned} \frac{d\tilde{\sigma}_{23}}{dt} &= \hat{\sigma}_{23} \frac{d}{dt} e^{i\omega_L t} + \frac{d\hat{\sigma}_{23}}{dt} e^{i\omega_L t} = \left(i\omega_L \hat{\sigma}_{23} + \frac{1}{i\hbar} \left[\hat{\sigma}_{23}, \hat{H} \right] \right) e^{i\omega_L t} \\ &= i e^{i\omega_L t} \left(\hat{\sigma}_{23} \omega_L - \hat{\sigma}_{23} \omega_A + g d \left(\hat{a}_- e^{-i\omega_L t} \left[\hat{\sigma}_{23}, \hat{\sigma}_{32} \right] + \hat{a}_-^\dagger e^{i\omega_L t} \left[\hat{\sigma}_{23}, \hat{\sigma}_{23} \right] \right) \right) \\ &= +i \left(\Delta \tilde{\sigma}_{23} + g d \hat{a}_- \left(\hat{\sigma}_{22} - \hat{\sigma}_{33} \right) \right). \end{aligned} \tag{2.3}$$

---

[1] $\hat{\sigma}_{23}$ oscillates at the atomic frequency while $\tilde{\sigma}_{23}$ oscillates with the detuning.

Because the light is far detuned the excited state population is very small, meaning $\frac{d\tilde{\sigma}_{23}}{dt} \approx i\left(\Delta\tilde{\sigma}_{23} + gd\hat{a}_-\hat{\sigma}_{22}\right)$. Thinking about the timescales involved[2] we see that $\tilde{\sigma}_{23}$ varies considerably faster than the ground state population $\hat{\sigma}_{22}$. Whenever the ground state changes the coherence term quickly swings into equilibrium. To good approximation the steady state solution can be used

$$\tilde{\sigma}_{23} = \frac{-gd\hat{a}_-\hat{\sigma}_{22}}{\Delta} \qquad\qquad \tilde{\sigma}_{14} = \frac{-gd\hat{a}_+\hat{\sigma}_{11}}{\Delta}. \tag{2.4}$$

This procedure can of course also be applied to $\tilde{\sigma}_{14}$ giving the above result.

With these operators the effective Hamiltonian, ignoring the free space terms, becomes

$$\begin{aligned}
\hat{H}_{eff} &= -\hbar gd\left(\hat{\sigma}_{41}\hat{a}_+e^{-i\omega_L t} + \hat{a}_+^\dagger e^{i\omega_L t}\hat{\sigma}_{14}\right) - \hbar gd\left(\hat{\sigma}_{32}\hat{a}_-e^{-i\omega_L t} + \hat{a}_-^\dagger e^{i\omega_L t}\hat{\sigma}_{23}\right)\\
&= -\hbar gd\left(\tilde{\sigma}_{14}^\dagger\hat{a}_+ + \hat{a}_+^\dagger\tilde{\sigma}_{14}\right) - \hbar gd\left(\tilde{\sigma}_{23}^\dagger\hat{a}_- + \hat{a}_-^\dagger\tilde{\sigma}_{23}\right) = \frac{2\hbar g^2d^2}{\Delta}\left(\hat{\sigma}_{11}\hat{a}_+^\dagger\hat{a}_+ + \hat{\sigma}_{22}\hat{a}_-^\dagger\hat{a}_-\right)\\
&= -\frac{\hbar g^2d^2}{\Delta}\left((\hat{\sigma}_{22}-\hat{\sigma}_{11})(\hat{a}_+^\dagger\hat{a}_+ - \hat{a}_-^\dagger\hat{a}_-) - (\hat{a}_+^\dagger\hat{a}_+ + \hat{a}_-^\dagger\hat{a}_-)(\hat{\sigma}_{11}+\hat{\sigma}_{22})\right)\\
&= -\frac{\hbar g^2d^2}{\Delta}\left((\hat{\sigma}_{22}-\hat{\sigma}_{11})(n_+ - n_-) - n_{ph}n_{at}\right)
\end{aligned} \tag{2.5}$$

$n_\pm$ is the photon number operator for the $\sigma^\pm$ polarised light and n_{at} is the atom number. The first term in the effective Hamiltonian describes the Faraday rotation. If the sample is magnetically oriented the sign difference between the $\sigma^\pm$ components gives rise to a phase shift between the two components of the light. This is interperted as a rotation of the polarisation. The second term is the AC-Stark shift which is an energy shift dependent on the local number of photons an atom interacts with [56]. This is used in deriving the equations for the dipole trapping potential, the subject of the next section.

Optical Lattices

To describe an optical lattice we consider the second term of the effective Hamiltonian. This term is spin independent and an interpretation of this term is that it provides a shift in the eigenenergies of the dressed atom-light diagram dependent on the intensity of the light. It is the inhomogeneity of the trapping laser that creates the trapping potential.

Consider a single atom interacting with a far-detuned linearly polarised high intensity laser. The first term in equation 2.5 becomes negligible because $n_{ph} \gg n_+ - n_-$ leading to

$$\hat{H}_{eff} = -\frac{\hbar g^2d^2}{\Delta}n_{ph} = -\frac{\omega_L d^2}{2\varepsilon_0 V\Delta}n_{ph} \rightarrow \frac{d^2|E_0|^2}{\hbar\Delta}, \tag{2.6}$$

the final term appears because the classical field amplitude is related to the quantum by $E_0 \leftrightarrow -\sqrt{\frac{2\hbar\omega_L}{\varepsilon_0 V}}n_{ph}$[55, 56].

---

[2] The oscillation frequency of $\tilde{\sigma}_{23}$ (the detuning) and the rate of population oscillations of the ground state.

The effective Hamiltonian corresponds to a shift in the eigenenergies of the dressed states dependent on the magnitude of the electric field $\Delta E_g = \frac{d^2|E_0|^2}{\hbar\Delta}$. The excited state experiences an opposite shift in its eigenenergy. Red detuned light ($\Delta < 0$) causes the ground state to be shifted down in energy while blue detuned light ($\Delta > 0$) shifts the ground state energy up. If the atom is considered semi-classically, this energy shift leads to a confining potential in the case of a red detuned laser where the atom seek high intensity, i.e. the focus of the beam [56, 58].

The dipole matrix element is related to the line width of the transition, which is well known for rubidium 87,

$$\Gamma = \frac{\omega_0^3}{3\pi\varepsilon_0\hbar c^3} d^2. \tag{2.7}$$

Leading to a trapping potential

$$U_{dip}(z,r) = \frac{3\pi c^2}{2\omega_0^3}\frac{\Gamma I(z,r)}{\Delta} \tag{2.8}$$

where z is the propagation axis of the laser while r is the radial coordinate.

The spatial dependence is the intensity, which is the source of the confining potential. The electric field of a linearly polarised Gaussian beam traveling along the Z-axis is given as [5, 58, 59]

$$E(z,r) = E_0\hat{\varepsilon}\frac{w_0}{w(z)}e^{ikz}e^{-r^2/w(z)^2}, \tag{2.9}$$

where $\hat{\varepsilon}$ is the polarisation vector, E_0 the field amplitude, $w(z) = W_0\sqrt{1+\left(\frac{z}{z_R}\right)^2}$ the beam waist at z, w_0 the beam waist at the focus and $z_R = \pi w_0^2/\lambda$ the Rayleigh length.

An optical lattice is formed by two counter-propagating laser beams, each described by equation 2.9, with parallel polarisation. The electric fields of the two beams are added to obtain

$$E(z,r) = E_0\hat{\varepsilon}\frac{w_0}{w(z)}e^{-r^2/w(z)^2}\left(e^{ikz}+e^{-ikz}\right) = 2E_0\hat{\varepsilon}\frac{w_0}{w(z)}e^{-r^2/w(z)^2}\cos(kz). \tag{2.10}$$

The intensity is proportional to the squared electric field $I = 2\varepsilon_0 c|E|^2$

$$I(z,r) = 4I_0\left(\frac{w_0}{w(z)}\right)e^{-2r^2/w(z)^2}\cos^2(kz) \tag{2.11}$$

where $I_0 = \frac{2P}{\pi w_0^2}$ is the intensity of one beam in its focus [59], P is the power of the laser

$$I(z,r) = \frac{8P}{\pi w_0}\left(\frac{w_0}{w(z)}\right)e^{-2r^2/w(z)^2}\cos^2(kz). \tag{2.12}$$

To obtain a better description of the trapping potential, the simple model described above has to be modified. Two factors are important for a better model for the optical lattice.

First, the multilevel structure of rubidium 87 has to be taken into account and secondly the use of the rotating wave approximation is not exactly valid for our lattice.

The multilevel structure of rubidium 87 is due to the two excited states. Transitions from $5^2\mathrm{S}_{1/2}$ to both $5^2\mathrm{P}_{1/2}$ and $5^2\mathrm{P}_{3/2}$ contribute to the trapping potential. Equation 2.8 becomes [58]

$$U_{dip}(z,r) = \frac{3\pi c^2}{2}\left(\frac{2\Gamma_2}{\Delta_2\omega_2^3} + \frac{\Gamma_1}{\Delta_1\omega_1^3}\right) I(z,r) \tag{2.13}$$

where Δ_i, ω_i and Γ_i are the detuning, frequency and line-width of the D_1 and D_2 transitions.

If the rotating wave approximation is not applied, the effective Hamiltonian has to be modified. Luckily this modification is only the inclusion of a second term [5]

$$\frac{1}{\Delta} \to \frac{1}{\Delta} + \frac{1}{\omega_L + \omega_A}. \tag{2.14}$$

The validity of the rotating wave approximation depends on the ratio of the two terms. For our lattice the correction is around 8% which is not ignorable. Without the rotating wave approximation the potential is

$$U_{dip}(z,r) = \frac{3\pi c^2}{2}\left(\frac{2\Gamma_2}{\Delta_2\omega_2^3} + \frac{2\Gamma_2}{(\omega_2+\omega_L)\omega_2^3} + \frac{\Gamma_1}{\Delta_1\omega_1^3} + \frac{\Gamma_1}{(\omega_1+\omega_L)\omega_1^3}\right) I(z,r). \tag{2.15}$$

When working with an optical lattice the quantity of interest is the lattice depth given as the depth of the potential in the center of the lattice

$$U_0 = U_{dip}(0,0) = \frac{3\pi c^2}{2}\left(\frac{2\Gamma_2}{\Delta_2\omega_2^3} + \frac{2\Gamma_2}{(\omega_2+\omega_L)\omega_2^3} + \frac{\Gamma_1}{\Delta_1\omega_1^3} + \frac{\Gamma_1}{(\omega_1+\omega_L)\omega_1^3}\right) \frac{8P}{\pi w_0}. \tag{2.16}$$

The depth of the lattice is measured in recoil energy $E_{rec} = \frac{(\hbar k)^2}{2m_{Rb}}$, where k is the photon wave number [5, 56] and is given by $s = U_0/E_{rec}$ for the one dimensional lattice.

For Bose-Einstein condensates in an optical lattice there are two relevant regimes. If the lattice depth is small, typically below 5 E_{rec}, the lattice is said to be in the super-fluid regime while deep lattices, typically above 10 E_{rec}, are said to be in the isolating regime. The exact depth at which the transition between the two regimes occur is dependent on the actual lattice.

All spinor work presented in this thesis has been performed at a lattice depth of 16 E_{rec}, well within the isolating regime. Because of this relatively deep lattice, properties such as band structure and tunneling between lattice sites, know from solid state physics, can be ignored. The combination of lattice and spinor dynamics will be the subject of further investigations. In the work presented here these lower lattices have not been investigated and each lattice site is considered an individual trap.

If each lattice site can be considered an individual trapping potential it can be well approximated by a harmonic potential. For a harmonic trap the trapping frequencies are

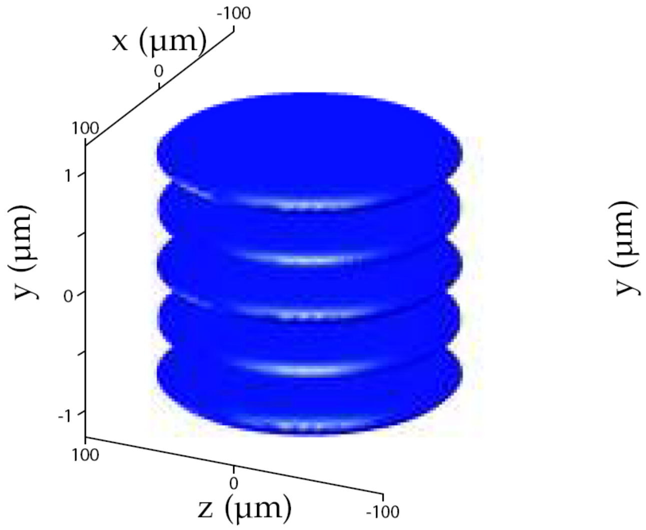

Figure 2.2: Equipotential surface of the lattice. This illustrate the pancake structure of the lattice and how deep lattice can be considered individual traps. Figure from [77]

given by the characteristic lengths of the trap. For the lattice these lengths are the beam waist and the wave-length of the lattice laser, for the radial and axial frequencies respectively

$$\omega_\perp = \sqrt{\frac{4U_0}{m_{Rb} w_0^2}} \qquad \omega_\parallel = \sqrt{\frac{2U_0}{m_{Rb}} k^2}. \tag{2.17}$$

Each lattice site has a pancake shape due to the large difference in the characteristic lengths. The lattice can be seen as a number of pancakes lying on top of each other, see figure 2.2. There is a separate condensate in each lattice site, with its own atom number and density.

Because the lattice is formew by a focused beam, the trap depths vary along the axial direction. The largest clouds we load into the lattice have an extent of 20 sites around the focus. The Rayleigh length of the lattice is on the order of centimeters so these twenty sites have very similar trapping parameters.

The Faraday Effect

The second subject of my masters work is the characterisation of Faraday non-destructive imaging. I describe the theory for the atom-light interaction starting from the effective Hamiltonian, equation 2.5. It is worth noting that this model is not fully realistic. In the experiment work is performed with atoms in the $|2,2\rangle$ state and we drive the D_2 transition off-resonantly. The complication in this case is again due to the multilevel structure of Rubidium 87. The multilevel structure of the atom was taken into account in [60] for the general case, in [61] in the case of rubidium. In the case of alkali atoms the polarisability of the atom can be described as a tensor consisting of a scalar $\alpha^{(0)}$, a vector $\alpha^{(1)}$ and a tensor term $\alpha^{(2)}$. The interaction Hamiltonian can be expressed as a linear combination of these three [62]

$$
\begin{aligned}
\hat{H}_I &= \hat{H}_I^{(0)} + \hat{H}_I^{(1)} + \hat{H}_I^{(2)} \\
\hat{H}_I^{(0)} &= \frac{\hbar g^2}{3}\alpha^{(0)} n_{at} n_{ph} \\
\hat{H}_I^{(1)} &= \hbar g^2 \alpha^{(1)} \hat{\mathscr{F}}_z \hat{\mathscr{S}}_z \\
\hat{H}_I^{(2)} &= \hbar g^2 \alpha^{(2)} \left((\hat{\mathscr{F}}_x^2 - \hat{\mathscr{F}}_y^2)\hat{\mathscr{S}}_x + (\hat{\mathscr{F}}_x\hat{\mathscr{F}}_y + \hat{\mathscr{F}}_y\hat{\mathscr{F}}_x)\hat{\mathscr{S}}_y + \hat{\mathscr{S}}_0(\hat{\mathscr{F}}_z^2 - \frac{1}{3}\hat{\mathscr{F}}^2) \right)
\end{aligned}
\tag{2.18}
$$

$\hat{\mathscr{F}}_i$ and $\hat{\mathscr{S}}_i$ are collective spin operators for the cloud and elements of the stokes vector respectively, see [63, 64]. In this section it is assumed that the laser intensity can be considered constant across the whole cloud. This assumption is reasonably well fulfilled in our experiment where the waist of the collimated beam is on the order of millimeters while the cloud is around 20 μm wide. The first two terms correspond to equation 2.5 while the tensor term is new. For now $\hat{H}_I^{(0)}$ can be ignored since it only introduces an overall phase-shift which affects the $\sigma^{\pm}$ polarisations equally [60]. For an atom in the $|2,2\rangle$ ground state the vector and tensor polarisability, following [61] and [52], become

$$\alpha^{(1)} = -\alpha_0 \left(-\frac{1}{20}D_{21} - \frac{1}{12}D_{22} + \frac{7}{15}D_{23} \right) \tag{2.19}$$

$$\alpha^{(2)} = -\alpha_0 \left(\frac{1}{60}D_{21} - \frac{1}{12}D_{22} + \frac{1}{15}D_{23} \right) \tag{2.20}$$

where $\alpha_0 = \frac{3\varepsilon_0 \hbar \Gamma \lambda^3}{8\pi^2}$, Γ is the natural linewidth of the D_2 transition and λ the laser wavelength. $D_{ij} = \frac{\Delta_{ij}}{\Delta_{ij}^2 + \Gamma^2/4}$ are relative detunings for the transition $|F = i\rangle$ to $|F' = j\rangle$.

In the case of large detuning[3] $\Delta \gg \Gamma$, $D_{ij} \rightarrow \frac{1}{\Delta}$ meaning $\alpha^{(2)} \approx 0$. Only the vector term remains

$$\hat{H}_{int} = \hat{H}_{int}^{(1)} = -\frac{\hbar g^2 \alpha_0}{3\Delta_{eff}} \hat{\mathscr{F}}_z \hat{\mathscr{S}}_z, \qquad \frac{1}{\Delta_{eff}} = \frac{1}{20}\left(-3D_{2,1} - 5D_{2,2} + 28D_{2,3}\right). \tag{2.21}$$

This Hamiltonian is used to determine the evolution of the Stokes vector which in turn gives the Faraday rotation angle, the quantity of interest. The effective detuning takes the different hyperfine manifolds into account. They were set equal in the argument for eliminating $\alpha^{(2)}$ this does not cause a problem for large detuning. The effects close to resonance have also been examined, where the contribution from the different hyperfine transitions have to be taken into account. It is therefore simpler to use the effective detuning. Around the resonances, the approximation of $\alpha^{(2)} = 0$ is no longer valid. In the case of a cloud

---

[3] Normally $\Delta > 100\Gamma$ in our experiments

that is spin polarised along the Z-axis, the X and Y components of the spin operator are negligible. To a first approximation $H_I^{(2)}$ in equation 2.18 becomes

$$\hat{H}_I^{(2)} \approx \hbar g^2 \alpha^{(2)} \hat{\mathscr{S}}_0 (\hat{\mathscr{F}}_z^2 - \frac{1}{3}\hat{\mathscr{F}}^2). \tag{2.22}$$

$[\hat{\mathscr{S}}_i, \hat{\mathscr{S}}_0] = 0$ for $i = \{x, y, z\}$ [63, 64]. So as a first approximation the inclusion of $\alpha^{(2)}$ should not affect the evolution of the Stokes vector and therefore not affect the Faraday rotation. Even close to resonance equation 2.21 is still valid.

To find the evolution of the Stokes vector we look at the time derivative of its components

$$\begin{aligned}
\frac{d\hat{\mathscr{S}}_x}{dt} &= \frac{1}{i\hbar}\left[\hat{\mathscr{S}}_x, \hat{H}_{int}\right] = -\frac{g\alpha_0}{\Delta_{eff}\hbar}\hat{\mathscr{F}}_z\hat{\mathscr{S}}_y \\
\frac{d\hat{\mathscr{S}}_y}{dt} &= \frac{1}{i\hbar}\left[\hat{\mathscr{S}}_y, \hat{H}_{int}\right] = -\frac{g\alpha_0}{\Delta_{eff}\hbar}\hat{\mathscr{F}}_z\hat{\mathscr{S}}_x \\
\frac{d\hat{\mathscr{S}}_z}{dt} &= \frac{1}{i\hbar}\left[\hat{\mathscr{S}}_z, \hat{H}_{int}\right] = 0 \\
\frac{d\hat{\mathscr{S}}_0}{dt} &= \frac{1}{i\hbar}\left[\hat{\mathscr{S}}_0, \hat{H}_{int}\right] = 0
\end{aligned} \tag{2.23}$$

because $\left[\hat{\mathscr{S}}_i, \hat{\mathscr{S}}_j\right] = i\varepsilon_{ijk}\hat{\mathscr{S}}_k$. If we look at the second derivative of $\hat{\mathscr{S}}_x$ we see that this is a rotation around the Z-axis.

$$\frac{d^2\hat{\mathscr{S}}_x}{dt^2} = -\frac{g\alpha_0}{\Delta_{eff}\hbar}\hat{\mathscr{F}}_z\frac{d\hat{\mathscr{S}}_y}{dt} = -\left(\frac{g\alpha_0}{\Delta_{eff}\hbar}\hat{\mathscr{F}}_z\right)^2\hat{\mathscr{S}}_x = -\omega_S^2\hat{\mathscr{S}}_x \tag{2.24}$$

A similar equation can of course be derived for $\hat{\mathscr{S}}_y$ giving harmonic equations corresponding to a rotation around the Z-axis. The total rotation is then

$$\theta = \frac{1}{2}\omega_S\tau, \tag{2.25}$$

where $\tau = \frac{L}{c}$ is the light-atom interaction time, L being the length of the sample and c the speed of light.

In the experiments all the atoms are oriented along the Z-axis, meaning the macroscopic angular momentum is oriented along the Z-axis. This allow us to replace the macroscopic spin operator with its expectation value $\hat{\mathscr{F}}_z \rightarrow \langle\hat{\mathscr{F}}_z\rangle = V\rho\langle\hat{F}_z\rangle$ [60] and the angle is given by [61]

$$\theta = \frac{\Gamma\lambda^2\langle\hat{F}_z\rangle L}{16\pi}\frac{\rho(\mathbf{r})}{\Delta} \tag{2.26}$$

where ρ is the density of the gas. This is fine in the case of a sample that has the same length everywhere. To apply it to our atomic cloud we have to integrate each column, as seen from the camera, and then arrive at an effective density for each pixel [65]

$$\theta = \frac{\Gamma\lambda^2\langle\hat{F}_z\rangle}{16\pi\Delta}\int dz\rho(\mathbf{r}) = \frac{\Gamma\lambda^2\langle\hat{F}_z\rangle}{16\pi\Delta}\tilde{\rho}(x,y) = c_F\tilde{\rho}(x,y) \tag{2.27}$$

c_F being the Faraday coefficient. The effective density is a measure of how many atoms the light hitting a particular pixel has interacted with. Thus the total atom number of the cloud can be found by integrating over the whole chip $N_{far} = \int_{\text{chip}} dxdy\theta(x,y)\frac{1}{c_F}$

It is not possible to probe the cloud by light without affecting the cloud itself. The first effect of the off-resonant probing is a rotation of the atomic spin around the Z-axis. We are not sensitive to this rotation in our probing and therefore this does not affect the evolution we can observe. Secondly the cloud will get heated due to spontaneous emission of photons.

Atom Light Scattering

In the beginning of this chapter the interaction of atoms and light was derived in the case of a two-level atom. In this derivation the spontaneous emission was ignored so only stimulated processes contributed. In the realistic case spontaneous emission have to be included. Spontaneous emission can be included by considering lower lying empty modes. The transition from the state of an excited atom and n_{ph} laser photons to the state of a ground state atom and n_{ph} laser photons [56]. This is a lower lying mode compared to the ground state atoms and $n_{ph}+1$ laser photons by an energy $\hbar\omega_L$.

To take the spontaneous emission into account a term $-\frac{1}{2}\Gamma\sigma_{eg}$ have to be included in the evolution of the two level system, we ignore spin for now. The equations of motion for the coherence operators then become.

$$\begin{aligned}
\frac{d\hat{\sigma}_{gg}}{dt} &= -igd\left(\hat{a}^\dagger\hat{\sigma}_{ge}e^{i\omega_L t} - \hat{a}\hat{\sigma}_{eg}e^{-i\omega_L t}\right) - \Gamma\hat{\sigma}_{ee} \\
\frac{d\hat{\sigma}_{ee}}{dt} &= -igd\left(\hat{a}\hat{\sigma}_{eg}e^{-i\omega_L t} - \hat{a}^\dagger\hat{\sigma}_{eg}e^{i\omega_L t}\right) - \Gamma\hat{\sigma}_{ee} \\
\frac{d\tilde{\sigma}_{eg}}{dt} &= -i\left(\Delta\tilde{\sigma}_{eg} + gd\hat{a}\left(\hat{\sigma}_{gg} - \hat{\sigma}_{ee}\right)\right) - \frac{\Gamma}{2}\hat{\sigma}_{eg}
\end{aligned} \tag{2.28}$$

where the slowly varying coherence operator is used again. This can be used to calculate a scattering rate [58]

$$\Gamma_{sc} = \frac{3\pi c^2}{2\hbar\omega_0^3}\left(\frac{\Gamma}{\Delta}\right)^2 I(r) \tag{2.29}$$

The important thing to note is that the scattering falls off as $1/\Delta^2$ while both the depth of the trapping potential and the Faraday signal drop off as $1/\Delta$. The destructiveness can be reduced by going to larger detuning in the case of Faraday imaging. For the lattice a lower heating rate for the same lattice depth can be achieved by going to larger detuning and more power.

Each scattering event of an off resonant photon can be considered as a heating event of the cloud. If an excited atom spontaneously emits a photon, the atom will, by conservation of momentum, receive a kick in the opposite direction, this is the recoil energy. First the atom absorbs an off-resonant photon entering its excited state and then this is re-emitted in any spatial direction. This means that the atoms pick up $2E_{rec}$ for each scattering event[58, 59].

2.2 Spinor Condensates

Spinors are Bose-Einstein condensates with their spin degree of freedom unlocked. To investigate spinor dynamics the atoms have to be in the ground state of the system. If the same investigation was performed on a thermal cloud of atoms the spinor dynamics would be dominated by thermal effects [66]. In this section the basic concepts behind Bose-Einstein condensation in a dilute gas are introduced. These are used to describe spinor condensates and find the instability rates investigated in the experiments.

Bose-Einstein Condensation

A gas of bosons obey Bose-Einstein statistics. From this formalism Bose-Einstein condensation occurs as a natural phenomena at high phase-space density. A system is Bose-Einstein condensed if the single particle ground state is macroscopically occupied. The mean occupation of a single-particle state, ν, is given by the Bose distribution function [5, 67]

$$\bar{n}(\varepsilon_\nu) = \frac{1}{e^{(\varepsilon_\nu - \mu)/k_B T} - 1}. \tag{2.30}$$

Here ε_ν is the energy of the state ν and μ is the chemical potential.

The internal structure of the atoms can be ignored in a first treatment. For rubidium 87 the internal structure is in the form of the hyperfine splitting of the $5^2\mathrm{S}_{1/2}$ ground-state. Here the $F = 1$ and $F = 2$ hyperfine manifolds are split by 6834.682 MHz which is equivalent to a temperature of around 0.3 K. The relevant temperatures for condensates are a few hundred nanoKelvin. The Zeeman splitting of the F = 2 hyperfine manifold is not considered here because it is frozen out during the condensation phase, see section 3.1. There are also two orders of magnitude between the condensation temperature and our trap bottom of 400kHz $\approx 20\ \mu$K.[4]

As discussed above the individual sites of the lattice can be considered individual harmonic trapping potentials

$$V = \frac{1}{2} m(\omega_x^2 x^2 + \omega_y^2 y^2 + \omega_z^2 z^2) \tag{2.31}$$

where ω_i is the trapping frequency in the i'th direction. In this harmonic case the energy levels are given by

$$\varepsilon(\nu_x, \nu_y, \nu_z) = (\frac{1}{2} + \nu_x)\hbar\omega_x + (\frac{1}{2} + \nu_y)\hbar\omega_y + (\frac{1}{2} + \nu_z)\hbar\omega_z \tag{2.32}$$

---

[4] The lowest Zeeman splitting to occur in the magnetic trap.

If ε_{min} is the lowest energy level equation 2.30 makes it clear that $\mu \leq \varepsilon_{min}$. Otherwise the mean occupation of a single particle state can become negative which is unphysical. From now on all states that are not the single particle ground state are referred to as excited states. By looking at the Bose distribution function of the excited states and the fact that $\mu \leq \varepsilon_{min}$, for $T \to 0$ K the mean occupation of the excited states will go to zero. If the mean occupation of all the higher lying states goes to zero they have to condense into the ground state of the system. The ground state can have an arbitrarily large mean occupation number and the system has Bose-Einstein condensed [5].

The condensation temperature (T_C) is the temperature where the mean occupation of the ground state becomes non-zero. The total number of particles in the ensemble must be a sum over all the individual distribution functions.

$$N = \sum \frac{1}{e^{(\varepsilon_\nu - \mu)/k_B T} - 1} \tag{2.33}$$

The number of particles in the excited states, must be the integral over the density of states weighted by the distribution function [5]

$$N_{ex} = \int_0^\infty d\varepsilon \bar{n}(\varepsilon) f(\varepsilon) \tag{2.34}$$

Now by considering this equation in the limit of $\mu = 0$ it is possible to arrive at an equation for the transition temperature given as

$$k_B T_C = 0.94 \hbar \bar{\omega} N^{1/3} \tag{2.35}$$

where $\bar{\omega} = (\omega_x \omega_y \omega_z)^{1/3}$ is the mean frequency of the three axis of the harmonic trap.

Because all the particles in the condensate are in the same state they must also be described by the same wave-function. The total condensate wave-function can be considered the product of N_0 single-particle wave-functions

$$\Psi(r_1, r_2, ..., r_{N_0}) = \prod_i^{N_0} \psi(r_i). \tag{2.36}$$

Another effect of all the particles in the condensate being in the single particle ground-state is that the density profile of the condensate is

$$n(r) = N_0 |\psi_0(r)|^2. \tag{2.37}$$

For a condensate in a harmonic trap the ground-state wave-function is [5]

$$\psi_0(r) = \frac{1}{\pi^{3/4}(a_x a_y a_z)^{1/2}} e^{-x^2/2a_x^2} e^{-y^2/2a_y^2} e^{-z^2/2a_z^2} \tag{2.38}$$

where $a_i = \sqrt{\frac{\hbar}{m\omega_i}}$ is the oscillator length in the i'th direction. The oscillator length determine the relevant length scales of the magnetic trap.

The non-interacting condensate was as mentioned first described by Einstein in the case of massive particles. Interaction is a prerequisite for the experimental realisation of Bose-Einstein condensates. Without interactions the atoms would not rethermalise during evaporative cooling. In spinor condensates the spin dynamics are driven by atomic collisions.

When considering interactions in a Bose-Einstein condensate it is enough to consider two body collisions. In a typical alkali gas condensate the inter-particle separation is on the order of 100 nm [5]. This is an order of magnitude larger then the length scale of the interaction. In the case of the alkali atoms the lowest order van der Waals interaction is the dominant interaction between two atoms, it falls off as r^{-6} [5]. In the condensate the thermal energy of the atoms is very small compared to the characteristic energy of the van der Waals interaction (E_c). Because of this interactions between atoms in anything other than the ground state can be ignored and also that the relative angular momentum of two colliding atoms can be set to zero. Therefore it is reasonable to restrict our treatment to s-wave scattering where all interaction is point interaction between two particles [5, 68].

In the case of s-wave scattering the only free parameter is the s-wave scattering length (a_s), it describes the relevant length scale for atomic interactions. For Rubidium 87 all scattering length are of comparable size around $100a_0$ [5]. The scattering length is large on an atomic scales but small compared to other relevant length scales of the condensate. These could be the inter-particle spacing and the thermal de Broglie wavelength, for rubidium at 200 nK $\lambda_{dB} = \sqrt{k_B T m_{Rb}} \approx 1$ μm. The sign of the scattering length determines if the interaction between the two particles is repulsive or attractive, positive and negative respectively [5, 68].

In the case of low energy s-wave scattering the inter-atomic potential can be approximated by a point like interaction [5, 68]

$$U_0(r_1 - r_2) = \frac{4\pi a_s \hbar^2}{m}\delta(r_1 - r_2) \tag{2.39}$$

where r is the inter-particle distance. This approximation is valid for cold indistinguishable particles[5, 68].

An interacting condensate is described by a many-body mean field approximation leading to the Gross-Pitaevskii equation [5, 68]

$$-\frac{\hbar^2}{2m}\nabla^2\Psi(r) + V_{ext}(r)\Psi(r) + U_0(r)|\Psi(r)|^2\Psi(r) = \mu\Psi(r) \tag{2.40}$$

$\Psi(r)$ being the order parameter given above. The interaction term describes the potential seen by one particle produced by all the other particles in the mean field approximation. In this approximation it is assumed that all particles are in the ground-state of the system. The interactions will lead to a depletion of the condensate, i.e. some atoms will be in excited states. For a normal alkali atom condensate the depletion is usually on the order of one percent, this can be ignored in our description [5, 50, 68].

To extract information from the Gross-Pitaevskii equation we make the Thomas-Fermi approximation. In the Thomas-Fermi approximation the kinetic energy term, $\hbar^2/(2m)\nabla^2\Psi(r)$, is neglected. This approximation is valid when the energy available from interactions, given by $a_s N_0$ is large compared to the energy of the trap given by a_{osc} [5, 68]. The approximation is only valid for the bulk condensate whereas the surface of the condensate has to be treated independently. In the case of spinor work the primary interest is the bulk condensate more than the surface and therefore I will not treat the surface here.

By applying the the Thomas-Fermi approximation to the Gross-Pitaevskii equation it can be recast as [5, 50, 68].

$$n(r) = |\Psi(r)|^2 = \frac{1}{U_0}(\mu - V_{ext}(r)) \tag{2.41}$$

the density profile of the condensate. From the density profile important properties such as the peak density and Thomas-Fermi radius can be extracted. The peak density occur at the minimum of the external potential. The minimum of the external potential for the harmonic trap is zero so the peak density is $n_0 = \mu/U_0$. The density cannot be negative meaning that the external potential have to less than or equal to the chemical potential. For $V_{ext} = \mu$ the condensate has to disappear. From the shape of the potential this happens at

$$R_{TF,i} \equiv \sqrt{\frac{2\mu}{m\omega_i^2}} \tag{2.42}$$

Under the Thomas-Fermi approximation the chemical potential is

$$\mu = \frac{15^{2/5}}{2}\left(\frac{Na_s}{\bar{a}_{osc}}\right)^{2/3}\hbar\bar{\omega} \tag{2.43}$$

Where $\bar{a}_{osc}$ and $\bar{\omega}$ are the mean oscillator length and trapping frequency respectively.

Spinor Dynamics

As mentioned in the introduction optical trapping allow the atomic spin degree of freedom to be unlocked. The effect of the Zeeman splitting on the optical confinement is negligible as discussed above.

The $F = 2$ hyperfine manifold of rubidium 87 has five Zeeman sub-levels denoted $m_F = \{-2,-1,0,1,2\}$. It is this internal degree of freedom that is liberated in the optical trap. If no magnetic field is present the different Zeeman sub-levels are degenerate. With the application of a magnetic field this degeneracy is lifted and small energy differences, on the kHz scale, appear between the different sub-levels. Similar to the scalar condensate the macroscopic order parameter is useful notation. Here the order parameter is a vector comprised of $2F+1$ components [69, 70]

$$\vec{\psi}(r) = \begin{pmatrix} \psi_2(r) \\ \psi_1(r) \\ \psi_0(r) \\ \psi_{-1}(r) \\ \psi_{-2}(r) \end{pmatrix}. \tag{2.44}$$

where $\psi_i(r)$ is the order parameter for the i'th Zeeman sub-level.

For spinor condensates the Hamiltonian can be split into an interacting and a non-interacting part [37]

$$\hat{H} = \hat{H}_0 + \hat{H}_{int} \tag{2.45}$$

The non-interacting Hamiltonian takes single particle effects into account: kinetic energy, the confining potential, the chemical potential and the Zeeman energy. The Zeeman energy is the shift of the individual Zeeman sub-level due to a magnetic field $E_Z = -m_F p + m_F^2 q$ where $p = g_F \mu_B B$ and $q = \mu_B^2 B^2/(8C_{hfs})$ are the linear and quadratic Zeeman energies respectively. g_F is the Landé g-factor, μ_B the Bohr magneton, B the magnetic field and C_{hfs} the hyperfine coupling strength [37]. The non-interacting Hamiltonian is

$$\hat{H}_0 = \int^3 r \sum_{m_F} \hat{\psi}^{\dagger}_{m_F} \left(-\frac{\hbar^2}{2m_{Rb}} \nabla^2 + V_{ext} + E_{Z,m_F} - \mu \right) \hat{\psi}_{m_F} \tag{2.46}$$

The interaction Hamiltonian takes interactions between two particles into consideration, assuming higher order interactions can be ignored. Two atoms in the $|m_f\rangle$ and $|m'_f\rangle$ states collide producing atoms in the $|m_F\rangle$ and $|m'_F\rangle$ states [37]

$$\hat{H}_{int} = \int^3 r \sum_{m_F, m'_F, m_f, m'_f} \hat{\psi}^{\dagger}_{m_F} \hat{\psi}^{\dagger}_{m'_F} U_{m_F, m'_F, m_f, m'_f} \hat{\psi}_{m_f} \hat{\psi}_{m'_f}. \tag{2.47}$$

Interaction in spinor condensates is still in the form of s-wave scattering, as in the scalar condensate. Unlike the scalar condensate there are multiple scattering channels that allow the colliding atoms to change their Zeeman sub-level. The interaction is still determined by the s-wave scattering length between the two colliding atoms. When multiple hyperfine components are available the scattering length depend on the total angular momentum of the interacting atoms. The total angular momentum is comprised of the relative angular momentum between the two atoms and their internal spin. First assume the internal and orbital angular momentum are separately conserved, ignoring spin-orbit coupling. Secondly assume hyperfine relaxation can be ignored[5]. With these assumptions the total spin of the scattering channel has to be even in the case of Bosons [24, 66, 69]. For $F=2$ the total spin of the scattering channel can be 0,2 and 4.

---

[5] Collisions relaxing atoms in the $F=2$ hyperfine manifold to the $F=1$ manifold.

The s-wave scattering can still be described by a contact interaction where

$$\hat{U}(r_1 - r_2) = \delta(r_1 - r_2)U_{m_F,m'_F,m_f,m'_f} = \delta(r_1 - r_2)\sum_{S=0,2,4} g_S\hat{P}_S \tag{2.48}$$

where $g_S = 4\pi\hbar^2 a_S/m_{Rb}$ is the interaction strength of the channel and $\hat{P}_S$ is the projection operator onto the total spin subspace. U_{m_F,m'_F,m_f,m'_f} is the non spatial part of $\hat{U}(r_1 - r_2)$[70, 71]

$$U_{m_F,m'_F,m_f,m'_f} = U_0\delta_{m_F,m_f}\delta_{m'_F,m'_f} + U_1 F_1 \cdot F_2 + 5U_2 P_0 \tag{2.49}$$

where $F_1 \cdot F_2 = (F_{tot}^2 - F_1^2 - F_2^2)/2$, P_0 is the projection onto the total spin zero state and

$$\begin{aligned} U_0 &= \frac{4g_2 + 3g_4}{7} \\ U_1 &= -\frac{g_2 - g_4}{7} \\ U_2 &= \frac{g_0 - g_4}{5} - \frac{2(g_2 - g_4)}{7}. \end{aligned} \tag{2.50}$$

U_0, U_1 and U_2 are the interaction coefficients that change the spin of the interacting atoms by $\Delta m_F = \{0, 1, 2\}$.

When the dynamics of the condensate are of interest further approximations has to be made. Because it is the initial dynamics that are of interest it can be assumed that the initial state has not changed much. We approximate the time evolution as a linear perturbation of the initial state. For now we only consider small deviations from the the initial state

$$\Psi(r,t) = \left(\begin{pmatrix} \psi_2(r,0) \\ \psi_1(r,0) \\ \psi_0(r,0) \\ \psi_{-1}(r,0) \\ \psi_{-2}(r,0) \end{pmatrix} + \begin{pmatrix} \delta\psi_2(r) \\ \delta\psi_1(r) \\ \delta\psi_0(r) \\ \delta\psi_{-1}(r) \\ \delta\psi_{-2}(r) \end{pmatrix} \right) e^{-i\mu t}. \tag{2.51}$$

Initially only the $|0\rangle$ state is populated and the $|\pm 2\rangle$ components can be ignored. The process $|2,0\rangle + |2,0\rangle \rightarrow |2,2\rangle + |2,-2\rangle$ is much suppressed compared to the process which populate the $|\pm 1\rangle$ states, due to the difference in U_1 and U_2. Finally we assume there is no depletion of the condensate, i.e. ignore the evolution of the $|0\rangle$ component because any decrease in its population will be small compared to the number of atoms in the $|0\rangle$ state. With these approximations

$$\Psi(r,t) = \left(\begin{pmatrix} 0 \\ \sqrt{n_0(r)} \\ 0 \end{pmatrix} + \begin{pmatrix} \delta\psi_1(r) \\ 0 \\ \delta\psi_{-1}(r) \end{pmatrix} \right) e^{-i\mu t} \tag{2.52}$$

Now there is only one scattering channel available for spin changing collisions, $U_{m_F,m'_F,m_f,m'_f} = U_{1,-1,0,0} \equiv U_1$. There are three spin preserving collisions: between a $|0\rangle$ atom and either a

$|-1\rangle$, $|0\rangle$ or $|1\rangle$ atom. These interactions are described by $U_{1,0} \equiv U_{0,1,0,1}$, $U_0 \equiv U_{0,0,0,0}$ and $U_{0,-1} \equiv U_{0,-1,0,-1}$. From [72] it can be seen that $U_{1,0} = U_{-1,0} = U_1 + U_0$.

With these approximations it is possible to arrive at a Hamiltonian for the dynamics [36]

$$\begin{aligned} H = \int d^3r \sum_{m_F=\pm 1} \delta\hat{\psi}^{\dagger}_{m_F} \left(-\frac{\hbar^2}{2m_{Rb}} \nabla^2 + V_{eff}(r) + q \right) \delta\hat{\psi}_{m_F} \\ + \Omega_{eff} \left(\delta\hat{\psi}^{\dagger}_1 \delta\hat{\psi}^{\dagger}_{-1} + \delta\hat{\psi}_1 \delta\hat{\psi}_{-1} \right). \end{aligned} \tag{2.53}$$

Second quantized notation is used meaning that $\delta\hat{\psi}_{m_F}$ ($\delta\hat{\psi}^{\dagger}_{m_F}$) are the annihilation (creation) operators for the m_F state. The first term is an effective eigenstate of the system with spin preserving interactions. The second term describe the spin changing collisions, its strength is given by the effective interaction of the spin changing collisions $\Omega_{eff} = U_1 n_0(r)$.

The effective eigenstate takes the effect of the magnetic field into account through the Zeeman energy. The linear Zeeman energy (p) is of no interest since it is the same for the $|\pm 1\rangle$ states, not changing the eigenstate because of equal $|\pm 1\rangle$ population in this model. It is the q dependence of the effective eigenstate that causes the spin changing resonances investigated.

The effective potential is not dependent on the population of the $|\pm 1\rangle$ states. By tuning the magnetic field it is possible to find a resonance between the energy gained by a spin changing collision and an excitation in the effective potential. The effective potential is

$$V_{eff}(r) = V_{ext}(r) + (U_0 + U_1) n_0(r) + \mu \tag{2.54}$$

The next step towards finding the spin changing resonances is to approximate the effective potential by a box potential. The allowed states of a box potential are Bessel modes and it is these Bessel modes that determine the energy of the resonances. Below the approximation will first be justified and afterward the solution of the effective eigenstate operator will be given.

It is reasonable to ignore the U_1 term in equation 2.54 because $U_0 \gg U_1$. The effective potential is now the effective potential of a single component condensate [31, 73]. The density profile can in this case found by solving the Gross-Pitaevski equation using the eigenstate Hamiltonian giving.

$$n_0(r) = \begin{cases} \frac{1}{U_0}(\mu - V_{ext}(r)) & \mu > V_{ext}(r) \\ 0 & \text{else.} \end{cases} \tag{2.55}$$

The atoms exist at the bottom of the potential and are not able to penetrate beyond the point where $V_{ext}(r) = \mu$. At this position the atoms see a very steep potential wall due to the external potential. It is important to think of the potential seen by the $|\pm 1\rangle$ atoms and not the $|0\rangle$ atoms. It is this potential that is relevant for determining the excitation resonances. There is a repulsive interaction between the $|0\rangle$ and the $|\pm 1\rangle$ states meaning that atoms in the $|\pm 1\rangle$ states will not experience a harmonic potential but instead something more akin to a flat potential for $V_{eff}(r) < \mu$ [35]. Because of this the dynamics are investigated using a square well potential with infinite sides

$$V_{eff}(r) \approx \begin{cases} 0 & r < R_{TF} \\ \infty & \text{else.} \end{cases} \tag{2.56}$$

In our experiment the trap is considered a two dimensional confining potential and the structure of the last direction is frozen out in this first approximation because the energies needed to drive excitations are very large. In the case of an infinite spherical well the solutions to the Schrödinger equation is given in terms of Bessel functions [35, 74]

$$\phi_{nl}(r,\theta) = \frac{1}{\sqrt{\pi} R_{TF} J_{l+1}(\beta_{nl})} J_l\left(\beta_{nl}\frac{r}{R_{TF}}\right) e^{il\theta} \tag{2.57}$$

with eigenenergies

$$\varepsilon_{nl} = \frac{\hbar^2 \beta_{nl}^2}{2m_{Rb}R_{TF}^2} \tag{2.58}$$

The resonance appear when the energy that can be gained through the spin changing collision is equal to the energy needed to excite two atoms into the higher lying Bessel mode. Therefore the energy distribution will show resonances given by the energy of the Bessel modes.

This results in final Hamiltonian for the spin changing collisions as [35]

$$\begin{aligned} \hat{H}_{n,|l|} = {} & (\varepsilon_{nl} + q) \sum_{l=\pm|l|} \left(\hat{a}_{n,l}^{\dagger}\hat{a}_{n,l} + \hat{b}_{n,l}^{\dagger}\hat{b}_{n,l}\right) \\ & + \Omega_{eff}\left(\hat{a}_{n,l}^{\dagger}\hat{b}_{n,-l}^{\dagger} + \hat{a}_{n,l}\hat{b}_{n,-l} + \hat{a}_{n,-l}^{\dagger}\hat{b}_{n,l}^{\dagger} + \hat{a}_{n,-l}\hat{b}_{n,l}\right) \end{aligned} \tag{2.59}$$

where $\hat{a}_{n,l}^{\dagger}$ ($\hat{b}_{n,l}^{\dagger}$) and $\hat{a}_{n,l}$ ($\hat{b}_{n,l}$) are the creation and anihilation operators for the n'th trap mode of Zeeman sub-level $m_F = +1$ (-1).

By the introduction of the quadratures [55]

$$\begin{aligned} \hat{X}_{n,l,1}^{(1)} &= \frac{e^{i\theta_{n,l}}\hat{a}_{n,l} + e^{-i\theta_{n,l}}\hat{b}_{n,-l}^{\dagger}}{\sqrt{2\sin(2\theta_{n,l})}} \\ \hat{X}_{n,l,1}^{(2)} &= \frac{e^{-i\theta_{n,l}}\hat{a}_{n,l}^{\dagger} + e^{i\theta_{n,l}}\hat{b}_{n,-l}}{\sqrt{2\sin(2\theta_{n,l})}} \end{aligned} \tag{2.60}$$

the Hamiltonian (2.59) can be rewritten

$$\hat{H}_{n,|l|} = \frac{E_{n,l}}{2} \sum_{m_F, l=\pm|l|} \left(\hat{X}_{n,l,m_F}^{(1)}\hat{X}_{n,l,m_F}^{(2)} + \hat{X}_{n,l,m_F}^{(2)}\hat{X}_{n,l,m_F}^{(1)}\right) \tag{2.61}$$

where $E_{n,l} = \sqrt{(\varepsilon_{n,l} + q)^2 - \Omega_{eff}^2}$ is the eigenenergy of the full system. Two regimes occur if $\varepsilon_{n,l} + q > \Omega_{eff}$ the eigenenergy is real and the system is stable, the atoms will remain in the $m_F = 0$ state. If $\varepsilon_{n,l} + q < \Omega_{eff}$ the eigenenergy is imaginary and the system is inherently unstable.

To investigate the instability consider the evolution of the quadratures. Using the Heisenberg equation of motion

$$i\hbar \frac{d}{dt} \hat{X}^{(1,2)}_{n,l,m_F} = \left[\hat{X}^{(1,2)}_{n,l,m_F}, \hat{H}_{n,l} \right] = iE_{n,l} \hat{X}^{(1,2)}_{n,l,m_F}. \tag{2.62}$$

From this it is possible to derive the time evolution of the $m_F = \pm 1$ population expectation value. In the final form the expectation becomes [75]

$$\langle n_{\pm 1}(t) \rangle = \sum_{n,l} |\phi_{n,l}|^2 \frac{\Omega_{eff}^2}{|E_{n,l}|^2} \sinh\left(\frac{|E_{n,l}|t}{\hbar} \right) \approx |\phi_{max}|^2 \frac{\Omega_{eff}^2}{|E_{max}|^2} e^{2|E_{max}|t/\hbar} \tag{2.63}$$

where the last approximation assume that the evolution time t is larger than $|E_{max}|/\hbar$. Because of the exponential evolution only the maximal Bessel mode contributes because it dominates the other modes.

Figure 2.3(a) show the instability rate as a function of q. The instability rate is the rate at which the process occur, in this case $E_{n,l}/\hbar$. The different curves are individual Bessel modes. On the right the population after 10 (dashed) and 50 (solid) ms evolution time is shown, illustrating the dominance of certain modes as the system is allowed to evolve for a long time. After 10 ms evolution there are many peaks whereas the spectrum have smoothed out after 50 ms.

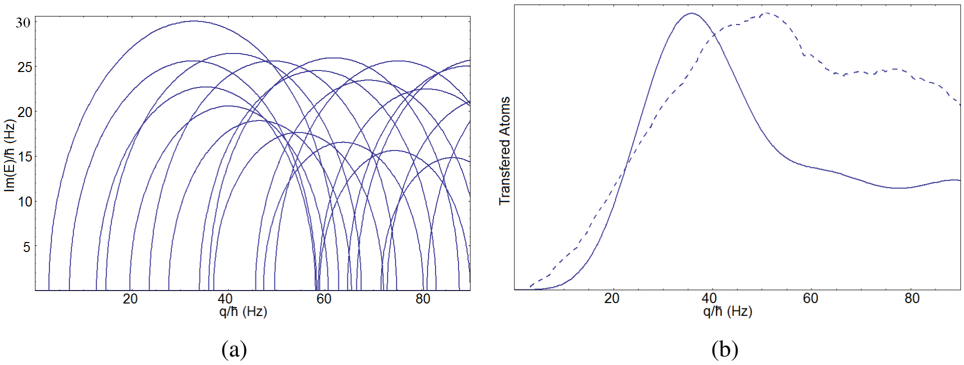

(a) (b)

Figure 2.3: (a) The instability rate as a function of the quadratic Zeeman energy. The different curves are resonances at different excitations of the effective trap. (b) The population of the $m_F = \pm 1$ states after 10 (dashed)and 50 (solid) ms spinor evolution starting from 15000 atoms in the central site of our lattice. The two are scaled curves meaning the peak population at 50 ms is order of magnitude larger than after 10 ms. These figures were created using code provided by the group of L. Santos, Hannover.

3. Experimental Setup

3.1 Creating a Bose-Einstein Condensate

Figure 3.1 illustrates the vacuum chamber with the most relevant sections marked. The chamber is comprised of two sections, the MOT chamber and the science chamber. Originally the experiment was designed to allow for the inclusion of a second atomic species. The design called for two separate MOT areas, to be combined at the cross. To make room for the optics, the three chambers of the experiment were designed with large distances between the different chambers. The second species was never incorporated and the MIX lab next door is a multi-species experiment.

Each sequence is started by collecting thermal rubidium atoms in a magneto-optical trap (MOT) [76]. The trap catches rubidium atoms from a background pressure of $1.3 \cdot 10^{-10}$ torr. The MOT is comprised of a pair of anti-Helmholtz coils and six counter-propagating laser beams. To have reproducible condensate atom numbers a cloud of the same size has to be collected in the MOT for each experiment. This is ensured by a photo detector placed next to the MOT glass cell that measure the fluorescence signal from the cloud. When the signal reaches a preset level the sequence is triggered. The current in the MOT coils is ramped to 300 A and the lasers are turned off. Collecting a cloud of the desired size takes between 3 and 15 seconds depending on how well the system is running. The size of the final condensate has not been observed to depend on the time used to collect the atoms.

In the final stage of the MOT the atoms are optically pumped using σ^+ light into the $|2,2\rangle$ hyperfine state [50]. They are maintained in this state because they are only able to do

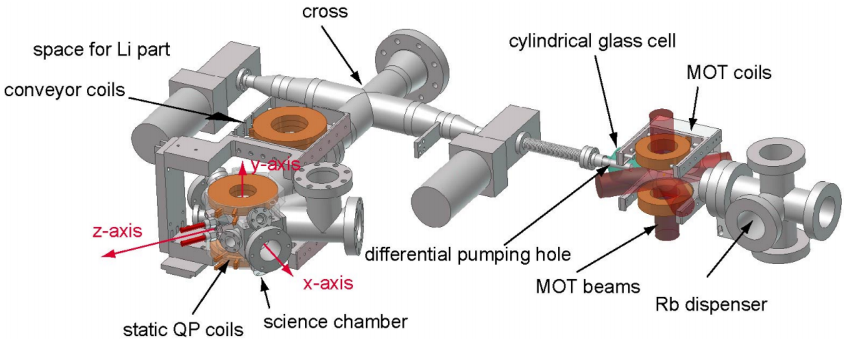

Figure 3.1: An illustration of vacuum chamber with the MOT cell and the science chamber. The image is taken from [77].

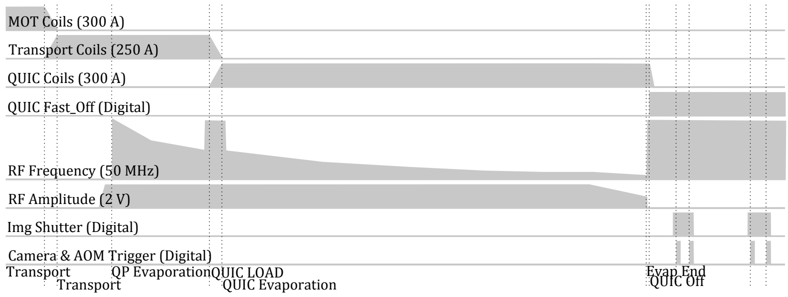

Figure 3.2: The experimental sequence to the point where a Bose-Einstein condensate is created in the magnetic trap. The amplitudes in the illustration are relative to maximal points and digital channels are either open or closed.

Majorana spin flips in the center of the quadrupole magnetic field created by the MOT coils [78].

The transfer from the MOT chamber to the science chamber is done by moving the MOT coils, they are mounted on a computer controlled translation stage. Between the glass cell where the atoms are collected and the cross (see figure 3.1) there is a differential pumping stage. This is a small diameter steel tube that allow us to maintain a pressure difference of two orders of magnitude between the MOT and science chambers. The low pressure is necessary to create a Bose-Einstein condensate. At the cross the atoms are loaded into a second set of coils, similar to the MOT coils, which transport the atoms from the cross to the science chamber. In our normal sequence we transfer $2 \cdot 10^8$ atoms at around 70 μK to the science chamber.

In the science chamber the atoms are cooled by forced evaporation, the hottest atoms are removed lowering the mean temperature of the atoms. To remove the hottest atoms radio-frequency radiation is used to drive transitions between the Zeeman sub-levels of the $F = 2$ hyperfine manifold. In the magnetic trap the atoms are in the linear Zeeman regime, so transition frequencies between the different Zeeman sub-levels are equal. The evaporation drive the transitions with $\Delta m_F = -1$ so $|2,2\rangle \rightarrow |2,1\rangle \rightarrow ...$ The goal of this is to change the Zeeman sub-level from a low field seeker to a high field seeker. These high field seekers are expelled from the trap [50].

Because the magnetic field in the trap is spatially dependent the trapping potential experienced by an atom in the $|2,2\rangle$ state will grow as it moves away from the center of the trap. Atoms with higher kinetic energy can get further away from the minimum experiencing higher fields. The further away from the minimum the bigger the energy split between the Zeeman sub-levels become.By sweeping a narrow band RF source from high to low frequency it is possible to remove the hottest atoms in the trap. If this is done too quickly the remaining atoms are not able to rethermalise and cutting too slowly will lead to inefficient evaporation due to the background pressure [50].

Evaporative cooling is initiated in the transport coils which produces a linear magnetic field gradient. This provides efficient evaporation for a hot atomic cloud. As the temperature is lowered atoms spend more and more time in the center of the trap. In the center they can undergo Majorana spin flips which mean the coldest atoms are lost [50]. Because of this we transfer the atoms to a quadrupole Ioffe configuration (QUIC) trap after 12 seconds evaporation in the transport coils [79].

In the QUIC trap the Bose-Einstein condensate is created by a further 45 seconds of evaporation. The QUIC trap does not have a zero crossing in the center of the trap due to the Ioffe coil producing a gradient magnetic field along the Z-axis of the trap. This lowers the trapping frequency along the axis of the Ioffe coil but it produces a finite magnetic field in the center of the trap [79]. During the time I spent with the group different configurations of the QUIC trap were used to produce condensates and thermal clouds with the desired properties. This lead to a number of different configurations which will be discussed in each section as we go along. The most efficient evaporation is achieved using a QUIC trap where 300 A is run through the quadrupole and Ioffe coils. A bias field of -110 mG is provided along the Z-axis. The axial and radial trapping frequencies of this trap are 17.5(7) and 353(2) Hz respectively. It produce a pure condensate of $1.8(2)10^5$ atoms with a $1/e$ lifetime of $119(10)$ ms and will be referred to as the tight trap throughout this thesis.

Other than the trapping coils there are three sets of bias coils used to create magnetic fields along the three directions of the experiment. These are the shim coils and are used to maintain spin orientation in the lattice, provide an offset in the magnetic field and tune the magnetic field used in the spinor studies. The shim coils will be discussed in section 3.5.

Absorption Imaging

To image the condensate our standard sequence uses absorption images, these are taken using the method described in [80]. From time of flight absorption images information can be gained about the momentum distribution of the sample.

The atomic cloud is dropped from the magnetic trap or optical lattice. After turning off the trap the atoms do a free fall for a variable amount of time between 0 and 18 ms. When desired a laser resonant with the $F = 2 \rightarrow F' = 3$ transition is shone onto the atoms. The atoms absorb the light from the laser leaving a dark spot in the further propagating laser light. This dark spot is imaged using an Andor Xion 885 camera along the X-axis of the system, an Andor Xion 888 along the Z-axis of the system[1] and a DTA Chroma C3 along the Y-axis.

For absorption imaging four pictures are taken. First a picture of the cloud and shortly after a picture of the laser beam itself. A couple of seconds later two bias images are taken, these are without laser light and used to subtract background light and camera noise.

---

[1] The same camera used in the Faraday imaging system.

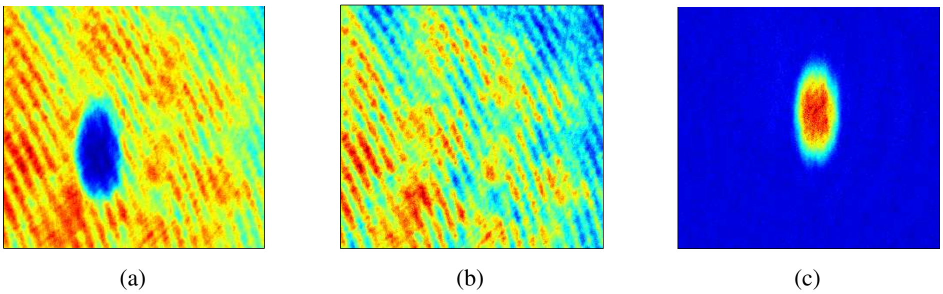

(a) (b) (c)

Figure 3.3: The raw absorption images with (a) and without (b) atoms and the subtracted signal (c). It is clear that the structure of the imaging beam is suppressed in the subtracted picture.

Figures 3.3(a) and 3.3(b) illustrate the two beam pictures. From each of these an unexposed image is subtracted and the ratio of the two gives information about the cloud, figure 3.3(c).

The method used by Reinaudi *et. al.* uses σ^+ polarised light for imaging only driving one transition on the D2 line. This allow for the use of well known imaging parameters which should give improved image quality and allow for reliable imaging of dense clouds with high intensity light. When it is know that the light have the proper polarisation the calibration boils down to the determination of the factor α used to scale the effective saturation intensity $I_{sat}^{eff} = \alpha I_{sat}$. The calibration of α is performed in section 5.3 with the aid of Faraday imaging. The effective saturation intensity takes corrections from different Zeeman sub-levels, imperfect polarisation of the imaging beam and the structure of the excited state [80]. The subtraction of the two images is done by

$$OD_0(x,y) = -\alpha \ln\left(\frac{I_f(x,y)}{I_i(x,y)}\right) + \frac{I_i(x,y) - I_f(x,y)}{I_{sat}} \tag{3.1}$$

where I_f is the image of the cloud with drak counts subtracted, I_i is the image of the beam with dark counts subtracted, $I_{sat} = \hbar\gamma/\pi\sigma_0$ is the resonant saturation intensity and σ_0 is the resonant absorption cross section.

Two methods are used to measure the properties of the cloud dropping from an optical lattice. The first is projection measurements, the lattice is turned off suddenly to reveal information about the momentum distribution of the condensate. In time of flight the condensates from different lattice sites will interfere and give rise to an interference pattern as seen in figure 3.4(a). This interference pattern provide information about the reciprocal lattice, similar to Bragg scattering known from solid state physics. The central peak is atoms with zero momentum while the two peaks correspond to atoms with momentum $\pm 2\hbar k$, in a deeper lattice more peaks would appear [81]. Since this is an interference phenomena the visibility of these Bragg peaks give information about the coherence between different lat-

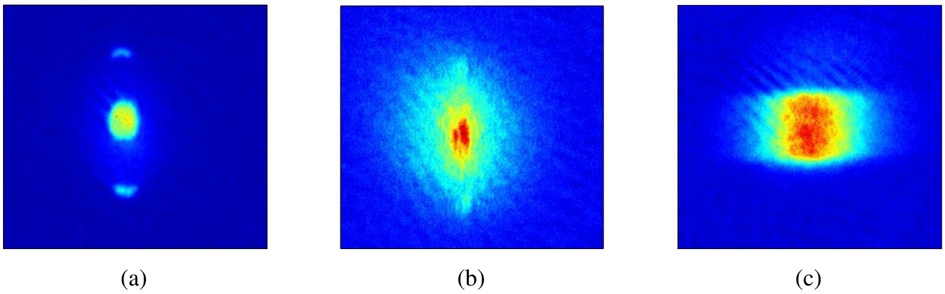
(a) (b) (c)

Figure 3.4: Evaluated images of projection (a and b) and band mapping (c) measurements. The visibility of the projection peaks are a measure of the inter-site coherence of the lattice.

tice sites. If the inter-site coherence is bad the peaks will be less visible as in figure 3.4(b). Here the visibility of the Bragg peaks is very low meaning low inter-site coherence.

Band-mapping is performed by turning off the lattice slowly compared to single particle timescales, but fast compared to the time scales of many body-interactions. This allow for a measurement of the population of the different energy bands. This method was only used to ensure that we only populated the lowest band when loading the lattice.

3.2 Faraday Imaging

The Faraday imaging system uses linearly polarised ligh detuned from the D_2 transition on the order of one gigahertz. The light is produced on the laser table where an extended cavity diode laser is offset locked to the experimental master laser. The Faraday system is described in detail in appendix A of interest here are the offset lock and the acousto-optic modulator.

The offset lock recieve a signal from a fast photo detector (PD2 in figure 3.5(a)) which is mixed with a voltage controlled oscillator. The signal from the fast photo detector is the beat signal of the master and Faraday laser. These two have been combined on a 50:50 beam splitter (S2 in figure 3.5(a)). The speed of the diode makes it act like a low pass filter for the signal, only the beat signal and not the original or added signals are seen. The voltage controlled oscillator can produce a frequency between 400 and 1300 MHz. We can sweep the frequency through 900 MHz by tuning the voltage on the oscillator. The laser frequency is locked to the oscillator using an offset lock. By tuning the oscillator we are able to change the frequency of the laser.

An Acousto-optic modulator is used to determine the length of the pulses. The modulator is double passed (figure 3.5(a)). Double passing the AOM improves the signal to noise ratio of Faraday images and reduces heating by stray light. The suppression of the modulator is three orders of magnitude . The pulses are microseconds long while the cycle time of the imaging system is on the order of milliseconds. If the modulator was only passed

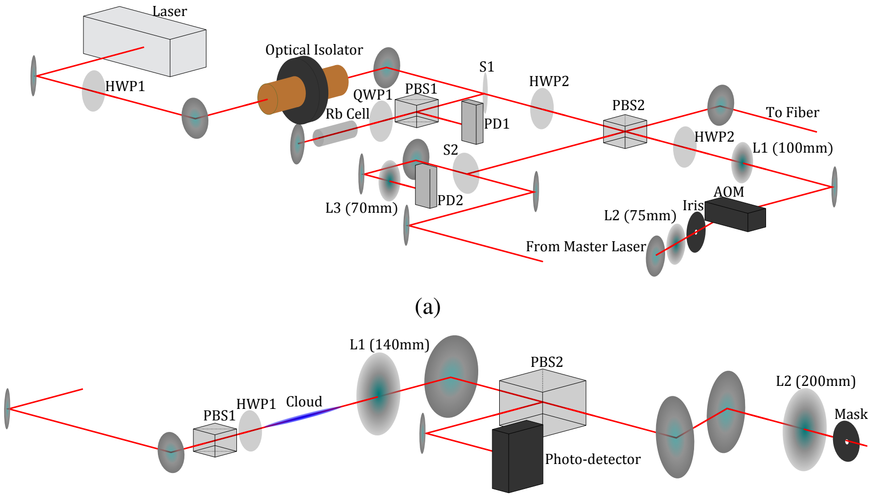

(a)

(b)

Figure 3.5: (a) The Faraday laser system with the Faraday laser and the beating of the two lasers. The signal from PD2 is sent to the offset lock which determine the frequency of the laser. (b) The Faraday system on the experimental table illustrating the beam path.

once the stray light and image signal would be of comparable magnitude. The modulator is turned on and off by a digital switch, controlled by an Agilent 33522A wave form generator . This provide very sharp pulses with a stable amplitude set in the experimental program. The wave form generator is used to determine the length and timing of the pulses. It is programmed by the camera software which calculates the cycle time of the imaging pulses based on frame size and readout speed. The imaging process is triggered by the experimental control system which triggers the camera and the Agilent independently so timings match. The imaging intensity is also set in the experimental control system.

In the experiment each axis have parallel propagating lattice and imaging beams. In figure 3.5(b) the experimental side of the Faraday setup is illustrated. To allow for the easiest possible implementation of Faraday imaging the Faraday light is coupled into the absorption imaging fiber. Switching between absorption and Faraday light is a matter of moving the beam block inserted in the absorption beam. On the experiment table the light is sent through a polarising beam splitter (PBS1) meant to combine the imaging and lattice light. The light passes through the chamber interacting with the cloud. After the chamber a lens (L1 in figure 3.5(b)) collimates the light scattered by the atoms. The scattered light is passed through another polarising beam splitter (PBS2) which separate the imaging and lattice light. The imaging light is transmitted on the cube going onto the camera for imaging. The lattice light hit the retro–reflector and is passed back through the chamber creating an optical lattice in the Z-axis.

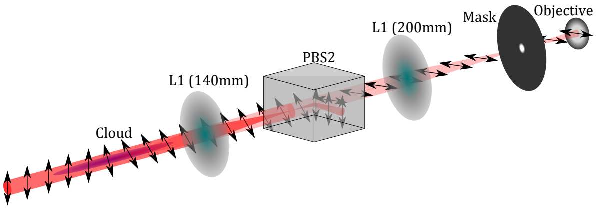

Figure 3.6: The interaction with the atoms and how the rotated light is passed through the polarising beam splitter and the non-rotated light is reflected. The black arrows indicate total polarisation of the light, before the beam splitter the combination of the rotated and non-rotated light.

For Faraday imaging the non-rotated light need to be maximally suppressed on the camera. To do this a half-wave plate was inserted after the first polarising beam splitter. This turn the polarisation 90° meaning that the image light would be reflected and the lattice light transmitted on the second cube. Because of this simultaneous Z-axis lattice and Faraday imaging is not possible[2]. To restore absorption imaging the half-wave plate should be turned so the imaging light is transmitted on the second beam splitter

In the chamber linearly polarised light interacts with the cloud, the interaction rotates the polarisation of the light as described in section 2.1. The light passing through the polarising beam splitter is transmitted or reflected depending on if it interacted with the atoms. The reflected light is sent onto a photo detector while the transmitted light is imaged on the camera. The beam splitter is not perfect so a small fraction of the non-rotated light will be transmitted. The transmitted intensity of the non–rotated light is used to extract information about the intensity of the imaging light at the atoms. This proportionality is expressed as the cube suppression. How the cube suppression is applied in the analysis is discussed in section 5.1.

To measure the cube suppression the maximum and minimum transmission of the cube is measured. First an image is taken with the half-wave plate set for maximum transmission on the cube, using a 2 μs pulse. The next measurement is made with the light polarised so that it is maximally suppressed on the cube, using a 1 ms pulse. To have a measure of the dark counts a region of the chip is blacked out, these dark counts are subtracted from the measurements before they are compared. Different pulse durations are used because a high photon count increases the signal to noise ratio of the measurement. The cube suppression of our system is

$$\Xi = \frac{P_{min}}{P_{max}} = \frac{I_{min}/T_{min}}{I_{max}/T_{max}} = 1.48(3)10^{-3} \tag{3.2}$$

Where $P_{min/max}$ is the minimum and maximum transmitted power on the cube, $I_{min/max}$ the

---

[2] This is only the case due to the original construction of the experiment and could of course be avoided by designing an experiment with Faraday imaging from the start.

mean intensity on the camera, $T_{min/max}$ the duration of the high and low intensity pulses respectively.

Looking at figure 3.6 the light scattered by the atoms is collimated by the lens L1. It propagates through a polarising beam splitter and is focused onto the CCD chip by the lens L2 and the camera optics. In the image plane between the L2 lens and the camera optics a mask have been placed. This is used to prevent light from hitting areas of the CCD chip, we do not want to expose. The system magnifies the image 4.85 times, a combination of the camera optics and the two external lenses. If the system had no magnification the pixel size would be the physical size of each pixel[3]. With our magnification each pixel corresponds to $2.68(6) \times 2.68(6)\ \mu\text{m}^2$ at the position of the atoms.

EMCCD Camera

The main advantage of our system is the spatial resolution. Working at low intensities means extra care have to be taken with the images. The electron multiplying register and effects of the CCD chip caused a number of complications which had to be understood.

The camera read out pixels one at a time using a readout node. The image is shifted to this node by shifting down a row of pixels to the register and then reading these out horizontally. The cameras maximum horizontal readout speed is 10 MHz, limiting the speed at which images can be taken continuously. To gain speed it is possible to crop the camera chip. Only the region specified is read out instead of the whole chip giving a lower cycle time. This mode is illustrated in figure 3.7(b) and allows higher speed of the camera because fewer pixels have to be read for each image. In figure 3.7(b) one problem of this method becomes clear from exposure to exposure charge builds up on the pixels that have not been read off. In a regular Faraday image there might be a mean background intensity around 500 counts per pixel while the signal from the cloud give a pixel count around 5000. Due to the low signal the effect of these multiple exposures become very relevant compared to an image where the signal to noise might be 10000:1. To avoid this effect a mask have been placed in the image plane between the L2 lens and the camera optics blocking light from the rest of the chip, see figure 3.5(b). The effect of the mask is illustrated in figure 3.7(c) where it can be seen that charge is not build up on the pixels.

To overcome the low signal to noise ratio an electron-multiplying charge coupled device (EMCCD) camera amplifies the signal before the readout node. The electron-multiplying register allow us to use short low intensity pulses of light limiting the destructiveness of the measurement. Without the electron-multiplying register imaging pulses of 50-100 μs would be needed to get the same signal 1-4 μs pulses provide with the register.

The quality of the Faraday image is expressed as the ratio of the signal to noise ratio of the image. In a regular charge coupled device (CCD) camera there are two sources of noise.

---

[3] The camera used for the Faraday system is a Andor iXon 888 EMCCD camera with 1024x1024 pixels each $13 \times 13\ \mu\text{m}^2$.

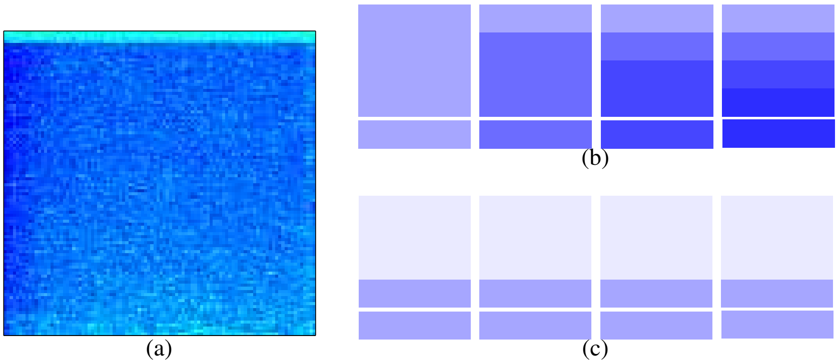

Figure 3.7: (a) On the edge of the specified frame negative effects of the camera become clear. On the upper and right edge there are rows/columns of pixels that are corrupted while intensity gradients show themselves at the lower and left edge of the frame. On the right pictures taken in cropped mode with (b) and without (c) the mask. Each row represent four images taken one after the other. On the top there is no mask meaning the whole chip is exposed in each image, because the whole chip is not read out for each image charge will build up on the pixels that have not been read out. This show itself as a darkening of the chip meaning higher charge on the chip. On the bottom the light is blocked from hitting the chip because of the mask making sure no charge build up on the chip and thereby eliminating the problem.

Noise of the detected signal itself and readout noise. The readout noise is independent of the signal while the inherent signal noise scales with the signal. It is possible to suppress the readout noise by amplifying the signal before the readout node. This is the purpose of the electron multiplying register where signal to noise ratio is improved by suppression of the readout noise. There is a limit at which the readout noise is so well suppressed, compared to the signal size, that higher gain does not improve the signal to noise ratio. In our system this limit is reached at a gain of 150-200.

Working with high magnification makes the images very susceptible to dark counts. Minimising dark counts is one way to increase the signal to noise ratio. Dark counts come from thermal effects in the CCD chip where stray electrons are released by thermal energy. Cooling the camera lowers the energy available thereby lowering the dark counts per second. The camera is cooled to -40°C. Cooling below this gives no improvements in the rate of dark counts for our typical expositions.

Using these methods to improve our images, introduce new unwanted effects. Cropping the image frame causes a number of rows and columns in the top and the right side of the frame to become corrupted. This corruption shows itself as an artificially high intensity as can be seen in figure 3.7(a). The number of corrupted rows (columns) depends on the width (height) of the frame. The wider the frame the fewer rows are corrupted in the top of the image. The corrupted frames are there, even if the camera shutter is closed. It can not be a charge buildup since there is no light. These two effects points to it being an artifact of the cropping done in the camera. This is an unfortunate effect which we have not been able to get rid of it. The corrupted rows and columns are taken into account during the image analysis.

Using the electron-multiplying register also have some unfortunate effects. Many of these were discovered while aligning the imaging system. First the register distorts the images elongating the cloud in the horizontal direction. This show itself as a mismatch of the cloud temperature in the horizontal and vertical directions. The blurring comes from charge building up in the register when reading out the pixels. This is supported by the fact that changing the gain, the light intensity, pre–amplification, pulse duration or vertical shifting speed does not affect the clouds aspect ratio. The only way to change the aspect ratio of the cloud is by changing the horizontal readout speed of the camera. This along with the cloud being round when the electron-multiplying is turned off and on absorption images along the Z-axis, indicate the distortion being an effect of the electron multiplying register. The elongation of the cloud can be removed by using a 5 instead of 10 MHz horizontal shift speed. The EMCCD also amplify intensity gradients at the edge of the chip. This effect is due to the chip not having an even response over the whole surface. The gradients at the edge of the chip are there with and without the electron multiplier, it is amplified by the register making it more visible, see figure 3.7(a). It is worth remembering that these limitations come from our camera and could possibly be avoided with a different camera. These effects are not a problem with the technique but limitations of our system which can be overcome in the analysis and by limiting our ambition for how much we can do at one time.

3.3 Optical Lattice Characterisation

The optical lattice used in these experiments is directed along the Y-axis. We also have lattice capability along the Z- and X-axis. This would allow us to perform measurements in a 3D lattice configuration. For the spinor experiments we are interested in bulk systems and how the trapping potential influence the spin mixing dynamics. A 3D lattice give high trapping frequencies in all directions, freezing out the influence of the trap on spinor dynamics.

The lattice light is produced on the laser table, an extended cavity diode laser is used to produce light at 914 nm. The laser is not locked but an optical cavity is used to ensure that it is single mode. We have the option of locking it to the cavity but it have not been deemed necessary because small drifts of the lattice frequency is not a problem. There are two lasers: the lattice master and the lattice slave. The master laser is used for the Y-axis lattice while the slave laser is used for the X- and Z-axis. For each axis of the lattice a tapered amplifier (TA) is used to increase the power. In the case of the master laser the TA is seeded with 54 mW and produce up to 900 mW of power. A tapered amplifier is a laser diode without the cavity meant to amplify a laser signal. The semiconductor chip is tapered to allow for large amplification, spreading the power over a larger area. The tapering makes it very susceptible to back scattered lightsince this is also amplified. In the opposite direction the cross-sectional area of the diode decreases along the length of the chip, this can lead to a breakdown of the chip.

After the amplifier the light passes a cylindrical lens (L1 in figure 3.8). An optical isolator is used to ensure that no light is reflected back into the amplifier. To control the amplitude and also be able to cut off the lattice quickly an acousto-optic modulator is inserted before the light is coupled into the fiber. The modulator is regulated by a control circuit receiving a signal from a photo detector on the experiment table (PD in figure 3.9). The lattice power fluctuates by less than 0.5%, peak to peak, of the total power.

On the experimental table the lattice beam is passed through an optical isolator, this prevents reflected light from coupling back into the fiber. Afterward a small fraction is split off by the S1 splitter and to provide the feedback signal to the AOM. The light passes through a telescope comprised of lenses L1 and L2 in figure 3.9 widening the lattice beam by a factor of 10 : 3. The waist of the lattice beam is increased to allow for a tighter focus on the atoms. In Gaussian optics the waist of a focused beam is [59]

$$w_0' \approx \frac{\lambda f}{\pi w_0} \tag{3.3}$$

where w_0 is the waist before the lens of focal length f and w_0' is the new waist at the focus of the beam after the lens. The lattice beam is focused on the position of the atoms by the L3 lens after which it passes through the polarising beam splitter PBS1 combining the lattice and imaging light. After the chamber the lattice light is collimated again by the L4 lens and split from the imaging light by PBS2. The lattice is reflected on a retro-reflector and passed

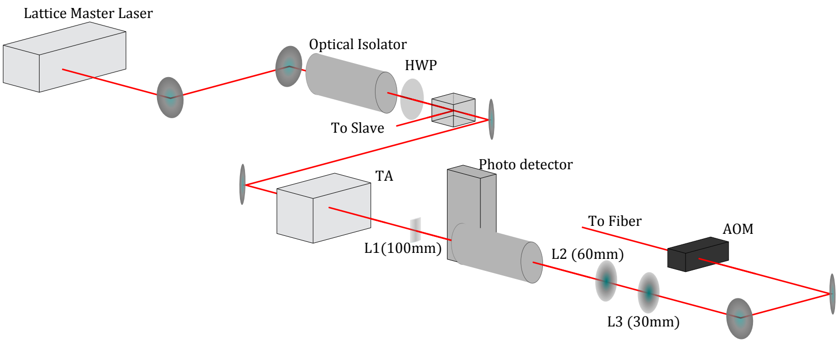

Figure 3.8: An illustration of the Y-axis lattice laser system, the illustration is not exact but include the most important elements.

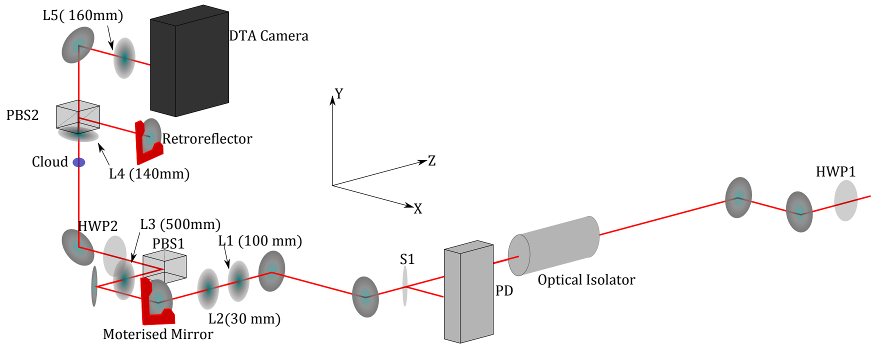

Figure 3.9: An illustration of the beam path of the Y-lattice on the experiment table.

back through the chamber.

In figure 3.10(a) the profile of the lattice beam is illustrated. The calculation was performed using Gaussian optics. The input parameters are the beam waist before the L3 lens (1.43(17) mm) and the focal length of 500 mm. The waist was measured by cutting into the lattice beam after the telescope with a sharp plane, while measuring the remaining power with a powermeter. The power in the beam correspond to the integral of a Gaussian and by cutting into the beam with the razor we effectively change the integration limits. This method can be used to find the width of the Gaussian. The measured and calculated waist of the dipole beam are in good agreement and the large Rayleigh length, 3.51 cm, needed to make the assumptions of identical lattice sites in section 2.1 is fulfilled. To measure the beam profile of the lattice the polarisation of the lattice light was turned so it passed through PBS1. It was measured using a small CCD camera moved along the lattice beam. The beam waist was extracted from the profile pictures taken with the camera. An image of the lattice beam is shown in figure 3.10(b).

A power callibration of the lattice is seen in figure 3.11(a) where the horizontal axis is the set voltage on the AOM. As seen the AOM has a linear response up to 4 V. Above the 4 V set point the system can not reliably deliver enough power. The calibration of the lattice waist and power enable us to calculate the expected lattice depth.

After the chamber the lattice is directed onto the retro-reflector by a polarising beam splitter. This is by no means perfect and therefore there is quite a big loss of power on this, dashed line in figure 3.11(a). Assuming a similar loss to occur each time it passes the beam splitter an effective depth of the lattice can be found. Instead of $(2E_0)^2$ we have $(1.79E_0)^2$ because of this loss when calculating the lattice depth.

The transverse trapping frequency can be used to determine the trap depth, it was determined by observing transverse oscillations, stemming from the loading sequence, with the Faraday imaging system. More on the frequency measurement can be found in chapter 5. The result of the measurement for multiple lattice depths can be seen in figure 3.11(b)

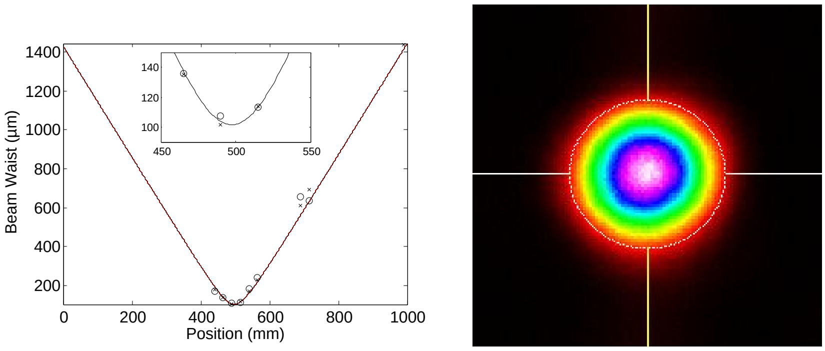

(a) (b)

Figure 3.10: (a) Calculated and measured beam profile of the lattice (b) picture of the lattice illustrating the nice Gaussian profile of the beam.

where the trap depth extracted from transverse oscillations marked is with diamonds. The lines are the expected trap depth case of a perfect lattice (solid) and taking the power loss into account (dashed), based on equation 2.16. For the measured points the frequency have been determined with a sinusoidal fit to the measured oscillations and the lattice depth determined from equation 2.17. The power was determined from the calibration of the AOM shown above.

In the axial direction the lattice depth is determined using loss spectroscopy. The lattice depth is modulated with an AC signal which is applied to the AOM. This amplitude modulation can drive excitation to higher bands [81]. Amplitude modulation can only drive transitions between bands of the same parity. If the modulation drive transitions to bands that are in the continuum of states atoms are lost from the trap. This loss is the signal we are looking for, from the frequency at which the loss occur the depth of the lattice can be calculated. The lattice depth as a function of power can be seen in figure 3.11(b) (circles). For both measurements our theoretical result over estimate the lattice depth compared to the measured depths. The measurements give good agreement with eachother leading us to assume a will known trap depth.

If the lattice is not aligned atoms will be lost during the loading and the cloud will start oscillating. The lattice is aligned by the use of absorption images and alignment has to be performed on both transverse directions individually.

The alignment start with the dipole beam and afterward the retro-reflector is aligned to give an optical lattice. Alignment is done by perturbing the condensate with the dipole beam. A condensate is created in the magnetic trap and released for imaging, usually with 15 ms time of flight. When the atoms are released from the trap the dipole beam is turned on for 2 milliseconds. The light affect the atoms with a force proportional to the transverse intensity gradient. A misaligned dipole beam will accelerate the atoms towards its center.

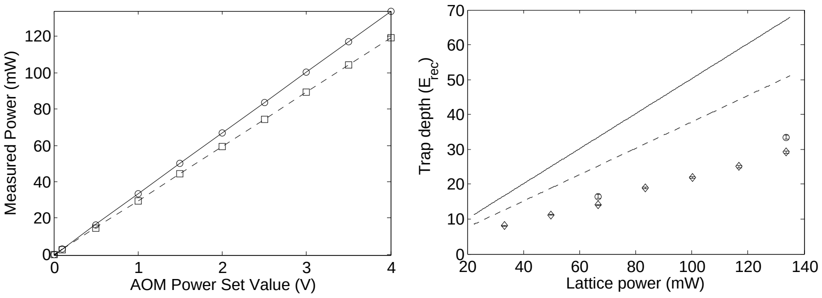

(a)

(b)

Figure 3.11: (a) Power calibration curve of the lattice as a function of set voltage. The solid line is the power entering the science chamber and the dashed line is the power after the beam splitter cube. (b) The expected and measured lattice depth as a function of the lattice power. The solid curve illustrate ideal lattice where power isn't lost while the dashed curve include the measured power loss.

When the atoms are allowed a time of flight before images are taken the effect show itself as a displacement which is proportional to the alignment of the lattice. This can be seen in figure 3.12.

The displacement is caused by the light acting on the atoms with a force proportional to the lattice gradient. This has been illustrated in figure 3.12 showing good qualitative correspondence with the measured dispersion. The zero crossing in the middle correspond to an aligned lattice. When aligned the lattice does not exert a force on the atoms in the magnetic trap. For each point in figure 3.12 an experiment has been performed, afterward the motorised mirror in figure 3.9 is moved which changes the position of the incoming beam relative to the atoms. The motorised mirror is controlled by the computer and moved in steps. Each step is equivalent of turning the screw on the mirror a tiny amount. The graphs use these steps as position axis since it have not been deemed relevant to calibrate the absolute value of a step. There is no interest in partially aligned lattices. This is also why there is only qualitative agreement with the derivative of the Gaussian.

The alignment is performed along both transverse lattice axes and the retro–reflector is aligned using the same approach. The alignment is performed often because a small misalignment causes inefficient loading of the lattice.

3.4 State Preparation

To allow for the observation of spinor dynamics we have to prepare the atoms in the desired state. In our experiment this is the $|2,0\rangle$ state from which we observe spin changing collisions populating the $|2,\pm1\rangle$ states. State preparation is performed using two microwave pulses, where the first drives the transition from the $|2,2\rangle$ to $|1,1\rangle$ and the second drives the

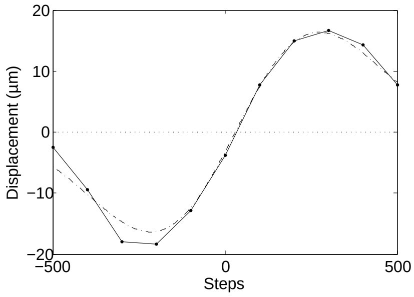

Figure 3.12: Dispersion curve illustrating the alignment procedure of the lattice. The horizontal axis illustrate the steps the lattice is moved which corresponds to an angle and not a length. The solid line is meant as a guide to the eye. It is the gradient of a Gaussian scaled to coincide with the measurements.

transition from the $|1,1\rangle$ to $|2,0\rangle$ state.

The state preparation is performed between the hyperfine manifolds of the $5^2\mathrm{S}_{1/2}$ electronic state. Transitions within an electronic state are driven by the magnetic dipole operator, unlike optical transitions discussed in section 2.1. The electric dipole operator vanishes for transitions inside an electronic state and therefore the magnetic dipole moment is addressed. For optical transitions the electric dipole moment dominates the magnetic dipole-moment [82].

The state preparation is done using microwave pulses of specific frequency and duration. At first the plan was to use microwave frequency sweeps to perform the state preparation. This turned out not to be reliable leading us to use microwave pulses for state preparation instead of sweeps.

In the case of zero magnetic field the hyperfine splitting is 6834.683 MHz [83]. Applying a magnetic bias field breaks the degeneracy of the hyperfine manifolds. The linear Zeeman splitting for both manifolds is $g_F m_F \mu_B B = \pm 0.7 m_F$ MHz/G for the $F = 2$ and $F = 1$ manifolds respectively [83]. The resonance frequency of the first and second transitions change by 2.1 and 0.7 MHz/G with the application of a magnetic field respectively. This field dependence was used to calibrate the shim coils and cancel background fields, see section 3.5.

The natural line-width of the transition should be quite narrow, compared for example with the D2 line-width, because it is a magnetic dipole transition. The transfer is done on resonance, so the atoms perform Rabi-oscillations between the $F = 1$ and $F = 2$ manifolds. For magnetic dipole interactions the probability of the atom being in the excited state is given by

$$P_e(t) \propto \frac{\mathscr{V}^2}{\Omega_R(\Delta)^2\hbar^2} \sin^2\left(\Omega_R(\Delta)t/2\right) \tag{3.4}$$

where $\Omega_R(\Delta) = \sqrt{(\Delta^2 + \mathscr{V}^2)/\hbar^2}$ and $\mathscr{V}^2$ is proportional to the intensity of the radiation

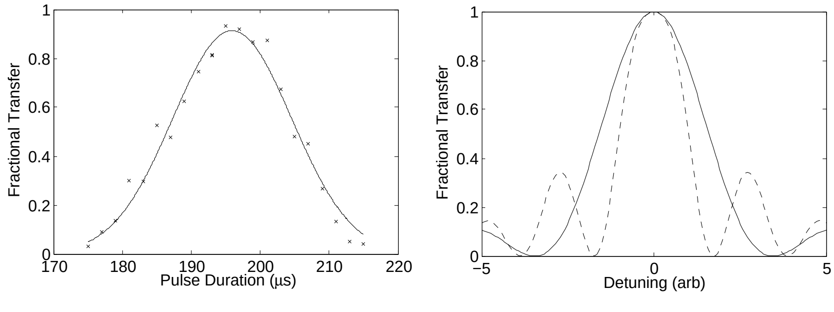

(a) (b)

Figure 3.13: (a) Scan of the resonance with a regular state preparation pulse. (b) Power broadening, the dotted line is twice the power of the solid line. The plot show expected transfer versus detuning, with an arbitrary scaling of the detuning.

field and the magnetic dipole moment [55].

The microwave resonance is illustrated in figure 3.13(a). The width of this resonance is attributed to three factors; power broadening, Fourier broadening and magnetic field noise. Power broadening is illustrated by figure 3.13(b). The solid line correspond to twice the power of the dashed line, the detuning is in arbitrary units. The pulse durations are different for the two resonances shown in the figure so that both are π-pulses. The Fourier broadening is due to the finite duration of the pulse, leading to a brocading of the pulse in frequency space. The width of a square pulse in frequency space scales as $1/\tau$, where τ is the pulse duration. For very short pulses as used in our experiment this leads to a considerable broadening. The final broadening term is the magnetic field noise. There are two relevant time scales for magnetic field fluctuations first there are fluctuations on time scales much shorter than the microwave pulse and secondly there are fluctuations on a time-scale longer than the microwave pulse. The fast fluctuations are the source of the resonance broadening noise while slow changes (on the time-scale of the microwave pulse) in magnetic field are seen as drifts of the magnetic field.

The broadening of the resonance from power and finite pulse length is not a problem in our experiment while magnetic field noise can be. The slow changes in magnetic field can lead to unstable state preparation, moving on and off resonance from run to run. If this instability was large we would not be able to consistently prepare a condensate in the $|2,0\rangle$ state. More on magnetic noise and its influence on the microwave transfer can be found in section 3.5.

The Rabi-oscillations of the two level system is illustrated figure 3.14(a). The detuning can be seen to increase the Rabi-frequency as is also obvious from the above discussion. At the same time a dephasing of the oscillation is illustrated. The dephasing is caused by not all the atoms seeing the same trapping potential. If two atoms are at different position in the potential they will have a very slight change of resonance. In our case the dephasing

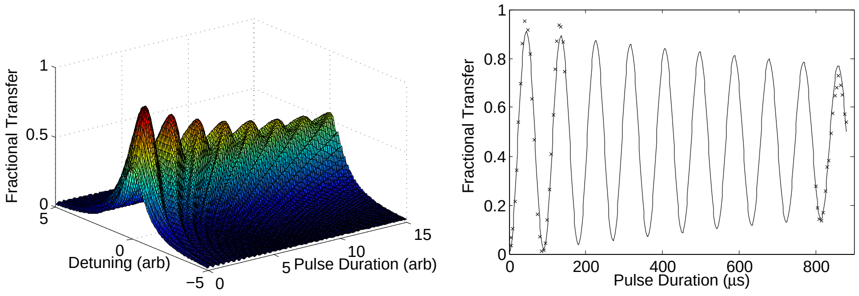

(a) (b)

Figure 3.14: (a) A calculation of the Rabi-oscillation in arbitrary units. The dephasing in this plot is exaggerated to illustrate that in time the oscillation will die out and the population of the two states will be even. (b) Long duration Rabi oscillation, this show the actual dephasing of the Rabi-oscillations in the experiment. The $1/e$ time of the oscillation is 2.2 ms.

of the Rabi-oscillation is very small as can be seen in figure 3.14(b) where we see that the oscillation dies out on time-scales of milliseconds while a π-pulse is on the order of tens of microseconds. If the dampening was comparable to the time needed to make a π-pulse it would not be possible to do the state preparation using microwave pulses.

Microwave Setup

The microwave setup has been a continually evolving system. With time we became aware of problems with the system and found ways of improving it. Both transfer pulses used to be provided by one microwave synthesizer. Quick state preparation was desired because of limited condensate lifetime in the optical lattice. Using one synthesizer limited the speed at which the microwave pulses could be applied. The synthesizer had to be reprogrammed which takes 15 ms. To gain speed we incorporated a second synthesizer to provide the second pulse. The final setup with the two synthesizers is illustrated figure 3.15

The two synthesizers are a Wiltron 6722B and a Marconi 2024. The Wiltron is able to produce microwave radiation between 10 MHz and 12.4 GHz while the Marconi synthesizer provide frequencies between 9 kHz and 2.4 GHz. The Marconi synthesizer has its output frequency tripled by a semiconductor diode. The signals from the two synthesizers are combined using a microwave switch controlled by a digital channel. Between the two microwave pulses this is switched by opening the channel that was previously suppressed. After the switch the signal is amplified 28 dB by a microwave amplifier. This allow us to change the microwave power from 25 to 45 dBm.

Since the Marconi synthesizer is not able to provide the desired frequencies a tripler diode is used. This works in the same way as frequency doubling in quantum optics [59]. Providing a microwave input of 2 GHz the diode produce higher harmonics such as 4, 6

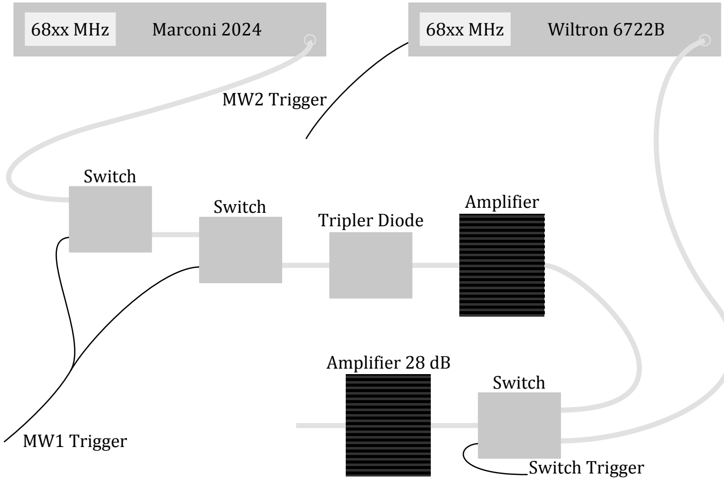

Figure 3.15: An illustration of the microwave setup used to perform the state preparation. The microwave signals are combined using a microwave switch and sent to the antenna which is located inside the chamber. The signal from the Marconi synthesizer is tripled in frequency and amplified before it is combined with the signal from the Wiltron syntheziser.

and 8 GHz, this component has been produced with high and low pass filters removing components other than the third harmonic.

The lengths of the microwave pulses are controlled by the experimental control system. The Wiltron has a digital channel which allow for easy control of the pulse length. In the case of the Marconi this is not possible because its response is highly unreliable when pulse lengths are programmed into the synthesizer. Instead the synthesizer is kept running in a constant mode and the signal is suppressed by two microwave switches in series. These are similar to the one used to combine the two microwave signals. Each suppress the signal around 43 dB at the used frequecy, which is more than enough because there is a lowest signal needed to get a response out of the tripler diode.

The major problem of this system is that the response of the tripler diode is non-linear. This means that the intensity of the tripled signal does not scale linearly with the input intensity, instead it scales as $I_{\omega_0}^3$ [59]. We always work with the same settings producing similar intensity. The tripler diode does not have an immediate response to a signal but a small delay. Despite of this it was decided it was preferable to have the switches before the tripler instead of having the tripler running with a continues input and afterwards switching it on and off. This decision was made because the switches are meant to work in the frequency range 0.5 to 6 GHz therefore giving better suppression in this region. Operating the combining switch at 6.8 GHz has not seemed to cause any problems but unlike the other two switches it is not used to terminate a signal. The signal is amplified by a second microwave amplifier before the combining switch.

	X-axis	Y-axis	Z-axis
Windings	208	64	208
Resistance (Ω)	4.4	1.1	4.2
Inductance (mH)	9.75	0.18	9.0
Coil Calibration (G/A)	3.24(9)	1.720(14)	3.10(1)
Compensation Current (mA)	45	-254	-75
Gradient (G/cm)	<0.005	< 0.02	< 0.01

Table 3.1: Parameters of the shim coils and our field calibrations.

3.5 Magnetic Field Control

Controlling the magnetic fields in the experiment is of great importance to our measurements. The dynamics depend on the quadratic Zeeman shift and the state preparation requires stable magnetic fields. The results of this section are listed in table 3.1.

Magnetic Coils

The shim coils allow us to produce an offset magnetic field along any axis of the experiment. Their configuration is a matter of what is deemed advantageous. The QUIC trap and Stern-Gerlach pulse, used to separate the different m_F states, produce magnetic fields along the Z-axis of the experiment. To avoid any complications that might arise from turning the spin orientation, the first attempt was made with both the X- and Y-directions set to their compensation values and any changes in the magnetic field applied along the Z-axis. Therefore the Z-axis was driven by a Danfysik System 7000 which is faster than the Knürr-Heinzinger PTN 32-10 used on the X- and Y-directions.

The Heinzinger power supplies were selected because they were available and very stable. As a first investigation a current transducer, Danfysik S200, was used to investigate the response of the coils to changes in the set current. First thing to note is the current noise being indistinguisable from inherent noise in the transducer. This high stability had the disadvantage that the Heinzinger supplies have a very slow response to a change in the set value. The 10-90% rise-time was on the order of 280 and 95 ms for the X- and Y-direction respectively. The difference in the rise time of the two come from the much lower inductance of the Y-shim. Because of this very slow response they were set to compensation in the beginning of an experiment and kept there during the full cycle.

The Z-shim had to respond quickly to any desired change in magnetic field. The magnetic field had to be changed quickly after the spin preparation to the desired spin evolution value. The other option was to perform state preparation at the final field for each experiment, meaning a different microwave frequency for every data point. We were interested in performing the state preparation at a fixed field and afterwards changing the field to somewhere between 0 and 3 G. After state preparation the magnetic field has to settle at the

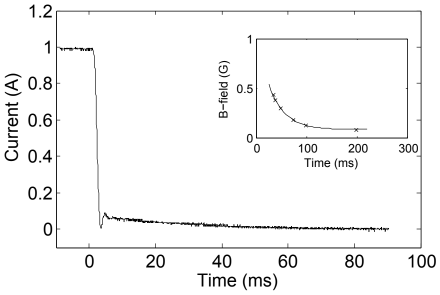

Figure 3.16: The induced field produced by the Danfysik power supply. As can be seen the field goes to zero and then rise to around 7% of the initial field. The inset is a measurement of the decaying field using microwave transitions, the line is an exponential fit.

desired value quickly to ensure a constant magnetic field during spin evolution. The Z-shim had to settle into the desired evolution field in one millisecond, which is based on experince from the Hanover group [36].

The response of the Danfysik power supply is much faster than the Heinzingers. The slew rate of the Danfysik supply is 400 A/s, much faster than we need, the power supply have an unfortunate effect which is illustrated in figure 3.16 where the current in the Z-shim coils is shown as a response to a 100 μs step from 1 to 0 A. The initial response is quite good, going to zero in less than 3 milliseconds, but a current is induced in the coil. The induced current, it turns out, is not a product of the coils inductance but the power supply. From table 3.1 it can be calculated that the $1/e$ time of any induced current should be 2.1 ms, for an RL circuit $\tau = L/R$ [84]. The inset in figure 3.16 show the induced current measured with microwaves. These give a $1/e$ time 31.4(6) ms which is much slower than what would be expected from the coils. The Danfysik supply also show a similar response when driving a pure resistor. The induced current is 6-7% of the initial current and it has not been possible to get rid of this behaviour.

Because the desired behavior could not be achieved with the Danfysik supply it was decided to purchase two HighFinesse current supplies. They have superior response time and should provide good current stability. Because the calculated response of the Z-coils was too slow for spinor work, two supplies were ordered. One was to drive the Z-shim and the other for the Y-shim, with a response time of 164 μs.

Magnetic Field Calibration

To precisely control the magnetic field our shim coils had to be calibrated. The calibration give information about the magnetic fields produced by the shim coils and background magnetic fields. Calibration was performed with microwave transitions from the $|2,2\rangle$ to $|1,1\rangle$ state.

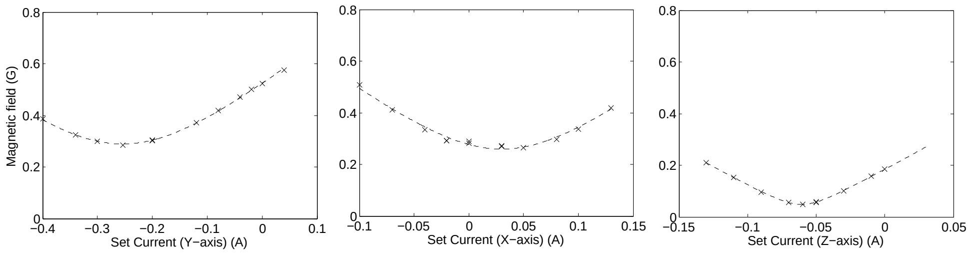

Figure 3.17: Nulling of the magnetic field along the three axis of the experiment. From left to right are the Y, X and Z axis. Each point is extracted from a fit to a scan across the resonance at that specific magnetic field. Any uncertainty would be from this fit which is very small.

The calibration is done one axis at a time, after an axis have been calibrated it is set to the compensation value, i.e. the field minimum along that axis. For each axis the microwave resonance is found for multiple set currents, preferably on both sides of the field minimum. Finding the resonance at one field requires a scan of the frequency, a microwave π-pulse is scanned across the resonance as in figure 3.13(a). From the resonance frequency the magnetic field can be found by

$$B(f) = \frac{2(f - f_0)}{\mu_B \Delta m_F} \tag{3.5}$$

where f is the frequency of the transition, f_0 the hyperfine splitting at zero field and Δm_F the effective difference in the Zeeman sub-level taking the sign of the Landé g-factor into account, in this case $\Delta m_F = 3$.

For each axis a fit was performed using

$$|B(I)| = \sqrt{(a(I - I_0))^2 + B_0^2} \tag{3.6}$$

the fitting parameters a, I_0 and B_0 are the calibration of the coil, the compensation current and the residual field respectively. Using this method the coil calibrations seen in table 3.1 are found. The calibration is illustrated in figure 3.17 where a residual field around 50 mG remains. This was subsequently reduced to less than 5 mG in the present experiment with the values given in table 3.1.

Magnetic Field Noise and Gradients

As mentioned above there are two sources of magnetic noise. The high frequency noise is not much of a problem, it introduces a minimum accuracy of our magnetic field, this can be measured using microwave transitions. In figure 3.18(a) the measurement is illustrated, it is clear that the width of this resonance is smaller than the one illustrated in figure 3.13(a). The difference comes from the use of a 5 ms low power microwave pulses. In this case the

Fourier broadening is less than 1 kHz and the power broadening will also be very small. The full width of this peak is 12.2 kHz which, attributing the full width to magnetic noise, translate into a high frequency noise less than 6 mG. This is in good agreement with the remaining field we observe from the nulling measurements.

Beside the high frequency noise there are slow changes in the magnetic field. These can cause problems with the state preparation because they will shift the resonance from run to run. Slowly changing magnetic fields can be from external sources or because the experiment change as it is run continuously. No evidence of this has been seen when performing state preparation along the Z-axis. Along the Y-axis there are fluctuations so we are not able to perform state preparation along this axis. In this case the state preparation is very unstable which show itself in drifts of the resonance on half an hour time scales. Therefore we can not turn the field along the Y-axis, perform state preparation and then change to the desired evolution field. This would have been preferable to our current method but because of this external instability it is not possible.

It is important that we have no magnetic field gradients in our experiment this would affect the spinor dynamics [37]. To ensure that no gradients are present in the chamber time of flight measurements were used. The atoms were loaded into the lattice and either kept in the $|2,2\rangle$ state or prepared in the $|1,1\rangle$ state, a low and high field seeker respectively. Time of flight measurements were performed along the two horizontal axis if there were no magnetic gradients the acceleration of the two state would be the same. From the position at different times of flight the acceleration along all axis can be extracted. The difference in the acceleration of the two states is proportional to the gradient along the measured axis. From the Breit-Rabi formula the force on the atoms is

$$F = g_I \mu_B m_F \nabla B \tag{3.7}$$

Remembering that $F = ma$ and that effectively there are three Zeeman sub-levels between the two states, opposite sign of the Landé g-factor, the gradient is

$$\nabla B = \frac{2m_{Rb}\Delta a}{3\mu_B} \tag{3.8}$$

where Δa is the difference in the acceleration. The upper limit of the gradients along the three axis is listed in table 3.1. These measurements were made with compensation current applied to the X- and Y-axis and a small field along the Z-axis. If we applied a large field along the Z-axis we would also have larger gradients because the shim coils are not aligned with the atoms. The atoms are a little bit off center of the Z-shim coils which could result in gradients of 0.12G/cm for 1 A current in the coils.

Stern-Gerlach Pulse

To distinguish the different m_F components of the condensate a magnetic gradient is applied along the Z-axis during time of flight. This gradient field is produced by the Ioffe

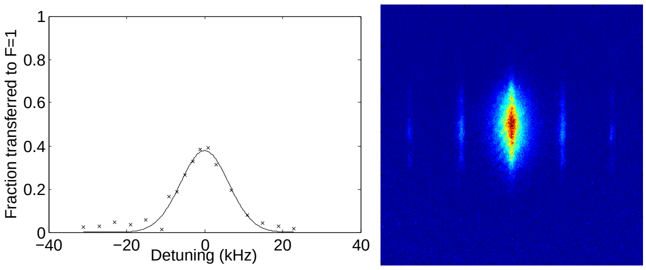

(a) (b)

Figure 3.18: (a) Scan across the microwave resonance on the $|2,2\rangle \rightarrow |1,1\rangle$ transition using low microwave power and long pulses. The maximum transfer is only 50% due to dephasing of the Rabi-oscillaitons. (b) The spinor condensate after time of flight expansion using a Stern-Gerlach pulse. The central peak is the $m_F = 0$ component while the four others are the $m_F = \{-2,-1,1,2\}$ compoenents from left to right, these have been produced by spin changing collisions.

coil running 30 A for 5 ms. The atoms interact for the first few milliseconds after being released and afterwards it can be considered free expansion [85]. Figure 3.18(b) illustrate the different states after the Stern-Gerlach pulse. Pictures like figure 3.18(b) can be used to determine the mean gradient produced by the Ioffe coil during the pulse. The acceleration can be found by considering a system that is first accelerated by a for a time τ_1 and then let fly freely for a time τ_2, the position at time $\tau_1 + \tau_2$, $x(\tau_1 + \tau_2)$ give an acceleration

$$a = \frac{x(\tau_1 + \tau_2)}{\frac{1}{2}\tau_1^2 + \tau_1 \tau_2}. \tag{3.9}$$

In our case after a total 15 ms time of flight of which the first 5 ms had the Stern-Gerlach pulse on lead to a splitting between the different Zeeman sub-levels of 226(2) μm based on the distance from the $m_F = 0$ to the $m_F = \pm 1$ peaks of 7 measurements. Using equation 3.8 gives a mean gradient of 3.34(3) G/cm.

4. Spinor Dynamics

The initial investigations of spinor dynamics are limited to confirming that the spinors behave as expected. We have ensured that we load a condensate into the optical lattice and performed initial investigations of spinor dynamics. We have investigated the time evolution and made first investigations of resonances looking for trap excitations.

4.1 Loading the Optical Lattice

The first step towards observing spinor dynamics was to obtain a condensate in the optical lattice. Different methods of loading and evaporation in the lattice were tested in search of a method that provided satisfactory results. A discussion of different attempted loading procedures can be found in appendix B.

When loading the lattice we have a number of different evaluation points to determine the quality of the loading: first the size and purity of the condensate, secondly minimisation of spatial modes, oscillations or breathing, and finally the coherence between different lattice sites. This last criteria has not been a priority for the investigations presented here. It may become relevant for the investigation of band excitations.

The size of the condensate (atom number) is important because the instability rate scales as the square root of the condensate size, see section 2.2. The larger the condensate the higher instability rates achievable. Higher instability rates and in general higher atom number give better statistics on a single measurement. Higher atom number also decreases the relative importance of atom number fluctuations because of the square root dependence. If the condensate atom number is low, small atom number fluctuations lead to significant changes in the instability rates.

The purity of the condensate has not been a high priority since spin-changing collisions has not been observed in thermal clouds. The only cause for concern is that previously spin domain formation has been shown to be affected by the thermal components [86]. This is not our primary concern and it has been of secondary interest compared to loading large condensates.

When loading a condensate from a cigar shaped trap with its axis of symmetry along the Z-axis to a 1D lattice oriented along the Y-axis avoiding spatial excitations is difficult. The large difference in trapping geometries can induce breathing modes in the condensate and spatial misalignment of the lattice and magnetic trap cause oscillations along the weak trapping directions of the lattice. These effects should be minimised because the kinetic energy available in this spatial motion can lead to excitations in the trap. Since the spinor dynamics rely on trap excitations this could blur possible resonances of instability rates.

Previously the experiment was used to investigate wave-packets [87]. Here a condensate of around $3 \cdot 10^5$ atoms[1] was created in the magnetic trap which was relaxed by lowering the current on the QUIC coils and increasing the bias field. This relaxation was performed in 500 ms resulting in a trap with $\omega_z = 12$ Hz and $\omega_\perp = 40$ Hz. Around this trap the optical lattice was ramped to a depth of $12E_{rec}$. It was under these conditions that the wave-packet work was performed. To observe spinor dynamics the magnetic trap has to be turned off so the different m_F states experience similar trapping potentials. This turn off unfortunately destroyed the condensate leaving a thermal cloud in the lattice.

It was later discovered that our method for turning off the magnetic trap caused the condensate to disappear. The magnetic trap was turned off with the digital suppression switch on the Ioffe branch of the magnetic coils (T2 in figure 4.1(b)). We have later discovered that this method kick the cloud unless the current in the QUIC trap has already gone to zero. The decompression was not tried again after this discovery because it induced oscillations in the trap, making it unlikely to give better results than the method used at the time.

From this point there were two proposed paths to achieving a condensate in the optical lattice. The first was to load the condensate from the compressed trap thereby avoiding the heating and induced oscillations from the decompression and the second to test the possibility of creating a condensate in the lattice, as done by the Munich group [88]. A discussion of this investigation can be found in appendix B. The final lattice loading and state preparation sequence is illustrated in figure 4.1(a). The evolution time is measured from the end of the second microwave pulse.

The lattice is loaded with a 100 ms simultaneous ramp of the QUIC current and lattice intensity. The ramp is compensated by the transistors T2 and T3, see discussion in appendix B, giving a smooth change of the trap. The QUIC is forced off before the ramp is completely finished and 2 ms later the first microwave pulse is applied, with a power of 40 dBm and a duration of 23 μs. This pulse is produced by the Marconi synthesizer. The digital switch is given two milliseconds to switch to the other branch while the remaining atoms in the $F = 2$ manifold are removed by an imaging pulse 20 μs long. Two milliseconds later the Wiltron synthesizer provide the second pulse of 70 μs at the same power as the first one. In total from the end of the evaporation ramp to the start of spinor evolution takes 103 ms. The result is a condensate in the $|2,0\rangle$ state of $5.5(6) \cdot 10^4$ atoms with a purity of $60(6)\%$. This is a lower estimate based on the atom number, in all Zeeman sub-levels, after spinor evolution. The efficiency of both microwave pulses has been measured to be $99(1)\%$ from 20 measurements. We see changes in the final condensate, these are ascribed to drifts of the magnetic field.

No matter which method was used for turning off the QUIC it has not been possible to remove the oscillations from the lattice. They have been reduced as much as thought

---

[1] These measurements were performed before the experiment was moved to its current place.

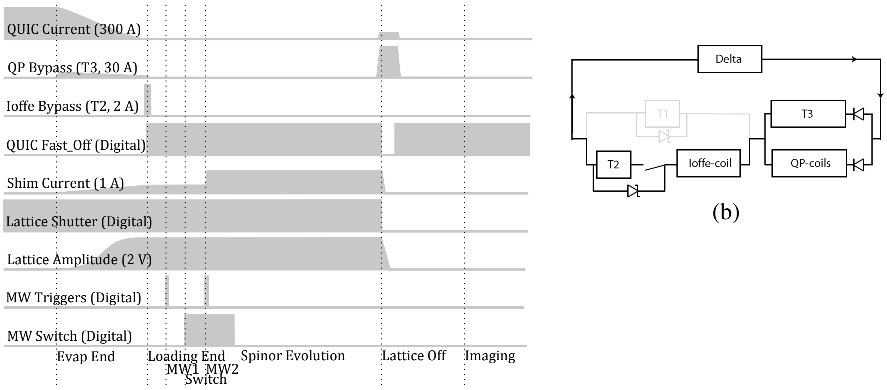

(a)

(b)

Figure 4.1: The control circuit for the QUIC trap. This circuit allow us to regulate the current in the Ioffe and quadrupole branches seperately thereby changing the trapping parameters. An illustration of the lattice loading and state preparation from the end of evaporation to images have been taken, the time axis is not to scale and channels are normalised to their maximum value.

possible, the upper estimate is 8(1) μm peak to peak in the trap. This should be compared with the transverse trapping frequency of 37.8 Hz for the lattice used for spinor dynamics. The energy available from the oscillation can be calculated from $U = \frac{1}{2} m_{Rb} \omega^2 x^2$ giving 16 Hz. This should be low enough that we do not excite spatial modes in the trap.

The imaging pulse used to clear away the atoms remaining in the upper hyperfine state has not been observed to have a pronounced effect as long as the transfer of the first microwave pulse is above 95%. If it gets below this the $F = 2$ atoms leaving the trap will heat the remaining atoms. The atoms in the lower hyperfine manifold are not cleared away, as we do not expect them to contribute to the spinor dynamics.

Lattice Distribution

When the atoms are loaded into the lattice, the magnetic trap is relaxed while turning up the lattice intensity as discussed. The magnetic trap is slowly relaxed until the confinement of the lattice becomes dominant. When taking images of the atoms in the lattice their extent along the Y-axis is 7 μm, so fifteen lattice sites are populated as each site is $\lambda/2 = 456$ nm. In the magnetic trap the atoms are distributed according to Thomas-Fermi statistics, leading to a different population in each lattice site after loading. When the atoms are loaded into the lattice the Thomas-Fermi profile is sliced into sections with a length of one lattice site, see figure 4.2. The figure is not to scale but an illustration of the different atom number in different sites. As a first approximation we assume that condensate fraction is the same in all the sites. It seem more reasonable that the thermal fraction arises when the lattice is dominant since we are able to decompress the magnetic trap without creating a large thermal fraction.

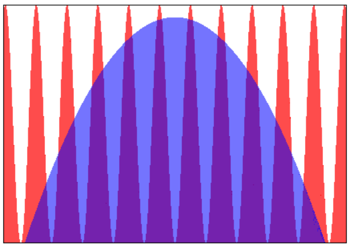

Figure 4.2: Simulation of the distribution of atoms in the lattice. The illustration is not accurate but illustrate a Thomas-Fermi distribution devided between lattice sites.

Different populations of each lattice site is one of the complications of working with a lattice instead of a dipole trap. Because of the different atom number in each site the eigenenergies of the Bessel modes will vary from site to site. This means that a certain magnetic field will be on resonance with one site while not the other. This may lead to no particular mode becoming dominant. Any such problem might be solved with sufficient evolution time, longer evolution time bring other problems such as the break down of the theoretical approximations and saturation of the spin dynamics.

4.2 Time Evolution

As with parametric amplification in quantum optics the spin changing collisions are driven by a seed, either classical or quantum [55, 33]. This initial seed is exponentially amplified until a saturation value is reached. In these initial investigations we have not spend much energy investigating the nature of the seed. There should be no atoms in the $|\pm 1\rangle$ states when spinor evolution is initiated because of the cleanup pulse that has been applied.

If the evolution is initiated by quantum fluctuations there is a spread in time when the evolution is started. Because of the exponential population growth small fluctuations in the seed can lead to large fluctuations in the observed dynamics. These fluctuations will of course decrease again when saturation is reached. The Exponential growth is very clear in figure 4.3(a). It is also clear that large uncertainties for the points on the exponential gets smaller after saturation have set in.

The condensate was produced as described above and state preparation was performed at the value of the evolution field 870 mG. This is not a peak in the instability rate but should be just above the initial peak.

The relative population of the $|\pm 1\rangle$ components seems to decrease quickly after the initial rise in population. This is not spin oscillations but due to thermalisation of the condensate. The relative purity of the condensates in the $|\pm 1\rangle$ components decrease as the condensate is allowed to evolve. For the first 20 ms the condensate is almost completely pure but then a small thermal fraction start appearing and after 40 ms the condensate have

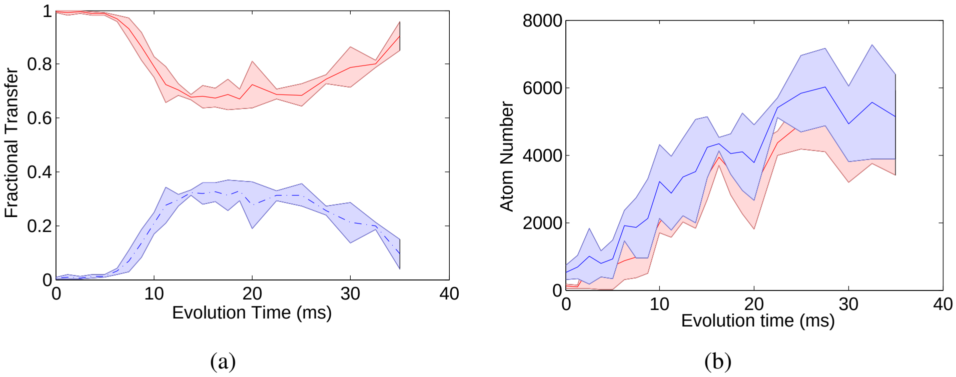

(a) (b)

Figure 4.3: (a) Time evolution of the condensate in the optical lattice. The exponential rise in the beginning is clear and so the saturation of the dynamics. (b) Total population in the $|\pm 1\rangle$ components from the same measurements as (a). The two components are shown separately to illustrate the even population. The uncertainties are standard deviations of 6 measurements.

disappeared.[2] This process is ascribed to thermalisation because we have seen no evidence that thermal atoms performing spin changing collisions. Instead of looking only at the condensate fraction we can include the thermal components. Looking at the total population in the $|\pm 1\rangle$ components, figure 4.3(b), the decrease in population no longer occur. This also explain the increase in the uncertainties again when thermilisation begins to take hold. This indicate that the condensate life-time is on the time scales investigated in our experiments. Increasing the lifetime in the lattice is not the main priority currently because the evolution times we investigate, below 20 ms this is not a problem.

4.3 Magnetic Field Resonances

The goal of the spinor dynamics is to drive trap excitations by tuning the quadratic Zeeman energy. These trap excitations can be used to produce EPR pairs in untrapped states. Here the initial results are presented and a qualitative comparison with theory made.

Initially the plan was to keep the magnetic field oriented along the Z-axis of the experiment. As discussed above this was not possible due to the response time of the Z-shim coil. It was decided to align the spin along the Y-axis during spin evolution. After working with this system for a few weeks we decided to investigate if turning the spin orientation had an effect. The investigation was performed with the a bias field of 675 mG for the state preparation. After the second microwave pulse the Z or Y- shim coils were set to the desired current while the other was kept at its compensation value. A spinor evolution time of 12

---

[2] This time is taken from a different set of data which showed similar tendencies but the scan was conducted to longer times.

ms was used and measurements were made with 15 ms time of flight. The result of the investigation is illustrated in figures 4.4(a) and 4.4(b).

The overall structure of the two graphs show similar trends where the atom number in the $|\pm 1\rangle$ components show a steep increase for q below 30 Hz. For q above 75 Hz the structure is again similar with the instability rate falling off as q increases which is consistent with the theory where smaller overlap between the excited state and the ground-state will lead to a smaller probability of excitation decreasing the instability rate. Around the peak of the spectrum there is a difference where the evolution along Z-axis show a flat peak the other show one point above the others. Since these measurements are preliminary results clear conclusions cannot be drawn from this.

In the measurements performed with the spin orientation along the Z-axis population $|\pm 2\rangle$ components was observed. When the orientation was turned along the Y-axis no such population occurred. This could be an indication that turning the spin orientation affect the observed spin dynamics. This is discussed by Deuretzbacher *et. al.* where the relative orientation of the magnetic field the trap influence the spinor dynamics [37]. It is also not certain that the reorientation of the spin maintaining field is slow enough for the atoms to follow adiabatically.

The production of $|\pm 2\rangle$ states indicate that our theoretical approximation may not be applicable. It does not seem like ignoring the $|\pm 2\rangle$ components is a good approximation even though the dynamics should be on a much slower time-scale than the production of $|\pm 1\rangle$ components. To understand how this population occur we can compare the relative population of the plus and minus components. If the populations occurred due to collisions of two $m_F = 0$ atoms the relative population is the same. If the atoms occurring in the stretched states are due to collisions of two atoms in the $|-1\rangle$ ($|1\rangle$) states collide populating the 0 and -2 (2) states the relative population can be different. Examining the measurements

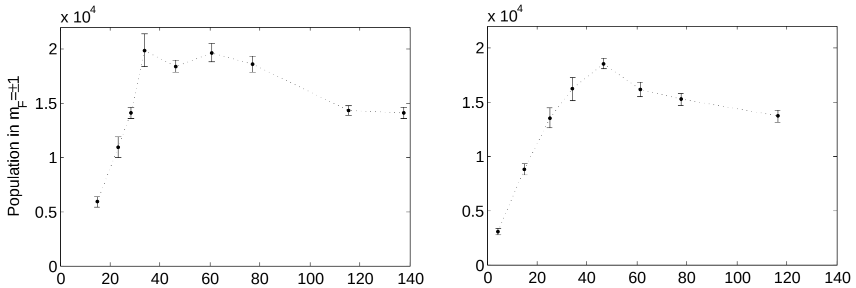

(a) (b)

Figure 4.4: The magnetic field dependence of the spinor dynamics for a magnetic field along the Z-axis (a) and along the Y-axis (b). The uncertainties are standard deviations of 8 measurements.

where atoms appear in the stretched states we have not seen any uneven distribution indicating they are produced by collisions between $|0\rangle$ atoms. The uncertainties are so large that it can not be eliminated that both processes contribute.

As hinted in section 3.5 our shim coils are less than perfect. Ideally they would be Helmholtz coils centered on the position of the cloud. At 1 ampere the Z-shim coils should, according to calculations, produce a gradient of 0.12 G/cm at the atoms. The center of the Z-shim coils are not at the position of the atoms. The Y-shim coils are much better centered on the atoms and closer to a Helmholtz configuration. This means that the two scans of the resonances have seen very different fields where one will se an almost homogenous field (Y-orientation) the other will experience a sizable gradient. Magnetic gradients displace the equilibrium position of the different m_F components. This can severely affect the dynamics of the system affecting the observed spinor dynamics [37].

The fact that we do not observe any clear resonances can be due to the very weak confinement in the transverse direction. In the Hanover experiment the trap had higher trapping frequencies in all three directions (176, 132, 46 Hz)[33, 35, 36]. They observed resonances in the tight trapping directions and therefore more energy was needed to couple the higher trap modes leading to greater spacing of the Bessel modes. This can be the reason for our unresolved spectrum.

5. Faraday Imaging System

First I discuss our evaluation method, calibrations of the Faraday system and finally applications of a working system. A discussion of the importance of an aligned Faraday system can be found in appendix C

The original faraday system was built by Nityanand Sharma. Later the Faraday system was implemented and configured with the experiment by Miroslav Gajdacz. I have worked with Miroslav to characterise the interaction of light and atoms, not a characterisation of the laser system itself.

5.1 Image Evaluation

In figure 5.1(a) a regular Faraday image with evaluation regions marked is presented. The analysis uses the ratio of the signal to the background intensity to determine the rotation angle. The rotation angle can be used to determine the atom number using equation 2.26. The method discussed below is designed for reliable extraction information from thermal clouds. Other methods are used to extract information from condensates and evaluation using the FPGA module for feedback.

Looking at the raw image there is no light on the right most area (region (I) in figure 5.1(a)). The light is blocked by the mask mentioned above. The dark region is used to determine the dark counts produced by the camera. These are subtracted from the signal and the background intensity before the angles are evaluated.

The imaging beam is structured due to optical elements in the imaging path. To take this structure into account a number of images are taken after the cloud have been released from the trap. An average of these beam images is shown in figure 5.1(b). Here the structure of the beam is clear, the region shown corresponds to region (II) in figure 5.1(a). The beam structure is scaled for each cloud image and subtracted to reduce its influence on the evaluation. From the transmitted light it is possible to extract the intensity at the atoms

$$I_{tot} = \frac{I_{min}}{\Xi} \tag{5.1}$$

where I_{min} is the background intensity.

The rotation angle is found by evaluating the cloud profile (region (II) in figure 5.1(a)). The atoms rotate the field polarisation by an angle but the overall field amplitude must be the same. Therefore the intensity as a function of rotation angle is

$$I(\theta) = \frac{I_{min}}{\Xi}\left(\Xi\cos^2(\theta) + \sin^2(\theta)\right). \tag{5.2}$$

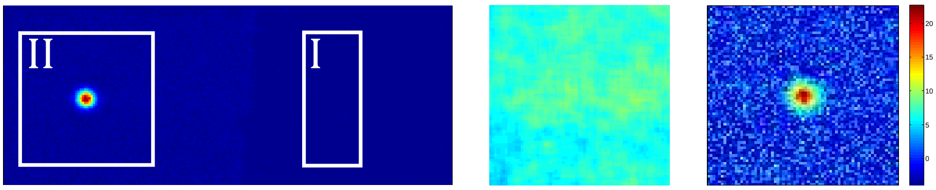

(a) (b) (c)

Figure 5.1: (a) The raw Faraday image, the marked regions are of interest in the evaluation. (b) The beam structure in region (II), a smoothed average of multiple pictures. (c) An evaluated image of the cloud where the colour bar shows the rotation angle in degrees.

It is the electric field and not the intensity that is rotated while the cube suppression is derived from intensity measurements. If the electric field is rotated by an angle θ the field is given as $E^2 = \left(\cos^2(\theta) + \sin^2(\theta)\right) E^2$ when this passes through the beam splitter the non-rotated component is suppressed by the beam splitter giving the above expression. From equation 5.2 the rotation angle is

$$\sin^2(\theta) = \left(\frac{I}{I_{min} - 1}\right)\left(\frac{\Xi}{1 - \Xi}\right). \tag{5.3}$$

The line density $\tilde{\rho}(x,y)$ is proportional to the density profile in the trap, for a thermal cloud this is a Gaussian. A fit is made directly to the intensity profile instead of evaluating the angle for each pixel individually. The fit is made by using the right hand side of equation 5.3 giving the sine squared of the rotation angle. The fit is performed in two dimensions and the maximum rotation angle, Gaussian widths and cloud position are extracted from this. These values are used in determination of the atom number and temperature.

The atom number is extracted from the 2D integrated Faraday rotation $\theta_{sum} px^2_{size} = \theta_{max} 2\pi\sigma_x\sigma_y$ this is devided by equation 2.27 which gives the atom number as

$$N_{far} = \theta_{max} 2\pi\sigma_x\sigma_y \frac{16\pi\Delta_{eff}}{\Gamma\lambda^2 \langle\hat{F}_z\rangle \tilde{\rho}(x,y)} \tag{5.4}$$

where σ_i is the width of the Gaussian in the i'th direction and θ_{max} is the maximum rotation angle in radians.

The temperature is given by the width of the cloud in the trap given as [5]

$$T_{far,i} = m_{Rb} \frac{(\omega_i\sigma_i)^2}{k_B} \tag{5.5}$$

The intensity profile is fitted directly instead of first taking the square-root and arcus sinus because negative pixel counts can occur once the mean background have been subtracted. The noise in the signal is considerable, if the square-root was taken first and afterward a fit was applied the noise would be relatively bigger, due to the steep slope of the square-root function around zero.

There are some limitations to our imaging method. The first limitation is that we are not able to tell the sign of the rotation. A cloud in the $|2,2\rangle$ and $|2,-2\rangle$ states look the same. Secondly we are not able to evaluate rotation angles above 90°. A pixel where the rotation is 70° and one where the rotation is 110° give the same signal. They show the same rotation angle but it is possible to tell the difference between the two due the shape of the cloud. The 110° rotation shows itself as a donuts contour where the highest angle is not in the middle but instead a ring around the middle.

5.2 Characterisation

Destructiveness

The destructiveness of Faraday measurements determine how many times we can probe the cloud without significantly altering it. The photon scattering rate is the measure used to determine the destructiveness. The primary effect of these scattering events are a heating of the cloud, we define a mean heating per scattering event. The observed heating is converted to scattering rate using this heating per event. The scattering rate fall off as $1/\Delta^2$ as can be seen in figure 5.2(b).

To calibrate the destructiveness a cloud of $1.6(2)\cdot 10^6$ atoms at 1.35(11) μK is prepared in the tight magnetic trap. The cloud is held in the trap for 3 seconds and in this time a varying number of Faraday imaging pulses are applied. These pulses have a duration of 4 μs and a power of 275(5) mW. This enable us to determine the heating rate independent of the heating caused by the trap. One complication to this measurement was caused by the magnetic trap. From run to run the cloud temperature is very stable but over time the temperature changes on timescales of half an hour, as illustrated by the large temperature uncertainty. To overcome this changing of the system every second experiment was performed without Faraday light. These were used to correct for any drift in the temperature that might occur. The heating rate per pulse at a detuning of 500 MHz is illustrated in figure 5.2(a) giving a rate of 310(20) μK/s.

For each scattering event the atoms pick up an energy of $2E_{rec}$, see section 2.1. This energy is converted into heating per scattering event using the heat capacity of the atom ($\frac{3}{2}k_B$). The heating per scattering is then

$$T_{rec} = \frac{4}{3}\frac{E_{rec}}{k_B} \tag{5.6}$$

in combination with the heating rate give a scattering rate of

$$\Gamma_{sc} = \frac{310(20)\ \mu\text{K/s}}{T_{rec}} = 1208(102)\ \text{photons/s}. \tag{5.7}$$

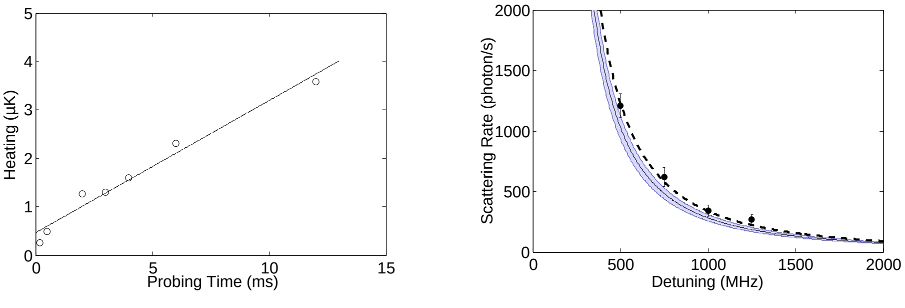

(a) (b)

Figure 5.2: (a) Heating rate versus pulse duration, the points are single measurements. (b) Destructiveness of the Faraday measurement, the uncertainties are fitting uncertainties of the the heating measurements, the fitted curve (dashed) and the theoretical prediction (shaded area) show good agreement. The theoretical uncertainty is due to uncertainty in the power used.

Equation 2.29 gives the theoretical scattering rate

$$\Gamma_{sc} = \frac{3\pi c^2}{2\hbar\omega_0^3}\left(\frac{\Gamma}{\Delta}\right)^2 \frac{2P}{\pi R_x R_y}, \tag{5.8}$$

R_i is the width of the beam in the i'th direction, $R_x = 1096(4)$ μm and $R_y = 1195(5)$ μm. The detuning is an effective detuning from the $F = 2$ to $F' = \{1,2,3\}$ transitions. All three transitions can be driven by the σ^- coupling of the light while the σ^+ component can only drive transitions to $f' = 3$. Taking the widths of the different transitions into account [83] the detuning becomes

$$\frac{1}{\Delta^2} = \frac{1}{\sqrt{2}\Delta_{2,3}^2} + \frac{1}{\sqrt{30}\Delta_{2,3}^2} + \frac{1}{\sqrt{12}\Delta_{2,2}^2} + \frac{1}{\sqrt{20}\Delta_{2,1}^2}, \tag{5.9}$$

$\Delta_{F,F'}$ is the detuning from the transition from the F hyperfine manifold in the $S_{1/2}$ state to the F' hyperfine manifold in the $P_{3/2}$.

At a detuning of 500 MHz from the $F = 2$ to $F' = 3$ line the theoretical scattering rate is 1032(97) photons/s. The uncertainty in this number arise from uncertainty in the power and beam waist.

In figure 5.2(b) the scattering rate at four different detunings have been measured. A fit to these give the dashed line while the shaded area is the theoretical scattering rate during our Faraday measurement. The agreement of the measurement and the theoretical prediction is within 15%.

Faraday Coefficient

Like the destructiveness the Faraday coefficient, given by equation 2.27, is dependent on the detuning. To investigate this detuning dependence of the Faraday coefficient the detuning

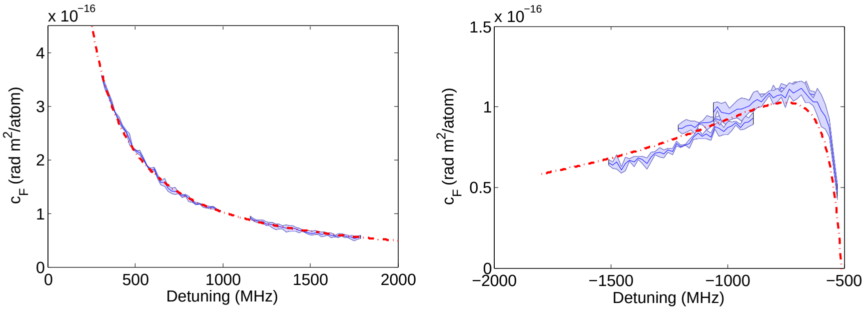

(a) (b)

Figure 5.3: Faraday coefficient of blue (a) and red (b) detuned Faraday imaging away from resonance. The theoretical curves (dash-dotted) have been rescaled by and overall factor of 0.635 and 0.786 for the blue and red detuning respectively. The shaded regions represent standard deviations of three measurements.

is changed while taking images. The detuning is swept by changing the set voltage of the voltage controlled oscillator. 50 images with a cycle-time of 4.7 ms are taken using imaging pulses of 1 μs with a power around 350 mW, detuned 750 MHz from the $F = 2 \rightarrow F' = 3$ line. With these settings the atom number does not change significantly during a measurement.

The experimental value of the Faraday coefficient is given as $c_F = \theta_{sum}/N_{abs}$, where θ_{sum} is the integral over the 2D Gaussian we have fitted to the intensity profile. We see that the signal fall off as $1/\Delta$ for both the blue and red detuned probing, figures 5.3(a) and 5.3(b) respectively. Unfortunately there is an overall discrepancy between the theoretical (dash-dotted line) and measured (shaded region) Faraday coefficient. The theoretical curves have been scaled to coincide with the measured Faraday coefficient. The rescaling of the red and blue detunings are 0.786 and 0.635 respectively.

In the single particle picture there is no difference between red and blue detuning. To explain the different scaling molecular formation on the red detuned side has to be taken into account [54]. Kaminski *et. al.* measured on the red detuned side where they saw a signal higher than expected from the single atoms model, discussed in section 2.1. This correlates well with our measurement of a higher relative signal on the red detuned side. In a dense atomic gas the single particle picture is no longer valid. The dipole-dipole interaction between two atoms close to each-other have to be taken into account. The electronic energy levels of two such atoms are shifted, leading to light induced resonances [82]. This leads to molecular formations which increase the rotation angle. We are still trying to understand the overall scaling coefficient and it will be discussed later in combination with atom number and temperature measurements. For now it is worth noting the overall detuning dependence is as expected and the discrepancy between the two sides can be attributed to an increased signal on the red detuned side due to molecular formation.

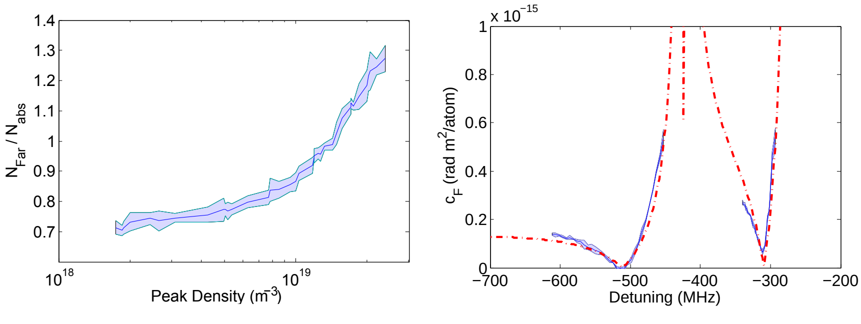

(a) (b)

Figure 5.4: (a) Density dependence of the Faraday coefficient on the red detuned side, a clear dependence of the density is visible. (b) Resolving the zero-crossings using Faraday imaging, the measurement show good agreement with theory.

The formation of molecular rubidium is density dependent while the Faraday coefficient is not. A measurement was made of the Faraday coefficient at varying density, see figure 5.4(a). As a function of density the Faraday coefficient rises with the density expected from two-body effects. This effect is not observed on the blue detuned side, see next section, which supports molecular formations as the source of the discrepancy.

Finally behaviour of the Faraday coefficient close to resonance was investigated. The actual resonances are at $\Delta = \{0, -266.65, -423.597\,\mathrm{MHz}\}$. The Faraday imaging have been used to examine the regions between the resonances. The fact that multiple hyperfine levels contribute to the signal also contribute to the splitting. At certain frequencies the contribution from all three lines combined will add to zero rotation meaning the signal disappear. This happens at two points, which we have resolved with the Faraday imaging system as illustrated in figure 5.4(b). The figure show the norm of the Faraday coefficient because we are not sensitive to the sign of the rotation only the magnitude. The interesting point is how well we can resolve the zero crossing, if our frequency was wrong the error would be most obvious at the zero crossing. There is good agreement of the Faraday coefficient around the zero crossings except for the overall scaling of 0.786 applied because we are working on the red detuned side.

Atom Number and Temperature

This section is focused on the blue detuned interaction, this avoids the complications of molecular formation. Our investigation show that the Faraday imaging is able to reliably extract temperature and atom number data from thermal clouds.

Above it is discussed that the Faraday atom number is given by the Faraday coefficient times the total rotation of the light. This ratio should be valid no matter the cloud, no assumptions about density or temperature have been made in the derivation of the Faraday effect. The agreement of Faraday and absorption images for varying density, atom number and temperature is a good check of the validity of our imaging method.

The atom number and temperature measurement was performed using thermal clouds, varying from $1.5 \cdot 10^7$ to $1.6 \cdot 10^6$ atoms at 30 to 1 μK in a weak trap, 191.7(1) and 17.5(6) Hz in the radial and axial directions respectively. The investigation spans three orders of magnitude in phase-space density as shown in figure 5.5(b). The Faraday probing was done with 6 pulses of 1 μs each with a cycle time of 4.69 ms. The imaging light was detuned 750 MHz from resonance and the camera amplified the signal using an EM-gain of 50. After the initial 6 pictures the cloud was released and the absorption image was taken. After the release from the trap another 14 Faraday pulses were shone onto the camera. These pulses were used to eliminate any structure in the beam. The cloud was exposed to additional Faraday light in time of flight, which could minimally distort the absorption image and the heating is on the order of 2 nK. This effect is ignored because it is less than our sensitivity. The trap used is not capable of producing condensates[1], but provides a better spatial profile of the cloud than the tight trap. In the tight trap a cold thermal could have a width around 10 μm or 4 by 4 pixels on the camera. This give bigger uncertainties in the fitting routine and therefore the weaker trap was used.

The ratio between absorption and Faraday temperature and atom number, see figure 5.5, is constant over three orders of magnitude in phase-space density. This indicate that Faraday images are a reliable source for extracting both atom number and temperature information from a thermal cloud. The atom number measurement show a ratio of 0.65(3) which is the same ratio as was found for the Faraday coefficient. This coefficient therefore indicate an inefficiency in our Faraday detection system or an evaluation error in our Absorption atom number. This contribution is independent of atom number, detuning and density and does not agree with the observation made by Kaminski *et. al.* who observed a signal higher than theory [54]. This indicate it being a problem with our system and not the overall method.

The temperature have been extracted using equation 5.5 where the width have been extracted from the fits used to find the atom number. The evaluation gives a ratio of the temperatures extracted from Faraday and absorption images of 0.82(9). Within the precision of our absorption measurement uncertainty this can be considered a good agreement.

Condensate Formation

All experiments discussed above were conducted using thermal clouds. It was decided that thermal clouds were preferable to the condensate because the Faraday signal dropped drastically around the condensation point, see figure 5.6(a). The figures on the top are Faraday images of the cloud along the evaporation ramp. As can be seen there is a steady deterioration of the signal as the condensation point is crossed. The Faraday image only have one pixel with high intensity and the rest are very low. Along with this the peak

---

[1] the evaporation efficiency is too low.

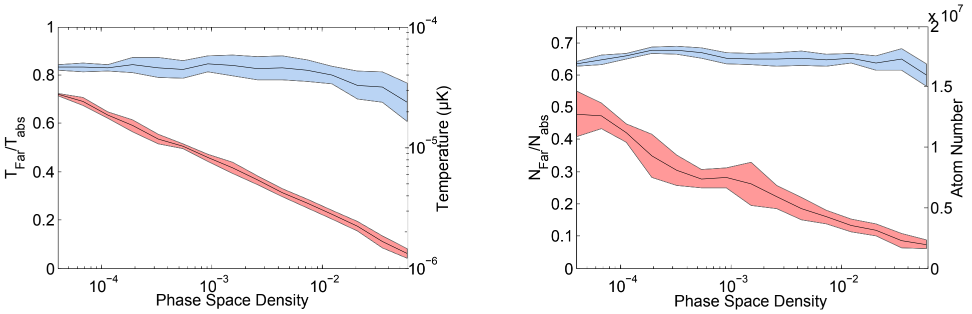

(a) (b)

Figure 5.5: Temperature and atom number comparrison between Faraday and absorption imaging showing good agreement (blue). Shown is also the absolute temperature and atom number extracted from absorption images (red).

rotation caused by the condensate is less than 10 degrees making the measurements very susceptible to noise. The noise is also more clear in the condensate image than the two images of thermal clouds where it is almost indistinguishable.

The measurement was taken with the same Faraday parameters used to measure the thermal and atom number ratios for thermal clouds and the method of taking pictures is also the same. The magnetic trap used is the decompressed trap discussed in section 4.1 creating a condensate of $1.3 \cdot 10^5$ atoms. In this trap the Thomas-Fermi radius is 6.9 μm so the whole cloud is only 5 pixels across which agree well with the image in figure 5.6(a). Because of the tight confinement in both directions we can not hope to resolve any bimodal structure as we can with absorption imaging along the X-axis. A thermal cloud in the same trap at 1 μK have a width of 7 μm, using equation 5.5. At condensation the temperature is on the order of 100 nK meaning the cloud is even smaller.

We are not able to gain much by higher magnification, the diffraction limit for our system is 2.66 μm [59]. So the effective pixel size is already at the diffraction limit. Higher magnification gives a smoother distribution on the camera but the resolution is not improved.

Because the cloud is so small and the shape of the condensate in the trap is not a Gaussian, a different evaluation method was used. For each pixel the rotation angle was extracted and the total rotation angle, and thereby the atom number, is the sum of the rotation over the whole image. The agreement between this method and the absorption images is illustrated in figure 5.6(a). The scaling factor is different from the thermal cloud measurement, this is attributed to a different evaluation method. The rise in the ratio for the condensate can be ascribed to a noise. The dash-dotted line is the condensate fraction and is there to show the onset of condensation.

In figures 5.6(b) the absolute Faraday atom number and maximum rotation angle are

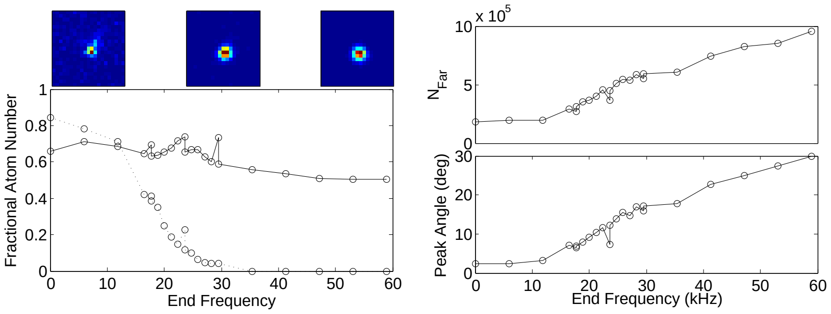

(a) (b)

Figure 5.6: (a) Faraday vs. absorption atom number (dashed) for evaporation across the BEC transition, the the condensate fraction (dash-dotted) illustrate the onset of condensation. The fluctuations are an indication of the worse signal and evaluation method used in this experiment. The figures on the top are Faraday images taken 0, 30 and 60 kHz above the trap bottom. (b) On the top total Faraday atom number and on the bottom the the peak rotation angle vs. absorption atom number.

illustrated. Looking at these there is not clear indication of the condensation. This along with the unlikeliness of a bimodal distribution we presently do not have any indication that the cloud is Bose-Einstein condensed.

5.3 Applications

There are a number of applications for the Faraday imaging system. Some applications decrease the time needed to performcalibrations of the system. Others are interesting because they allow us to monitor something we haven't been able to monitor before or allow us an extra check of our methods.

Absorption Image Calibration

One really useful application of the Faraday imaging method is to speed up absorption imaging calibration. A description of the absorption imaging system and image evaluation can be found in section 3.1 [80]. It is the determination of α that can be speed up by the use of Faraday imaging by eliminating atom number fluctuations from run to run.

The method used by Reinaudi *et. al.* rely on doing absorption images at multiple different imaging intensities, keeping the photon count constant. The higher the intensity the shorter the pulse, our measurement of α spans two orders of magnitude in imaging intensity (0.4 to 9 I_{sat}) while the pulse duration is varied from 1000 to 9 μs giving an average pixel count of $2.65(14)\cdot10^3$. For each chosen intensity multiple absorption images are taken in order to eliminate shot to shot atom number fluctuations. The optical depth as a

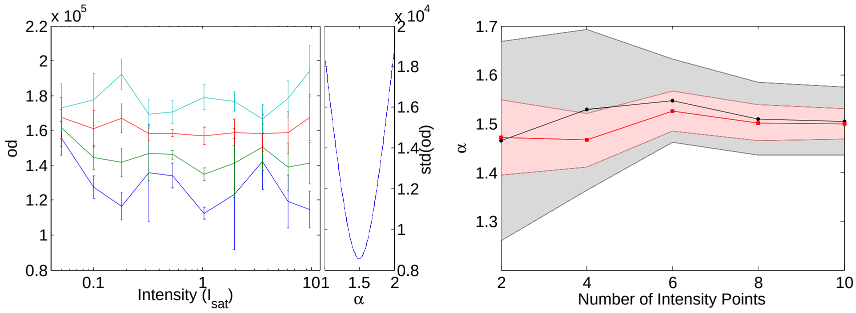

(a) (b)

Figure 5.7: (a) The standard α determination introduced by Reinaudi *et. al.* where the optical density as a function of intensity for different values of α are illustrated. On the right the standard deviation of the optical density as a function of alpha. (b) An illustration of the advantage provided by normalisation using Faraday images.

function of the intensity has been plotted for a number of different α values in figure 5.7(a). The correct α minimises the variations of the optical depth over the whole intensity range. This minimisation is shown on the right side of figure 5.7(a) giving $\alpha = 1.50(7)$.

In our method we remove shot to shot fluctuations of the atom number by taking 10 Faraday pictures each run. Each Faraday pulse is 2 μs long amplified using an EM-gain of 200 and the cycle time is 2.437 ms. Unlike the absorption images the Faraday parameters are not changed from run to run. The Faraday images scale the absorption images, eliminating run to run atom number fluctuations. It is irrelevant that the Faraday and absorption atom number does not correspond exactly since there is just a scaling factor between them.

We are able to achieve a good alpha calibration by only taking the points of highest and lowest intensity. An interesting way of illustrating the advantages of Faraday scaled absorption image calibration can be seen in figure 5.7(b). Here the α is shown as a function of how many different intensity points are used. With Faraday rescaling using two intensities give a resonable measurement of α while using two intensities give large uncertainties in the pure absorption method. From figure 5.7(b) we arrive at $\alpha = 1.50(3)$.

Using this fast α-calibration method allows us to quickly investigate the effect of changing absorption imaging parameters. α was measured for a number of different pulse durations, both high and low intensity pulses were scaled accordingly. This showed a tendency of α to reach a minimum at a mean pixel count of 2000. In figure 5.8(a) α as a function of the mean pixel count is shown. This indicates a dependence of α on the overall photon count, the imaging system have to be re-calibrated whenever such a change is made. The interpretation of this is that the effective saturation intensity changes with the overall photon count, warranting further investigation. It is not clear why the effective saturation intensity depends on the overall photon count.

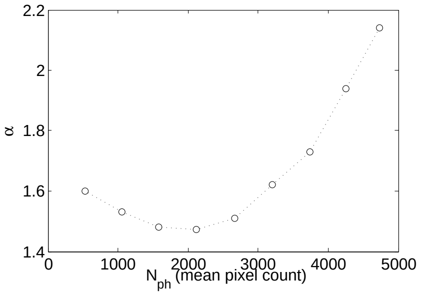

Figure 5.8: (a) Measurement of α vs. overall photon count, this show a clear dependense of α on the photon count.

Trap Characterisation

The Faraday imaging system has been used to monitor the cloud in the magnetic trap. We have investigated trapping frequencies, stopped deterministic oscillations and monitored the trap decompression online measuring the changing trapping frequency in a single run. This makes the Faraday imaging system very useful in determining trapping parameters and monitoring the trap characteristics.

When working with trapped ultra-cold gasses one of the most important parameters to know is the trapping frequency. The trapping frequencies are used to extract information from cloud images and determine relevant timescales for atomic dynamics. The trapping frequency can be determined in multiple ways such as: cloud oscillations, parametric heating and expansion of a thermal cloud. All of these measurement require multiple iterations of the experiment and all are sensitive to fluctuations from iteration to iteration.

With the Faraday system we are able to take up to 2000 images of the cloud in a single run and thereby determine oscillations in one run instead of 20-30 runs meaning we are not sensitive to fluctuations from iteration to iteration. The technique also allows for a quick measurement of trapping frequencies if the parameters of the trap have been changed. Both of these points have been a great help when trying new trap configurations or changing the system in some other way. It also allowed a measurement of the transverse trapping frequency of our optical lattice which was not possible with absorption images due to non-deterministic oscillations.

A measurement of the trapping frequency is shown in figure 5.9(a) where the frequency is determined as 222.44(7) Hz in a single run. The cloud is set oscillating by turning off the trap for a short time (70 μs) with the digital off switch discussed in section 4.1. The imaging is started before the cloud is set oscillating. With our current setup we are only able to determine the transverse trapping frequencies of the magnetic trap because Faraday images are taken along the axis of the QUIC trap. The points in figure 5.9(a) were taken with imaging pulses of 1 μs with a cycle-time of 0.401 ms. To achieve this high speed we

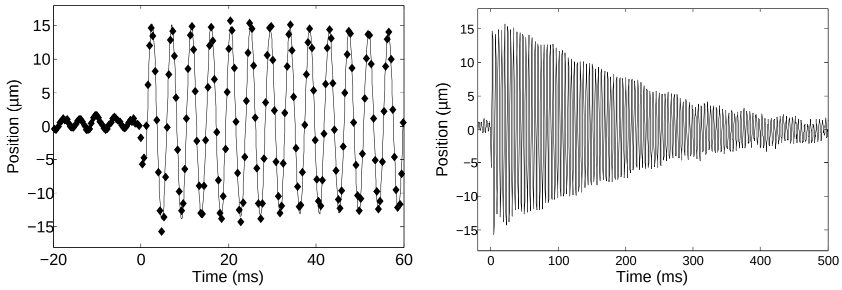

(a) (b)

Figure 5.9: (a) The first 60 ms of the cloud oscillating in the trap. (b) Full oscillation sequence showing the dampening of the oscillation.

use a horizontal shift speed of 10 MHz thereby blurring the cloud, a very small frame of 80 by 18 pixels is used making accurate fits difficult. This is an unfortunate limitation of our system but is only relevant when we are trying to achieve very high speed. The high speed was determined necessary to get a good frequency measurement.

Looking at figure 5.9(b) the whole sequence is resolved, figure 5.9(a) are the first 60 ms of the oscillation. The oscillation is dampened out with a $1/e$ time of 213.5(15) ms. This dampening is ascribed to the trap not being a perfect harmonic potential. The dampening correlate to an increase in temperature because the spatial motion is transferred to heating of the atoms. Due to the high imaging frequency we can not reliably extract the absolute temperature of the atoms. It is possible to monitor the heating rate because the blurring seems to be a factor of two on the cloud size. This is illustrated in figure 5.10(a) where the the temperatures extracted from the Faraday images are shown. Both of these have been fitted with an exponential giving $1/e$ time of 190(2) and 190.0(14) ms for the Y- and X-axes respectively. The higher heating rate compared to the dampening can be explained by heating from the Faraday pulses. The heating rate is 153(19) μK/s at a detuning of 750 MHz, which has to be taken into consideration.

Before the kick the cloud is already oscillating, see figure 5.9(a). The goal of the spatial motion measurements is to allow the Faraday system to identify oscillations inherent to the trap and stop these. That we are able to resolve these small oscillations is encouraging for this long term goal. As a first step towards stopping such oscillations an atomic cloud was set oscillating and after a number of oscillation cycles it was stopped again. How the actual implementation will be done is not finalised but one method is to use the Faraday imaging to determine frequency, amplitude and phase of the oscillation, then stopping it by a perturbation of the trapping potential of a proper size, direction and timing.

As a demonstration of the feasibility of this method we performed a stoppage of deterministic oscillations. The oscillation is started by turning off the magnetic trap for 70 μs at

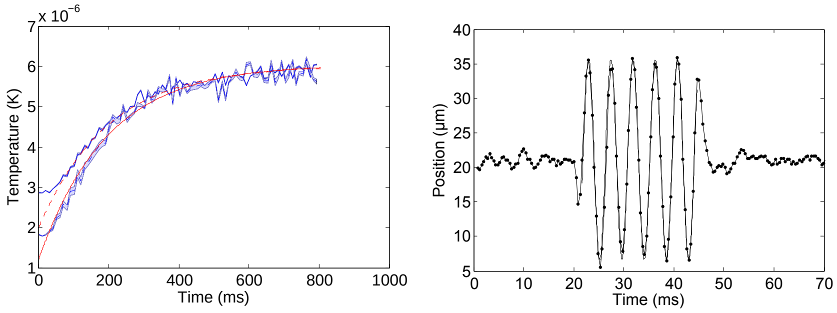

(a)

(b)

Figure 5.10: (a) Heating of the cloud during the oscillation measurement. As can be seen the initial temperature of the two directions disagree but they give the same heating rate. (b) Illustrating our ability to stop start and stop spatial motion.

time $t = 0$ s, as done above for the trap frequency measurement. In figure 5.10(b) the cloud is then stopped after five and a half oscillations by turning off the trap for 70 μs again. The Faraday and trapping parameters are the same as for the trapping frequency measurement. In this measurement we demonstrate that we are able to measure the frequency and phase well enough from Faraday images to stop the oscillation again. Because we use the same kick for starting and stopping the oscillation we are not sensitive to the amplitude of the oscillations. We are able to determine the timing of a new perturbation to stop the cloud at a different time. Our method only allows the so called bang bang stoppages but the hope is that in the future we will be able to install an FPGA to provide on line analysis and feedback to the system.

We are able to decompress the trap by lowering the current in the Ioffe and quadrupole coils. This relaxation changes trapping frequency and the cloud sags due to gravity. We can measure the change in trapping frequency during the decompression with the Faraday system allowing us to monitor the change of the trap as we change the current. This is very useful in trying to reach shortcuts to adiabatic decompression as attempted by J. F. Schaff *et. al.* [89]. They calculate how the trapping frequencies change during the decompression and then try to reconstruct this using their magnetic trap. They need to perform multiple measurements to establish that the frequency changes as they expect it to. With the Faraday imaging system we are able to determine the trapping frequency during the whole decompression in a single run where they just sampled certain points in the decompression. This allows for a fine-tuning of the decompression and the possibility of achieving even better results than they did.

The measurement of the oscillations was performed in a similar manner to the trapping frequency measurement. A larger frame, 80 by 50 pixels, was used to allow for the sag of the cloud. Again the could was set oscillating by forcing the magnetic trap off for 70 μs. 60 ms

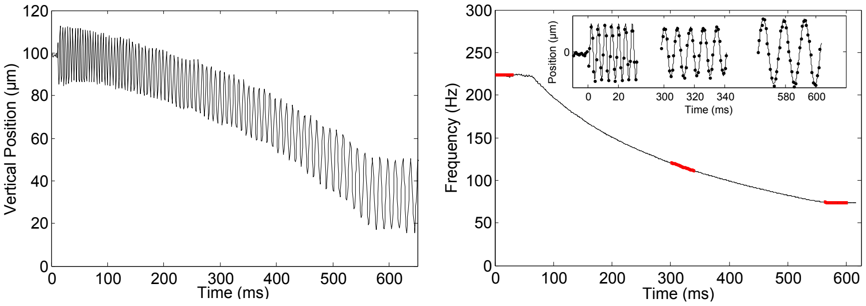

(a)

(b)

Figure 5.11: (a) An illustration of the position of the cloud along the vertical axis of the experiment during the decompression. It is clear that the frequency changes during the decompression and the change in position can be ascribed to gravitational sag and a movement of the magnetic field minimum. (b) The frequency along the decompression extracted from figure (a). It also show the fitted frequencies for three points along the decompression.

after the kick the decompression starts. The decompression is a linear ramp of the current in the QUIC trap from 300 to 200 A in 500 ms. At the same time the current in the Z-axis bias coils is raised from -0.945 to 1 A. During the decompression the central position of the cloud moves and the oscillation frequency changes, figure 5.11(a). This change in frequency is evaluated by fitting small sections of the oscillation at a time, 5 periods, moving over 1 period and performing a new fit. This chirped fitting allow us to determine the frequency of the oscillation through out the decompression. This is illustrated in figure 5.11(b) where the frequency vs. time is plotted. The figure includes uncertainties which is a testament to how accurate these fits can be made by using only a few periods. The red markings along the decompression are the time periods whose oscillations are plotted in the inset of figure 5.11(b). These show a closeup of the frequency during the decompression where the different frequencies become very apparent.

Investigations in an Optical Lattice

Since the central point of our experiment is the optical lattice we tried imaging a thermal cloud in the lattice. The outcome of this was a magnetic field nulling method that allow for a calibration of the magnetic fields in far fewer runs then the method used in section 3.5. The Faraday imaging was also used to determine the trapping frequency in the lattice as described in section 3.3. This method used the same principles as discussed for the frequency measurement in the magnetic trap, except we didn't have to initiate oscillations.

First there was an investigation of the alignment of the lattice where we used the Faraday imaging to monitor the lattice loading and the checking for oscillations after the lattice have been loaded. The lattice alignment does not benefit from the use of Faraday images in our current system since we are unable to move the mirrors directing the lattice beam together with running the experiment. If such a turn was possible we could turn the incoming lattice beam while imaging the cloud. We would be able to see the alignment of the lattice by the effect it has on the cloud in the trap. If the equilibrium position of the magnetic trap is known, the incoming or reflected lattice beam could be swept through this position while taking images with the Faraday camera. After the sweep the mirror could be turned to the position where the lattice beam was in the equilibrium position during the sequence. This requires a major change to our system and have not been investigated because we have problems with the motorised mirrors.

The transverse trapping frequency of the lattice was measured for multiple lattice settings by Faraday imaging. This was done because we were not able to perform a measurement using absorption images. Non-deterministic fluctuations in the turn off of the magnetic trap caused oscillations which did not seem reproducible. This allowed us to measure the transverse trapping frequency and from it extract the lattice depth as discussed in section 3.3. The final application of Faraday Imaging is magnetometry. The Faraday rotation is

proportional to the expectation value of the collective atomic spin operator along the imaging axis $\langle F_z \rangle$. If we now orient the magnetic field along a direction that is transverse to the Z-axis, the Faraday signal go to zero, provided the atomic spins follow the field direction adiabatically. This can be exploited to calibrate the magnetic fields along the two transverse directions and find the zero point along the imaging axis. The field is rotated by applying a static bias field along the Y-axis and sweeping the Z-field through the zero point.

Ignoring field gradients the and assuming the field along the X-axis to be zero the total magnetic field is

$$\vec{B}(t) = \sqrt{B_z(t)^2 + B_y^2} \tag{5.10}$$

the magnetic field along the Z-axis is assumed to change in time. The expectation value of the Z-axis spin operator is proportional to the relative projection of the field along the Z-axis, i.e.

$$\langle F_z \rangle \propto \frac{B_z(t)}{B(t)}. \tag{5.11}$$

In our measurements we apply a field along the Y-axis and set our X-axis to its compensation value. The current in the Z-axis bias coils is swept from 300 mA in 30 ms. While sweeping the field 50 Faraday images are taken with a cycle time of 1.4 ms. This allow each Faraday picture to be assigned to a magnetic field value, each experiment produce a curve like figure 5.12(a). At zero field the signal disapear, the width of the dip depends on the transverse field. The dashed line in figure 5.12(a) is a fit to the measured data from which the transverse field and the zero point of the Z-field can be determined. This fit predicates the knowledge of the calibration of one of the magnetic fields. In our case we assume to know the calibration of the Z-field and therefore the we only gain information about the transverse field. If the transverse field was know a calibration of the Z-field is possible. The

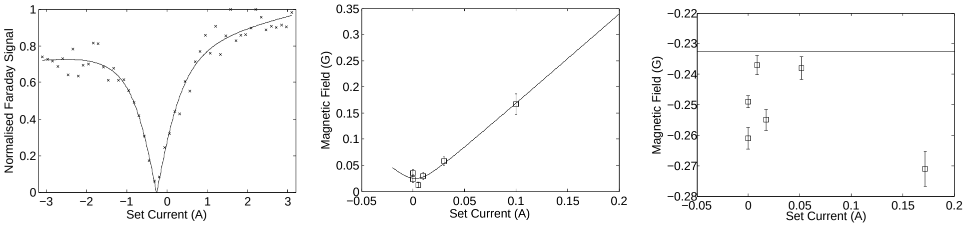

(a) (b) (c)

Figure 5.12: (a) The magnetic field is swept across the zero point along the imaging direction leading to a drop in the faraday signal which depends on the transverse field. The dashed line is a fit using equation 5.12. (b) Field nulling performed using Faraday measurements instead of microwaves. Uncertainties are from fitting. (c) The position of the field zero along the imaging axis, as extracted from the fitting routine deviates from the zero point found by microwave calibration (solid line).

reason both can not be determined in this method is because both B_z and B_y can be scaled without changing the signal.

The fitting is done with

$$e^{-\beta t}\frac{|B_z(t)-B_{z0}|}{|\vec{B}(t)|} \tag{5.12}$$

the exponential decay takes loss of atoms into account. This loss is both from the destructiveness of the measurement and atom loss from the lattice. By setting different transverse fields it is possible to calibrate the transverse shim coils. Figure 5.12(b) show the magnetic field extracted from Faraday images plotted against the set transverse field. The dotted line is a fit of the kind performed in section 3.5. It gives a calibration of the Y-shim of 1.7(2) G/A, in good agreement with the microwave calibration performed in section 3.5. The field zeroing is not as accurate with an uncertainty three times the actual value. This could have been fixed better by going to opposite polarity on the Y-shim to achieve a better calibration. This was not done since it is only a proof of principle measurement.

We also look at the zero point determined from the individual measurements. This can be seen in figure 5.12(c) where the zero point as determined by microwave calibration is presented as the dotted line. This shows that we underestimate the field zero along the Z-axis and that this is not a very accurate measure. The measurement is very sensitive to fluctuations because a few points around the zero point, where the noise is already most significant, can change the position of the zero point. This do not affect the curvature of the fit which determines the transverse field.

6. Conclusion and Outlook

Both investigations presented here show encouraging results prompting further investigations. In the future the goal is to pursue both research direction in parallel.

The progress towards observing trap induced spin changing collisions in an optical lattice have progressed at a steady pace. We are able to currently reliably prepare the atoms in the $|2,0\rangle$ state and accurately control the magnetic field. Problems identified and to be improved upon include fluctuations in magnetic field along the Y-axis and short condensate lifetimes in the optical lattice. Having observed spin changing collisions with the expected signature is encouraging. The agreement with theory is one of the current directions of investigation. There are a number of elements we still need to understand for an accurate comparison with theory. The theory is based on programs developed by the Group of Luis Santos. These programs are based on the theory covered in the beginning of the thesis and therefore are only applicable in the linear regime where changes in the $|0\rangle$ state population are negligible. In the currently experimentally achievable region the theory dos not show any clear resonances, we may not be able to observe well resolved resonances as done by Klempt *et. al.* [36, 33]. There are also experimental imperfections, already discussed, that can be the cause of not observing resonances.

One goal is an increased resolution of the magnetic field resonances in an attempt to observe their structure. To achieve this experiments with lower atom number are an option, the widths of the instability modes decrease and the energy between the modes increase. Next efforts will be towards providing better input parameters to the theory in an attempt to increase the correspondence with the most recent measurements.

Currently work is progressing towards imaging the spatial structure of the excited modes. This is to investigate if we populate the Bessel modes as done in [35]. Because multiple lattice sites are populated we can only hope to resolve modes with $l = 0$. Phase differences between lattice sites would blur modes of higher l. Based on theory the first mode we can resolve is the $n = 3$ mode. The $n = 1$ mode is almost indistinguishable from the Thomas-Fermi profile and the instability rate of the $n = 2$ mode is dominated by the $n = 1$ mode. These measurements will also benefit from a better correlation between theory and measurements because they allow us to determine what modes we are looking for at a specific field.

The long term goal is to reach the limit where lattice structure and even super-fluid properties affect the spinor dynamics. The first experiments will investigate the excitation of atom pairs to higher lattice bands and another is the effect of the lattice on the dynamics. The next important experimental step to observing these excitations is to produce large enough magnetic fields to give the required Zeeman energy. Driving these excitations would require a magnetic field on the order of 15 G. In this region we should have a number of resonances available in the transverse direction. This would lead to a resonances structure similar to the one at low fields. To produce this field the current plan is to use the transport coils in a Helmholtz configuration. In the long term the deep lattice regime provides an interesting setting for investigating two dimensional dynamics. The shallow lattice would unlock the band structure of the lattice allowing for the production of EPR pairs and the investigation of spinors in even more complex geometry where the different lattice sites interact through tunneling. As with the two dimensional case this regime has not yet been explored.

Faraday imaging has been demonstrated to be a reliable method for extracting information about the cloud and also a useful tool in our everyday lab work. We have been able to demonstrate the properties of our imaging system and learned its limitations. The calibration of the Faraday system shows that we have a reliable method for imaging a thermal atomic cloud. For a Bose-Einstein condensate the atom number can still be reliably extracted while more precise evaluation is difficult due to the small size of the clouds. We also observe that the Faraday system behaves as expected in regards to detuning and destructiveness of the light. Numerous applications of the Faraday system have been shown. Some mimic the properties of regular absorption imaging while others are not even possible with absorption imaging. It has been shown that Faraday imaging improves the calibration of absorption imaging systems, allows for monitoring trapping parameters and their change due to perturbations. The Faraday imaging technique also has applications in magnetometry.

There are two planned directions of future work: online feedback and examination of a Bose-Einstein condensate. Both of these require further improvements to our system. To observe a condensate in the trap we may have to increase the atom number and improve the resolution of the imaging system. The feedback work is currently in its preparatory phase, where an FPGA module is being programmed to read images from the camera, evaluate these and provide a feedback to the atoms during the experiment. This should allow for feedback to our evaporation sequence and also to minimise trap oscillations. The first goal is to provide feedback to the evaporation cycle. The goal is to remove atom number fluctuations in the final condensate with this method.

In conclusion both subjects of my thesis show promising first results and indicate the prospect of future research in both directions. The initial spinor results encourage further theoretical and experimental work. The speed and reliability of the Faraday system encourage future work in this direction.

Bibliography

[1] M. H. Anderson, J. R. Ensher, M. R. Matthews, C. E. Wieman and E. A. Cornell - Science, 269 198 (1995).

[2] K. B. Davis, M. O. Mewes, M. R. Andrews, N. J. van Druten, D. S. Durfee, D. M. Kurn and W. Ketterle - Phys. Rev. Lett. 75, 223969 (1995)

[3] C. C. Bradley, C. A. Sackett, and R. G. Hulet - Phys. Rev. Lett. 78, 060985 (1997)

[4] A. Einstein, B. Podolsky and N. Rosen - Phys. Rev. 47 777 (1935)

[5] C. J. Pethick and H. Smith - Bose-Einstein Condesation in Dilute Gases, Cambridge, second edition, 2008.

[6] S. N. Bose - Z. Phys. 26, 178 (1924)

[7] A. Einstein -Sitzungsberichte der Preussischen Akademie der Wissenschaften 1: 3 (1925)

[8] P. Kapitza - Nature 141, 3558, 74 (1938)

[9] J. F. Allen and A. D. Misener - Nature 142, 3597, 643. (1938)

[10] F. London - Nature 141, 643 (1938) and Phys. Rev. 54 947 (1938)

[11] C. E. Hecht - Physica 25, 1159 (1959)

[12] W. C. Stwalley and L. H. Nosanow - Phys. Rev. Lett. 36, 910 (1976)

[13] D. G. Fried, T. C. Killian, L. Willmann, D. Landhuis, S. C. Moss, D. Kleppner and T. J. Greytak - Phys. Rev. Lett. 81, 3811Ű3814 (1998)

[14] A. G. Truscott, K. E. Strecker, W. I. McAlexander, G. B. Partridge and R. G. Hulet - Science 291, 2570 (2001)

[15] S. Jochim, M. Bartenstein, A. Altmeyer, G. Hendl, S. Riedl, C. Chin, J. Hecker Denschlag and R. Grimm - Science 302, 5653, 2101 (2003)

[16] Markus Greiner, Cindy A. Regal, Deborah S. Jin - http://arxiv.org/abs/cond-mat/0311172v1

[17] M. W. Zwierlein, C. A. Stan, C. H. Schunck, S. M. F. Raupach, S. Gupta, Z. Hadzibabic and W. Ketterle - Phys. Rev. Lett. 91, 250401 (2003)

[18] M. R. Andrews, C. G. Townsend, H. J. Miesner, D. S. Durfee, D. M. Kurn and W. Ketterle - Science 275, 5300, 637 (1997)

[19] M. R. Matthews, B. P. Anderson, P. C. Haljan, D. S. Hall, C. E. Wiemann and E. A. Cornell - Phys. Rev. Lett. 83, 2498 (1999).

[20] C. Chin, R. Grimm, P. Julienne and E. Tiesinga - Rev. Mod. Phys. 82, 1225 (2010)

[21] C. J. Myatt, E. A. Burt, R. W. Ghrist, E. A. Cornell and C. E. Wieman - Phys. Rev. Lett. 78, 040586 (1997)

[22] D. S. Hall, M. R. Matthews, J. R. Ensher, C. E. Wieman and E. A. Cornell - Phys. Rev. Lett. 81 081539 (1998)

[23] D. M. Stamper-Kurn, M. R. Andrews, A. P. Chikkatur, S. Inouye, H.-J. Miesner, J. Stenger and W. Ketterle - Phys. Rev. Lett. 80, 2027 (1998)

[24] T.-L. Ho - Phys. Rev. Lett. 81, 040742 (1998)

[25] J. Stenger, S. Inouye, D. M. Stamper-Kurn, H.-J. Miesner, A. P. Chikkatur and W. Ketterle - Nature 396, 345 (1998)

[26] H.-J. Miesner, D. M. Stamper-Kurn, J. Stenger, S. Inouye, A. P. Chikkatur and W. Ketterle - Phys. Rev. Lett. 82, 112228 (1999)

[27] D. M. Stamper-Kurn, H.-J. Miesner, A. P. Chikkatur, S. Inouye, J. Stenger and W. Ketterle - Phys. Rev. Lett. 82, 040661 (1999)

[28] M.-S. Chang, C. D. Hamley, M. D. Barrett, J. A. Sauer, K.M. Fortier,W. Zhang, L. You and M. S. Chapman - Phys. Rev. Lett. 92, 140403 (2004)

[29] T. Kuwamoto, K. Araki, T. Eno and T. Hirano - Phys. Rev. A 69, 063604 (2004)

[30] L. E. Sadler, J. M. Higbie, S. R. Leslie, M. Vengalattore and D. M. Stamper-Kurn Nature 443, 312 (2006)

[31] J. Kronjäger, C. Becker, P. Navez, K. Bongs and K. Sengstock - Phys. Rev. Lett. 97, 110404 (2006)

[32] S. R. Leslie, J. Guzman, M. Vengalattore, Jay D. Sau, Marvin L. Cohen and D. M. Stamper-Kurn - Phys. Rev. A 79, 043631

[33] C. Klempt, O. Topic, G. Gebreyesus, M. Scherer, T. Henninger, P. Hyllus, W. Ertmer, L. Santos and J. J. Arlt - Phys. Rev. Lett. 104, 195303 (2010)

[34] A. Widera, F. Gerbier, S. Fölling, T. Gericke, O. Mandel and I. Bloch - Phys. Rev. Lett. 95, 190405 (2005)

[35] Scherer, M., B. Lücke, G. Gebreyesus, O. Topic, F. Deuretzbacher, W. Ertmer, L. Santos, J. J. Arlt and C. Klempt - Phys. Rev. Lett. 104, 195303 (2010)

[36] C. Klempt, O. Topic, G. Gebreyesus, M. Scherer, T. Henninger, P. Hyllus, W. Ertmer, L. Santos and J. J. Arlt - Phys. Rev. Lett. 103, 195302 (2009)

[37] F. Deuretzbacher, G. Gebreyesus, O. Topic, M. Scherer, B. Lücke, W. Ertmer, J. Arlt, C. Klempt and L. Santos - Phys. Rev. A. 82, 053608 (2010)

[38] V. B. Braginsky and, Y. I. Vorontsov - Sov. Phys. Usp. 17, 644 (1975)

[39] V. B. Braginsky, Y. I. Vorontsov and F. Y. Khalili - Sov. Phys. JETP 46, 705 (1977)

[40] K. S. Thorne, R. W. P. Drever, C. M. Caves, M. Zimmermann and V. D Sandberg - Phys. Rev. Lett. 40, 667 (1978)

[41] W. G. Unruh - Phys. Rev. B 19, 2888 (1979)

[42] G. J. Milburn and D. F Walls - Phys. Rev. A 28, 2065 (1983)

[43] B. Yurke - J. Opt. Soc. Am. B 2, 732 (1985)

[44] N. Imoto, H. A. Haus and Y. Yamamoto - Phys. Rev. A 32, 2287 (1985)

[45] J. F. Roch, G. Roger, P. Grangier, J. M. Courty and S. Reynaud - Applied Phys. B 55, 291 (1992)

[46] J. P. Poizat and P. Grangier - Phys. Rev. Lett. 70, 271 (1993)

[47] S. F. Pereira, Z. Y. Ou and H. J. Kimble - Phys. Rev. Lett. 72, 214 (1994)

[48] K. Bencheikh, J. A. Levenson, P. Grangier and O. Lopez - Phys. Rev. Lett. 75, 3422 (1995)

[49] A. Kuzmich, Klaus Mølmer and E. S. Polzik - Phys. Rev. Lett. 79, 244782 (1997)

[50] W. Ketterle, D. S. Durfee and D.M. Stamper-Kurn - Proceedings of the International School of Physics "Enrico Fermi" (1999)

[51] L. D. Turner, K. F. E. M. Domen and R. E. Scholten - Phys. Rev. A 72 031403 (2005)

[52] K. Hammerer, A. S. Sørensen and E. S. Polzik - Rev. Mod. Phys 82, 021041 (2010)

[53] A. Kuzmich, N. P. Bigelow and L. Mandel - Europhys. Lett. 42(5), 481 (1998)

[54] F. Kaminski, N.S. Kampel, M.P.H. Steenstrup, A. Griesmaier, E.S. Polzik and J.H. Müller - Eur. Phys. J. D 66, 227 (2012)

[55] C. C. Gerry and P. L. Knight - Introductory Quantum Optics, Cambridge, 2005

[56] V. I. Balykin, V. G. Minogin and V. S. Letokhov - Rep. Prog. Phys. 63, 1429 (2000)

[57] L. Duan, J. I. Cirac, P. Zoller and E. S. Polzik - Phys. Rev. Lett. 85, 265643 (2000)

[58] Grimm R., Weidemüller M. and Ovchinnikov Y. B. - Advances In Atomic, Molecular and Optical Physics Vol. 42 pp. 95, 2000

[59] P. W. Milloni and J. H. Eberly - Laser Physics, Wiley, 2010

[60] J. M. Geremia, J. K. Stockton and H. Mabuchi - Phys. Rev. A 73, 042112 (2006)

[61] M. Kubasik, M. Koschorreck, M. Napolitano, S. R. de Echaniz, H. Crepaz, J. Eschner, E. S. Polzik and M. W. Mitchell - Phys. Rev. A 79, 043815 (2009)

[62] S. R. de Echaniz, M. W. Mitchell, M. Kubasik, M. Koschorreck, H. Crepaz, J. Eschner and E. S. Polzik - J. Opt. B: Quantum Semiclass. Opt. 7 (2005) S548-

[63] J. F. Sherson - Quantum Memory and Teleportation Using Macroscopic Gas Samples, Ph.d. Thesis, University of Aarhus 2006

[64] M. Kubasik - Towards Spin Squeezing in Cold Atomic Ensembles, Ph.d. Thesis, Departament de Física Aplicada 2009

[65] To be published

[66] M. Lewenstein, A. Sanpera, V. Ahufinger - Ultracold Atoms in Optical Lattices: Simulating quantum many-body systems, Oxford University Press, 2012

[67] F. Mandl - Statistical Physics, Wiley, second edition, 1988

[68] A. J. Leggett - Rev. Mod. Phys. 73, 020307 (2001)

[69] T Ohmi and K Machida - Jour. Phys. Soc. Jap. 67, 061822 (1998)

[70] C. V. Ciobanu, S.-K. Yip and T.-L. Ho - Phys. Rev. A 61, 033607 (2000)

[71] M. Ueda - Phys. Rev. A 63, 013601 (2001)

[72] F. Dalfovo, S. Giorgini, L. P. Pitaevskii and S. Stringari - Reviews of Modern Physics, Vol. 71, No. 3 (1999)

[73] A. Widera, F. Gerbier, S. Fölling, T. Gericke, O. Mandel and I. Bloch - New J. Phys. 8 152 (2006)

[74] D. J. Griffiths - Introduction to Quantum Mechanics (International Edition), second edition, Prentice Hall, 2005

[75] M. Scherer - Nichtklassische Zustände in Spinor-Bose-Einstein-Kondensaten, Ph.d. Thesis, University of Hanover 2011

[76] H. J. Lewandowski, D. M. Harber, D. L. Whitaker and E. A. Cornell - J. Low Temp. Phys. 132, 309 (2003)

[77] H. K. Andersen - Bose-Einstein condensates in optical lattices, Ph.d. Thesis, University of Aarhus 2008

[78] D. M. Brink and C. V. Sukumar - Phys. Rev. A 74, 035401 (2006)

[79] T. Esslinger, I. Bloch and T. W. Hänsch - Phys. Rev. A 58, 042664 (1997)

[80] G. Reinaudi, T. Lahaye, Z. Wang, and D. Guéry-Odelin - Opt. Lett. 32, 3143 (2007)

[81] J. H. Denschlag, J. E. Simsarian, H. Häffner, C. McKenzie, A. Browaeys, D. Cho, K. Helmerson, S. L. Rolston and W. D. Phillips - Journal of Physics B: Atomic, Molecular and Optical Physics, 35(14):3095 (2002)

[82] B. H. Bransden and C. J. Joachain - Physics of Atoms and Molecules, second edition, Prentice Hall, 2003

[83] Steck D. A. - "‘Rubidium 87 D Line Data,"’ (revision 2.0.1, 2 May 2008):

`http://steck.us/alkalidata`

[84] J. D. Jackson - Classical Electrodynamics, 3rd edition, Wiley, 1999

[85] Gerlach, W., and O. Stern - Ann. Phys.-Berlin 74, 673 (1924)

[86] J. M. McGuirk, D. M. Harber, H. J. Lewandowski and E. A. Cornell - Phys. Rev. Lett. 91, 150402 (2003)

[87] Jacob F Sherson, Sung Jong Park, Poul L Pedersen, Nils Winter, Miroslav Gajdacz, Sune Mai and Jan Arlt - New J. Phys. 14 083013 (2012)

[88] C. Weitenberg - Single-Atom Resolved Imaging and Manipulation in an Atomic Mott Insulator, Ph.d. Thesis, University of Munich, 2011

[89] J.-F. Schaff, X.-L. Song, P. Capuzzi, P. Vignolo and G. Labeyrie - EPL 93, 23001 (2011)

[90] J. F. Bertelsen - Ultracold Atomic Gases *Mixtures and Molecules*, Ph.D. Thesis, University of Aarhus 2007

[91] C. J. Hawthorn, K. P. Weber and R. E. Scholten - Rev. Sci. Instrum. 72, 4477 (2001)

[92] U. Schünemann, H. Engler, R. Grimm, M. Weidemüller and M. Zielonkowski - Rev. Sci. Instrum. 70, 242 (1999)

[93] N. Sharma - Off-Resonant Laser System for Non-Destructive Faraday Probing of Ultra-Cold Atoms, masters thesis, Cochin University of Science and Technology 2011

A. Laser Systems

There are three different laser system in the experiment, these are: the rubidium laser system, lattice lasers and the Faraday laser. Below are descriptions of the rubibium and Faraday laser setups, their locking schemes and the use of the light. The lattice laser is adequately described in chapter 3.1.

A.1 Rubidium Laser System

A detailed description of the rubidium system can be found in the Ph.D. thesis of Jesper Fevre Bertelsen [90] and Henrik Kjær Andersen [77]. The description given here follows these thesis. The rubidium system consists of the master, the cooler and the repump lasers. The master and repump lasers are locked by Doppler free saturated absorption spectroscopy to the $F = 2 \rightarrow F' = 1/3$ transition and $F = 1 \rightarrow F' = 2$ transitions of the D2 line respectively. The cooler laser is offset locked from the master laser 22 MHz below the $F = 2 \rightarrow F' = 2$ transition. All lasers used in the experiment are home built and are Littrow configuration extended cavity diode laser [91]. They are very stable and except for the repump laser will usually stay locked all day.

The laser is illustrated in figure A.1(a). The diode is mounted onto a good thermal conductor from which heat is removed or added by a peltier element. The peltier crystal uses the aluminum base of the laser as a reservoir for temperature stabalisation. The light emitted by the diode hit a diffraction grating which reflect the first order diffracted light back into the diode setting the frequency. By changing the angle of the grating the frequency is changed allowing us to fine tune the frequency. A piezo crystal is used to fine tune the frequency to keep the laser locked [91].

As mentioned the lasers are locked to rubidium 87 using saturated absorption spectroscopy. A high intensity laser beam, well above the saturation intensity, is passed through a glass cell with rubidium at room temperature. The atoms are moving leading to Doppler broadening of the absorption peak. The Doppler broadening at room temperature smear out the hyperfine structure of the excited state. To resolve the hyperfine structure and lock the laser to a specific transition a second "‘probe"’ beam is sent through the cell traveling in the opposite direction. If an atom is resonant with both pump and probe beam the atoms will already be in the excited states. This will show itself as a higher signal on the probe beam which is illustrated in figure A.1(b). Both the pump and probe beams are resonant with stationary atoms, which resolve the hyperfine manifold. The lasers also become resonant if the Doppler shift is equal to half the hyperfine splitting. This gives rise to 1/3, 1/2 and 2/3

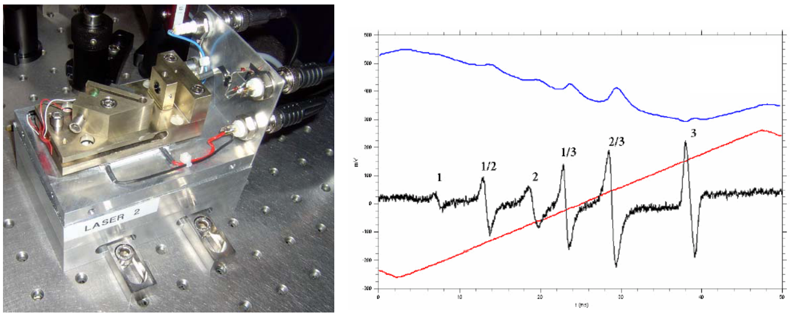

(a) (b)

Figure A.1: (a) The home-built laser system with the diode on the right and the grating on the left. The peltier crystal is mounted on the left end of the pivot. (b) Saturated absorption (top) and locking signal (bottom) for the D2 transition in rubidium 87. The numbers denote the hyperfine manifold which is resonant there. Both figures taken from [90].

lines in figure A.1(b).

By modulating the current on the laser diode at 10 MHz we are able to produce a dispersion signal to be used for locking. The laser is locked and the piezo crystal makes sure the proper frequency is selected. The dispersion curve is also shown in figure A.1(b) and the servo which drive the piezo is locked to zero-crossings in this dispersion.

The rubidium laser system is used to produce light for the magneto optical trap and for absorption imaging. The locking points of the lasers are illustrated in figure A.2 and the layout of the whole system can be seen in figure A.3. The MOT uses three types of off-resonant light: cooling, repumping and optical pumping light. The atoms are trapped and cooled by the combination of the magnetic field gradients and the cooling light. The cooling light is red-detuned from the $F = 2$ to $F' = 2$ transition. Due to the Doppler shift atoms moving opposite the propagation direction of a red detuned laser will experience the light closer to resonance than atoms moving in the direction of the laser light. Two counter propagating beams create a trapping potential. The atom will feel a force from the laser it is moving towards that is greater than the one it is moving away from, creating a cooling effect because the atoms are continually slowed. Unless the laser beams are very well matched this focus may not be very tight. To increase the tightness of the confinement a magnetic quadrupole field is added to the mix and $\sigma^{\pm}$ light is used to cool the atoms. Because of this different m_F states in the excited hyperfine manifold are addressed by the two beams so on one side of the magnetic field minimum the atom see the one laser as the strongest while on the other the other laser. This means the atoms are trapped in the magnetic field minimum. The MOT light is provided by the cooler laser. In each branch of MOT light 14-16 mW of power is needed.

When cooling the atoms we address a cyclic transition in the level scheme of rubidium.

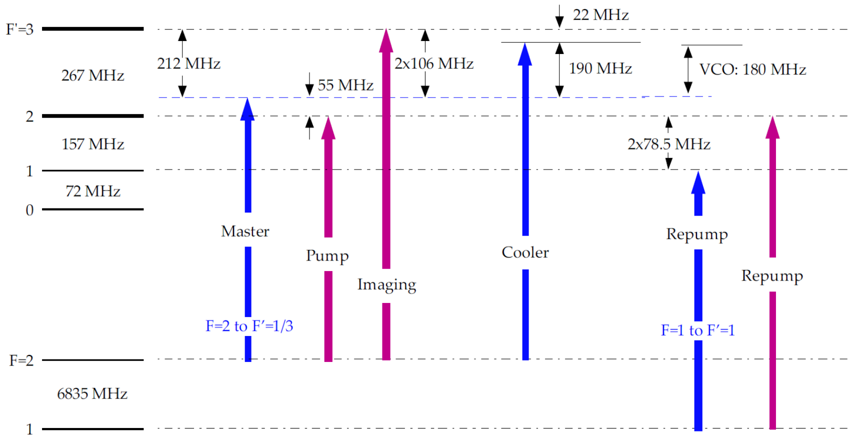

Figure A.2: An illustration of the locking scheme of the rubidium laser system. The blue lines are the locking points of the lasers and the red lines are the frequencies of the light after modulators. The figure is taken from [77]

Even though we are driving a cyclic transition in rubidium atoms can decay into the $F = 1$ manifold. In this case they have to be transferred back into the cyclic transition. This is done with the repump laser, resonant with the $F = 1$ to $F' = 2$ transition. By driving this transition along with the cooling light the capture of atoms is much more efficient because the main source of loss have been eliminated from the trap.

The final stage of the trapping is the optical pumping of the atoms into the $|2,2\rangle$ state. This ensures a large portion of the trapped and cooled atoms also stay in the trap when the MOT light is turned off. Only the $|2,1\rangle$ and $|2,2\rangle$ states are trappable which is why σ^+ light is used to drive transitions with $\Delta m_F = +1$. The pump light is produced by the master laser and is shifted on resonances with the $F = 2$ to $F' = 2$ transition by the AOM.

The imaging light is resonant with the $F = 2$ to $F' = 3$ transition. This resonances is fine-tuned by an AOM which allow us to change the frequency of the imaging light when changing magnetic fields.

The master and repump lasers are both locked to transitions in rubidium while the cooler laser is offset locked from the master laser. A small amount of light is split off from the master laser and is mixed with light from the cooler laser. This mixed signal is sent onto the a photo-detector with a bandwidth of 300 MHz. The photo detector can only resolve the beat signal which is used for locking the cooler laser.

The cooler laser is amplified by a tapered amplifier to deliver power enough to build the MOT. It is then split into three branches of even power each feeding into a fiber. The fibers go to the experiment table and is used for the MOT. Each fiber is split in two and provide equal power for the counter-propagating beams of the MOT.

The master laser is first split in two, the optical pumping and imaging branches. They

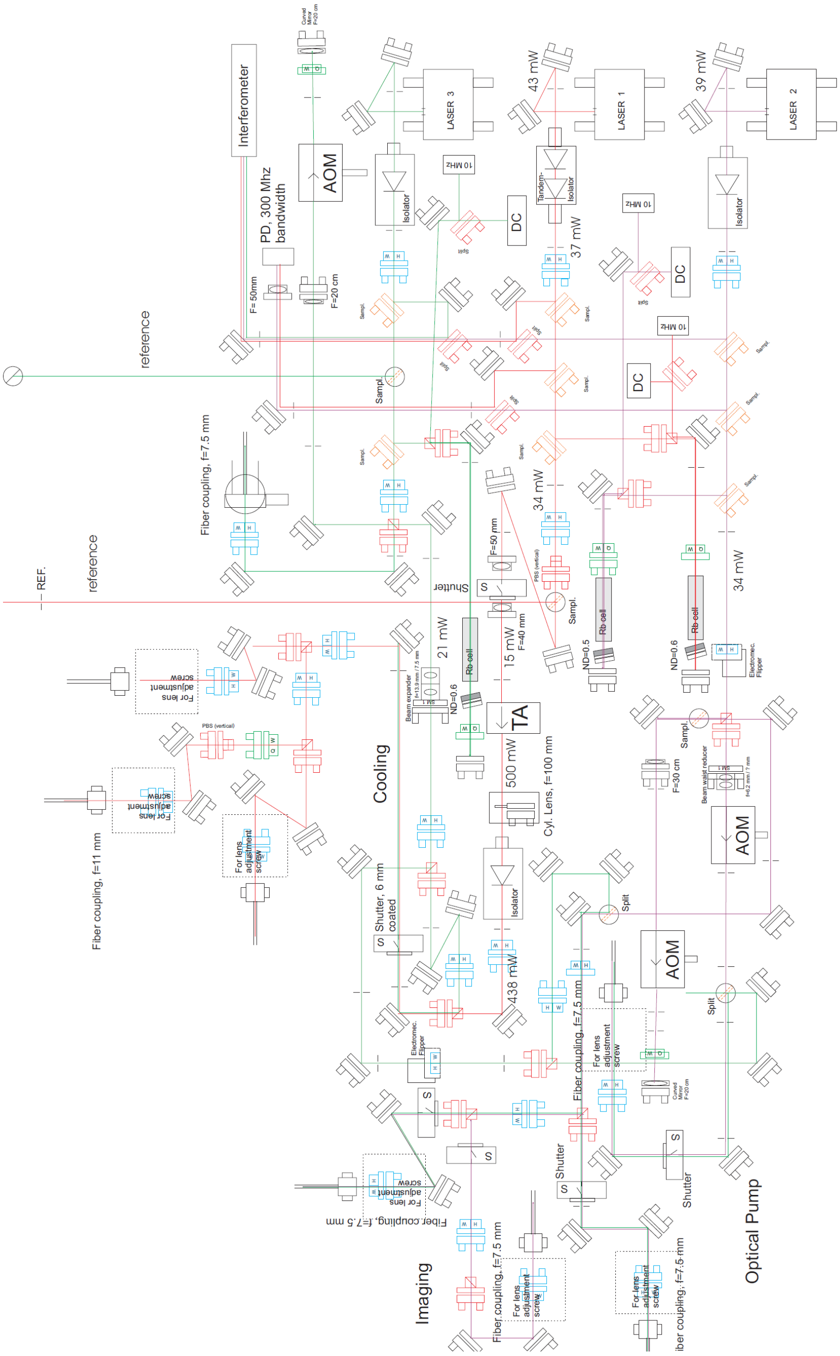

Figure A.3: An illustration of the locking scheme of the rubidium laser system. The master laser is locked at the The figure is taken from [90] each have an individual AOM which allow fine tuning of the frequencies individually. The imaging light is split in three to provide imaging light for all three axis.

The repumper light is split in two where one part is mixed with the cooling light on a beam splitter and is sent into one axis of the MOT. There are not very stringent requirements on the MOT repump light as long as a around 1 mW of power gets to the experimental table. The other branch of repump light is combined with the imaging light and sent into the imaging system when we are interested in imaging the $F = 1$.

A.2 Faraday Imaging Laser

The Faraday laser is of the same design as the rubidium lasers. The locking scheme is different because we use a tunable offset lock unlike the cooler laser which is locked to a fixed frequency. The locking scheme is based on the scheme developed by Schünemann *et. al.* [92]. As mentioned the original Faraday system was built by Nityanand Sharma and a detailed description of the system and analysis can be found in his masters thesis [93]. An illustration of the offset locking circuit can be seen in figure A.4.

In the Faraday system the beat frequency of the master and Faraday lasers are converted into an electronic signal by a fast photo diode. The manipulation of this electronic signal is what allow us to tune the laser frequency over a 900 MHz range. The beat signal has frequency $\omega_B = \omega_L - \omega_{Far}$, the difference between the master and Faraday laser. The beat signal is mixed with the output of a voltage controlled oscillator at frequency ω_O. High frequency components are removed and the signal is amplified before it is split in two. The signals will now propagate through cables of different lengths before they are recombined. High frequency components are again removed with a low pass filter. The signal is used to lock the Faraday laser to master laser by driving a servo amplifier.

The signals of the system start with the signal of the photo detector $E_B(t)$ and the signal of the voltage controlled oscillator $E_O(t)$

$$\begin{aligned} E_B(t) &= E_{0,B}\cos(\omega_B t + \phi_B) \\ E_O(t) &= E_{0,O}\cos(\omega_O t + \phi_O) \end{aligned} \tag{A.1}$$

where $E_{0,i}$ and ϕ_i $(i = \{B, O\})$ are the amplitude and phase of the signals from the photo detector and oscillator respectively. These are mixed producing a product signal. High frequency components are removed with a low pass filter leaving

$$E_{mix}(t) = \frac{E_{0,B}E_{0,O}}{2}\cos\left((\omega_B - \omega_O)t + (\phi_B - \phi_O)\right). \tag{A.2}$$

This signal is split in two and allowed to propagate in cables of different length. After the propagation they are recombined with another mixer. The two branches have evolved for different times τ_1 and τ_2. Combining the signals the difference in time can be experessed as

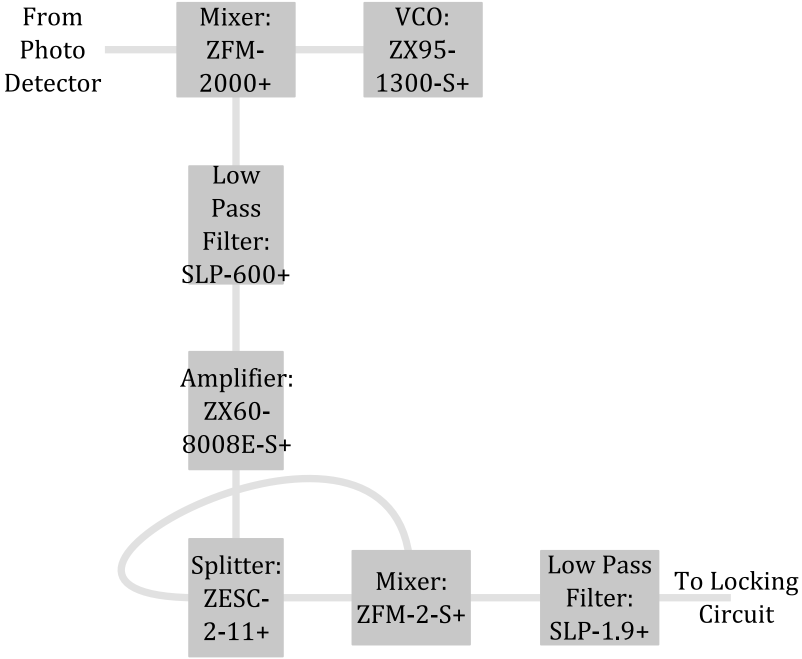

Figure A.4: The tunable offset lock used for the Faraday laser. The circuit is built of mini-circuit microwave parts.

a relative pahse. The relative phase is the frequency times the difference in evolution time

$$\Phi = (\omega_B - \omega_O)(\tau_2 - \tau_1)\,. \tag{A.3}$$

The mixed signal after recombination is

$$E_{delay}(t) = \frac{E_{0,B}^2 E_{0,O}^2}{8}\left(\cos(\Phi) + \cos(2(\omega_B - \omega_O)t + 2(\phi_B - \phi_O) + \Phi)\right). \tag{A.4}$$

The second term is removed with a low pass filter leaving only a dependence on the relative phase. For the frequency range under investigation the signal propagates at the same speed in the cables so the relative propagation time will always be the same leaving only a dependence on the relative frequency.

The delay signal is used to drive the servo-amplifier which lock the frequency of the Faraday laser with respect to the master laser. The Servo-amplifier uses the signal from the locking circuit where it is locked to a zero-crossing.

B. Lattice Loading

This section is included to illustrate the different methods tried for loading the lattice. To argue why we ended with our current loading method. When it was realised that loading from the decompressed trap did not result in a condensate in the lattice, two approaches were taken towards the creation of a condensate. The first was by evaporating in the lattice because it was hoped that it could produce condensates that did not oscillate. Oscillations are to be expected from the loading procedure as discussed. Evaporating in the lattice was thought to reduce these oscillations because of the three second evaporation after loading the lattice. The second method, which proved the most successful, was to load the condensate directly from the tight magnetic trap.

B.1 Lattice Evaporation

The Munich group used a magnetic gradient along the axis of the optical lattice to create a condensate of a few thousand atoms in their experiment. In our experiment we also used a magnetic gradient, in the transverse direction, to create the condensate. With this method we were able to create condensates of $1.4 \cdot 10^4$ atoms with a purity of 34%.

First the cloud loading was optimised, here a large cloud was decided to be more important than a very cold cloud. If we created a very cold cloud and loaded it into the lattice it would be heated by the act of loading. When loading a hotter and larger cloud it would be easier to overcome the heating caused by the transfer. The temperature increase should be proportionally smaller for the hot than the cold cloud. The largest clouds the lattice could hold were 10^6 atoms at a temperature around 1 μK. It did not matter if the depth of the lattice was 16 or 32 E_{rec} indicating that a larger cloud is bigger than the waist of the lattice.

First evaporation was attempted without a magnetic gradient which did not yield any condensate fraction results. The lattice depth was lowered from 32 to 8 E_{rec} in 3 seconds using multiple linear ramps. To increase the evaporation efficiency a magnetic gradient was introduced. In an optical lattice you relax the trap while lowering the lattice depth, i.e. the cloud has to be colder or larger to condense than the shallower the lattice. By applying a gradient we are able to lower the side of the lattice without relaxing the trap giving a higher condensation temperature. This is caused by the Zeeman energy changing the potential seen by the atoms. In our case it could be described as lowering one side of the trap.

The gradient was produced by the Ioffe coil. This was less than ideal, we only evaporated on one side of the cloud. Ideally the magnetic gradient would be along the axis of the lattice, allowing evaporation along both weak directions of the lattice. As a first attempt at

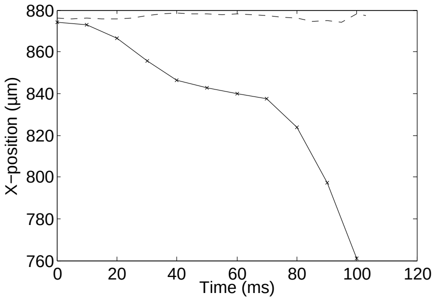

Figure B.1: Position of the condensate along the weak direction of the trap as the QUIC trap is turned off without (solid) and with (dashed) the quadrupole compensation ramp.

introducing lattice evaporation the Ioffe coil was a straight forward implementation compared to constructing a gradient coil along the lattice axis. It was tried to use both a constant gradient while lowering the lattice depth and also raising the gradient while having a constant lattice depth. Both methods worked equally well creating the condensates as discussed above.

At the end of evaporation the gradient had to be turned off to allow for spinor dynamics. This set the cloud oscillating eliminating what was thought to be the biggest advantage of this method. It was assumed that this oscillation would not disappear by using a gradient coil along the axis of the lattice. The waist of the lattice is 101 μm, The lattice and gradient coil would have to be aligned to higher precision than this to avoid oscillations. Because of the oscillations and large variations in the condensate atom number further work on lattice evaporation was dropped in favour of optimising the loading of a condensate into the lattice.

B.2 Loading Condensates into the Lattice

Loading a condensate directly from the tight trap was investigated because it was not possible to create a condensate of satisfying quality in the lattice. The idea was to slowly turn the lattice on around the magnetic trap and then slowly turn off the magnetic trap. Turning off the magnetic trap caused the cloud to displace along the weak axis of the QUIC trap. Figure B.1(a) (solid line) illustrate the position of the cloud along the weak axis during turnoff, with no lattice. This movement indicate non-ideal behavior of the QUIC trap, either uneven current sharing or misaligned coils. To overcome this misalignment current is purposefully directed around the quadrupole coils by lowering the resistance in a parallel branch, T3 transistor in figure 4.1(b). By empirically optimising the bypass current the dashed line in figure B.1(a) can be produced. Similar behavior was not observed along the tight axis, here the balancing of the Ioffe and quadrupole coils are not as important because of the higher trapping frequency.

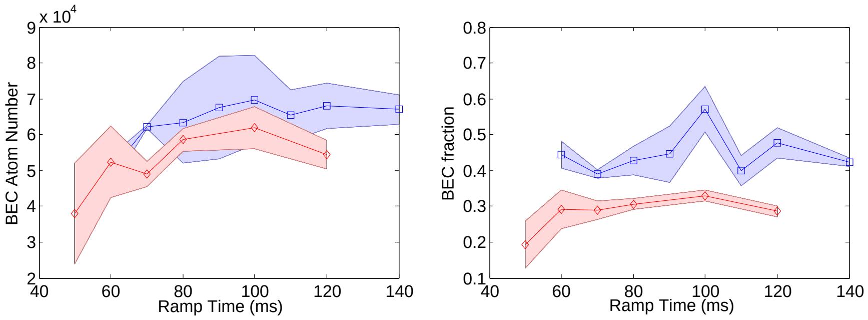

(a)

(b)

Figure B.2: (a) The size of condensates loaded from the tight (diamonds) and weak (squares) traps versus ramp time. (b) The purity of the condensate versus ramp time for the tight and weak trap. The uncertainties are standard deviations of 5 measurements.

After the introduction of the bypass ramp the cloud was stationary in the QUIC trap, except for gravitational sag, when the lattice was off. When the lattice is turned on strong oscillations are induced at the end of the loading. The oscillation is believed to be started by residual current in the Ioffe coil, observed with the H2 current transducer in figure 4.1(b). It was believed that the digital switch did not completely close the Ioffe branch. To avoid this spike it is enough to delay the digital switch by 5 ms, at which point the residual current is so small that it no longer show a noticeable effect. This loading method performed well and was used for the first spinor measurements.

During our initial investigation of spinor dynamics we observed a short lifetime of the condensate in the optical lattice. This prompted us to decompress the condensate before loading into the lattice. Instead of going back to a decompression followed by lattice loading we attempted to create a condensate in a weaker trap and also attempted to decompress and load the lattice simultaneous. Both methods seemed preferable compared to the original decompression scheme because of the oscillations this started. First it was attempted to load the lattice by simultaneously turning down the current of the QUIC and turning on the lattice. This is effectively a decompression, for the first part of the loading the magnetic trap is dominant which is relaxed, when the lattice becomes dominant the atoms are more decompressed than in the previous scheme. This showed an immediate improvement by just moving the turn on of the lattice back and ramping it in 70 ms instead of 100 ms. This resulted in $7.3(4)\cdot 10^4$ atoms at a purity around 50% compared to the previous method producing condensates of $4.3(7)\cdot 10^4$ atoms with a purity around 25%.

A parallel approach was adopted looking both at loading from the thight and a relaxed trap simultaneously. The relaxed magnetic trap produce smaller condensates of $1.3(4)\cdot 10^5$ atoms but has a transverse trapping frequency of 222.9(2) Hz. When loading from the weak trap the shape of the trapping potential is changed less, relative to the tight trap. The hope was that it would result in a purer condensate in the lattice. Figures B.2 show the condensate size and purity versus the loading time, for both the tight (diamonds) and weak trap (squares). As can be seen both traps have an optimal loading time of 100 ms above which no improvement is seen. At the same time it can be seen that loading from the tight trap produce lower quality condensates, purity wise, but the atom number is more stable as indicated by the uncertainties. Since overall atom number stability has been deemed more important than condensate purity it was decided to work further with the tight trap. It is worth noting that these measurements were performed without the quadrupole bypass ramp and therefore the results cannot be directly compared with the numbers mentioned above.

Optimising this loading comprised of tweaking timings further and the introduction a an empirically calibrated change of the T2 transistor, amplitude, timing and duration. This step on the T2 was introduced as a replacement for the wait used as the original workaround. Applying this step allowed for the tweaking of the turnoff and thereby minimising the oscillations. This turned out to improve the lattice loading dramatically and was kept because of this. The result of the optimisation is the loading of condensates around $9(1) \cdot 10^4$ atoms with a condensate fraction of 60 %.

C. Faraday Imaging Alignment

This is a description of the method used to align the Faraday imaging system. This is meant as an illustration of approach we took. It doesn't present any interesting physics but is an argument for the Faraday imaging system being aligned. Before it was know that the camera caused the cloud to be elongated a lot of effort was put into aligning the incoming imaging beam and the image plane with the orientation of the atomic cloud.

Alignment was triggered by the observation that the cloud was diagonal in the Faraday images, see figure C.1(a). The Z-axis is the QUIC traps axis of symmetry, i.e. the cloud should be round on Faraday images. The cloud being diagonal was taken as an indication that the incoming imaging beam was not aligned. Figure C.1(b) illustrates the projection of the cloud onto the image-plane in the case of a misaligned incoming beam. When the cloud is aligned with the imaging system the cloud looks round in the images. When the two are misaligned one axis seems elongated, in our case both axis were misaligned.

First the image-plane needed to be aligned with the cloud, this was done using absorption imaging. We move the L2 lens (figure 3.5(b)) using a micrometer which moves the position of the image plane in the chamber. When focusing the imaging system pictures are taken of the cloud in the trap. By moving the image plane we focus our imaging on the position of the cloud. It can also be used to check if the imaging system, after the chamber, is aligned with the axis of the cloud. If the image plane is not perpendicular to the axis of the cloud, it moves as the L2 lens is moved. If the imaging system is not aligned the first mirror after the chamber have to be adjusted until this stops. This method is not dependent on the alignment of the incoming beam.

Next the incoming beam was aligned. This was first done using Faraday images and afterward a more precise method was discovered while focusing the imaging system as described above. The initial alignment was performed by taking a Faraday image and moving the incoming beam. This was done iteratively until the cloud was round on the Faraday images. We switched to absorption imaging to make sure the camera was still focused. In the absorption images there are diffraction fringes around the cloud and we take a minimisation of these fringes to mean the camera is focused. When we switched to absorption imaging after the initial alignment of the incoming beam we saw these diffraction fringes were not symmetric around the cloud as expected of an aligned system. The shape of the fringes depended on the alignment of the incoming light. The incoming light is diffracted by the cloud, this diffraction is not even if the incoming beam and the cloud are not aligned.

After all these fine–tunings of the system we had a round cloud in the absorption images and the diffraction fringes were minimised. Using the Faraday system this was no longer

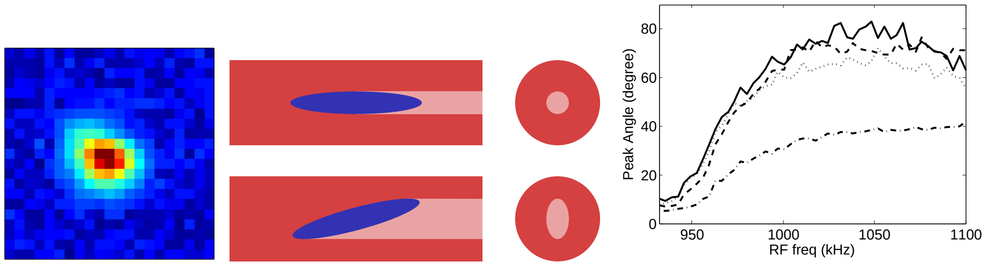

(a) (b) (c)

Figure C.1: (a) The diagonal cloud in this image illustrate how the alignment of the incoming beam have an effect. This effect of the incoming beam is also illustrated in figure (b) where the projection on the image plane is illustrated. (c) The lowering of the intensity by cutting the collimated light with an iris showing the size of the collimated beam. The iris aperture is 50 (solid), 23 (dashed), 16 (dotted) and 9 mm (dot-dashed).

the case, now the cloud was still elongated. We therefore investigated if the polarisation, focus and aspect ratio of the incoming light had an effect on the observed aspect ratio of the cloud. This was not expected to have an effect on the observed signal and it turned out that it didn't. After this we were very sure that the imaging system worked as well as possible. This initiated the investigations into the effects of the camera and the electron-multiplying register on the clouds aspect ratio as discussed above.

The final check of the imaging system was performed to make sure no signal was lost because light scattered by the atoms hit something before being collimated. If the diffraction from the cloud was so great that light hit the chamber before the L1 lens it show itself in the radius of the collimated beam. If the collimated beam is much smaller then the aperture of the optics we can conclude there is no signal lost before the light is collimated. To check this an iris was inserted before PBS2 (figure 3.5(b)), the aperture of this iris was changed to determine the width of the collimated beam. As seen from figure C.1(c) power is not lost at an iris aperture of 23 mm while at 16 mm aperature only a slight loss is seen. The aperture of all the optics on the back side of chamber is 50 mm, therefore losses due to this effect can be excluded.